Chapter 1

Introduction

Small spacecraft known as micro-, nano-, and pico-satellites are increasingly being used for low cost, rapid response, or distributed space missions [1,2]. To enable deployment of ever smaller and more versatile fleets of spacecraft, there is a logical progression toward in-space propulsion systems with high efficiency, small footprints, and low mass. Current state-of-the-art technologies are predominantly rocket propulsion systems, which generate thrust as a reaction force to the momentum of stored propellant being ejected. While propellantless propulsion technologies such as solar sails [3], magnetic sails [4], and electrodynamic tethers [5] are being developed, their operational flexibility is limited by functional dependence on ambient environmental conditions, such as solar radiation pressure, solar wind properties, and local magnetic fields.

The remainder of this chapter concerns rocket propulsion systems that convert energy, either stored in or applied to the propellant, into directed kinetic energy. For cold gas thrusters and chemical rockets, the energy source for conversion via a nozzle is the propellant's enthalpy [6]. Electric propulsion instead accelerates propellant via electrical heating, electrostatic forces on charged particles, or electromagnetic forces on plasmas [7].

1.1 Rocket Propulsion Fundamentals

Consider a rocket propulsion system that generates thrust T, defined as

$$T \equiv \dot{m} u_e, \tag{1.1}$$

where $\dot{m}$ *is* the propellant mass flow rate and u_e is the effective exhaust velocity relative to the rocket. Thrust power P_T is the rate at which directed kinetic energy is expended for thrust generation and is defined as

$$P_T \equiv \frac{1}{2}\dot{m}u_e^2 = \frac{1}{2}Tu_e = \frac{1}{2}\frac{T^2}{\dot{m}}. \tag{1.2}$$

The achievable total impulse or linear momentum change I_t during the time interval $[t, t + \Delta t]$ is defined as

$$I_t \equiv \int_t^{t+\Delta t} T\, dt. \tag{1.3}$$

Total impulse per unit sea-level weight of propellant used is the specific impulse I_{sp}, defined as

$$I_{\text{sp}} \equiv \frac{I_t}{g_0 \int_t^{t+\Delta t} \dot{m}\, dt}, \tag{1.4}$$

where g_0 is the sea-level gravitational acceleration. For the instantaneous specific impulse, Equation (1.4) simplifies to

$$I_{\text{sp}} = \frac{T}{\dot{m} g_0} = \frac{u_e}{g_0}. \tag{1.5}$$

Specific impulse is a metric indicating how efficiently a rocket uses propellant to generate thrust and can be interpreted as the amount of time that a sea-level pound-mass of propellant can generate a pound-force of thrust.

A rocket's propellant mass fraction ξ_p is defined as

$$\xi_p \equiv \frac{m_p}{m_0}, \tag{1.6}$$

where m_p and m_0 are the propellant and initial rocket wet mass, respectively. The relationship between a rocket's propellant mass fraction and specific impulse is given by the ideal rocket equation [8,9],

$$\xi_p = 1 - \exp\left(-\frac{\Delta V}{g_0 I_{sp}}\right), \tag{1.7}$$

where ΔV is the is the rocket's achieved velocity increment. For a given mission ΔV, a higher specific impulse requires less propellant mass, thus resulting in more available mass for the rocket's payload. Figure 1.1 shows this behavior for some representative nano-satellite missions [10]. The point at which the propellant mass makes up only about 10% of the rocket's wet mass, beyond which increased specific impulse provides diminished returns, occurs for $I_{sp} > \Delta V/g_0$.

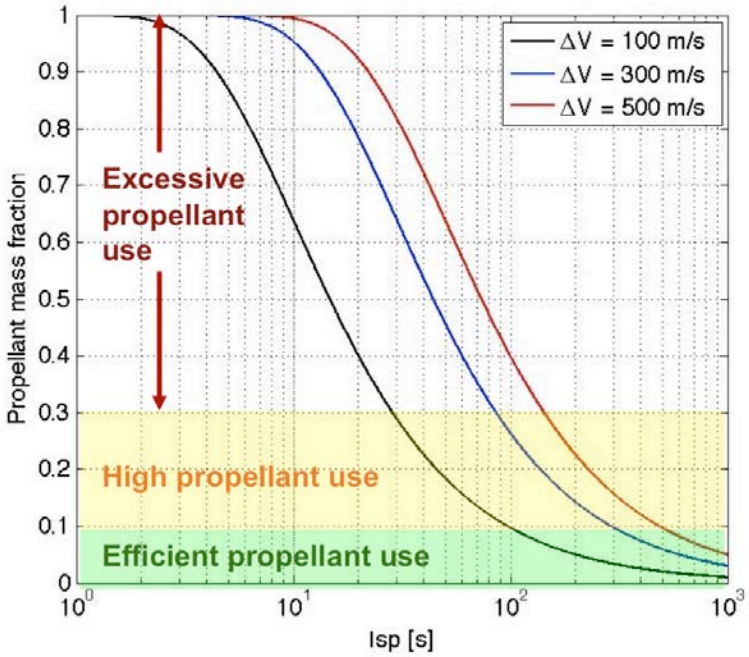

Figure 1.1: Propellant usage for representative nano-satellite missions. Specific impulses that are too low leads to excessive propellant use, whereas specific impulses that are too high provide only slight additional mass savings.

Electric propulsion systems require input power to operate and have a thrust efficiency η_T defined as

$$\eta_T \equiv \frac{P_T}{P}, \tag{1.8}$$

where P is the input power to the thruster. The propulsion system's thrust-to-power ratio T/P is given as

$$\frac{T}{P} = \frac{2\eta_T}{u_e} = \frac{2\eta_T}{g_0 I_{\text{sp}}}. \tag{1.9}$$

Under constant input power conditions, electric propulsion systems operate with $I_{\text{sp}} \propto T^{-1}$, leading to a tradeoff between better propellant use efficiency (i.e., high I_{sp} and low T) or greater thrust capability (i.e., low I_{sp} and high T).

Electrostatic propulsion systems operate by converting the electric potential energy of charged propellant undergoing a potential change V_o into directed kinetic energy. Conservation of energy (i.e., $qV_o = \frac{1}{2} mu_e^2$) and Equation (1.5) yields

$$I_{\text{sp}} = \frac{\sqrt{2V_o}}{g_0}\left(\frac{q}{m}\right)^{\frac{1}{2}}, \tag{1.10}$$

where q and m are the propellant particle's charge and mass, respectively. Meanwhile, the corresponding thrust-to-power ratio from Equation (1.9) is

$$\frac{T}{P} = \eta_T \sqrt{\frac{2}{V_o}}\left(\frac{q}{m}\right)^{-\frac{1}{2}}. \tag{1.11}$$

For a given operating voltage V_o, increasing the specific charge q/m thus increases the specific impulse while decreasing the thrust-to-power ratio.

1.2 Micropropulsion Systems

The trade space for various micropropulsion technologies is shown in Figure 1.2, including the projected performance zone for the Nanoparticle Field Extraction Thruster (NanoFET). Electrospray thrusters, when operating in colloid mode, electrostatically charge ionic liquids and accelerate the resulting charged droplets [11,12]. These thrusters can achieve fine thrust resolutions (e.g., < 0.1 μN), making them attractive for missions requiring precise pointing and positioning. While NanoFET is anticipated to have similarly fine thrust resolutions, a higher thrust capability compared to electrospray thrusters is possible due to NanoFET's more modest specific impulses; these higher thrust levels become important if higher spacecraft accelerations are desired for time-critical missions. Although cold gas thrusters (which exhaust pressurized gas) and micro-resistojets (which resistively heat the propellant) can also generate high thrusts, their specific impulses are low [13], resulting in less mass being available for payload and a lower achievable ΔV. Ion thrusters, on the other hand, have specific impulses that are too high (i.e., too low thrust-to-power) for many nano-satellite missions and also become less efficient at smaller sizes. NanoFET thus seeks to fill in the trade space and provide propulsive capabilities that would otherwise require multiple different propulsions systems, with the corresponding disadvantage of increased propulsion system mass and more complicated spacecraft integration and design [14]. Table 1.1 summarizes representative performance metrics for state-of-the-art micropropulsion systems.

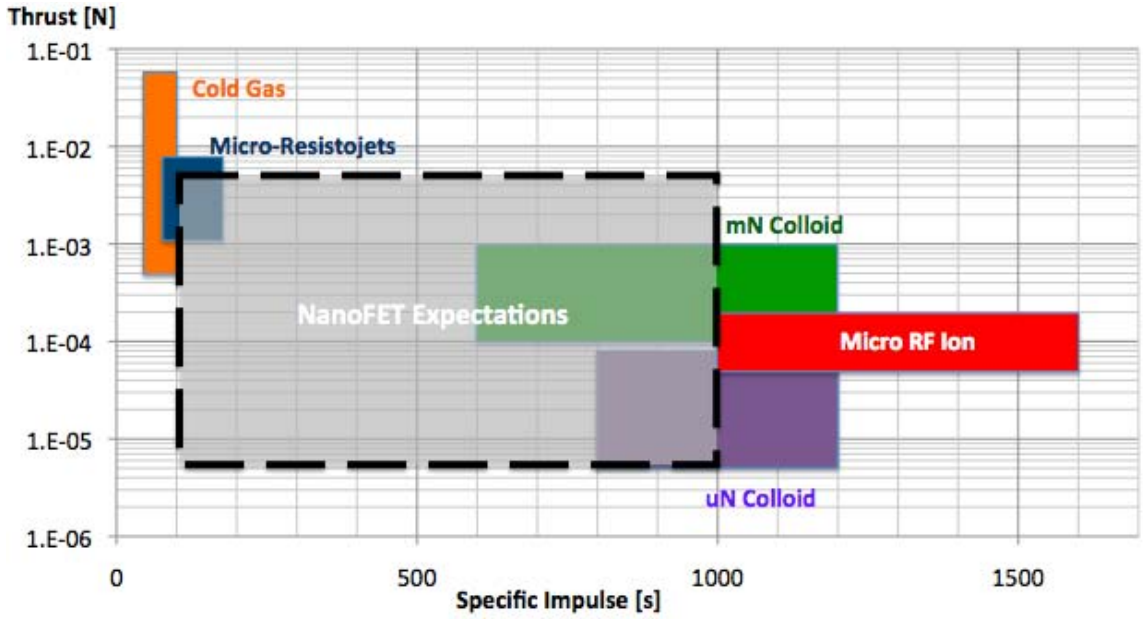

Figure 1.2: Micropropulsion trade space. NanoFET fills a region of the design space crucial for nano-satellite missions. Data from References 15 (cold gas) and 16.

Thruster Type	Specific Impulse [s]	Thrust [mN]	Thrust-to-Power [mN/W]
Cold gas	65	55	–
Resistojet	300	5	0.5
Colloid	750	0.75	0.15
Ion	1340	0.13	6.5×10^{-3}

Table 1.1: Representative micropropulsion performance. Data from References 15 (cold gas) and 16.

1.3 Nanoparticle Field Extraction Thruster: NanoFET

While similar in operation to electrospray thrusters, the Nanoparticle Field Extraction Thruster (NanoFET) does not rely on droplet formation and extraction to provide thrust. Instead, NanoFET electrostatically charges and accelerates pre-fabricated, solid micro- and nano-particles. Although the concept of electrostatically charging and accelerating micro-particles via high electric potentials is not new [17], NanoFET

proposes to charge and accelerate particles down to ~10 nm size scales using a continuous propellant feed system and a scalable, planar array configuration.

1.3.1 Configuration Overview

As shown conceptually in Figure 1.3, backpressure passively feeds the electrically conductive particle propellant in dry powder form towards the charging sieve. There, particle aggregates are dispersed upon passage through the sieve with the aid of piezoelectric-induced inertial forces. Individual particles undergo contact charging and extraction due to the electric field imposed between the charging sieve and the extractor gate. The charged particles are then accelerated to the exhaust velocity by electric fields generated between the extractor and accelerator gate electrodes. While NanoFET can operate with just a single gate electrode, having dual, stacked gate electrodes permits the charging and acceleration stages to be decoupled [18]; such a setup enables voltage throttling of NanoFET without adversely impacting particle charging. Individual emitters are arranged in a planar array sized for the desired thrust range [19].

Charge neutralization may be achieved on NanoFET using various field emission cold cathodes being considered for other micropropulsion systems [20]; these cold cathodes operate by emitting electrons from the conduction band of the emitter material via quantum mechanical tunneling under high electric fields [21]. To make use of field emission neutralizers, NanoFET must operate at positive polarity, with a maximum theoretical specific charge that is an order of magnitude greater than operation in negative polarity. An alternative approach is to have NanoFET undergo bipolar operations, where either an alternating charging electric field is applied or different segments of the NanoFET array are at different polarities; such a scheme eliminates the need for a

separate neutralizer by emitting positive and negative particles from the same propellant reservoir.

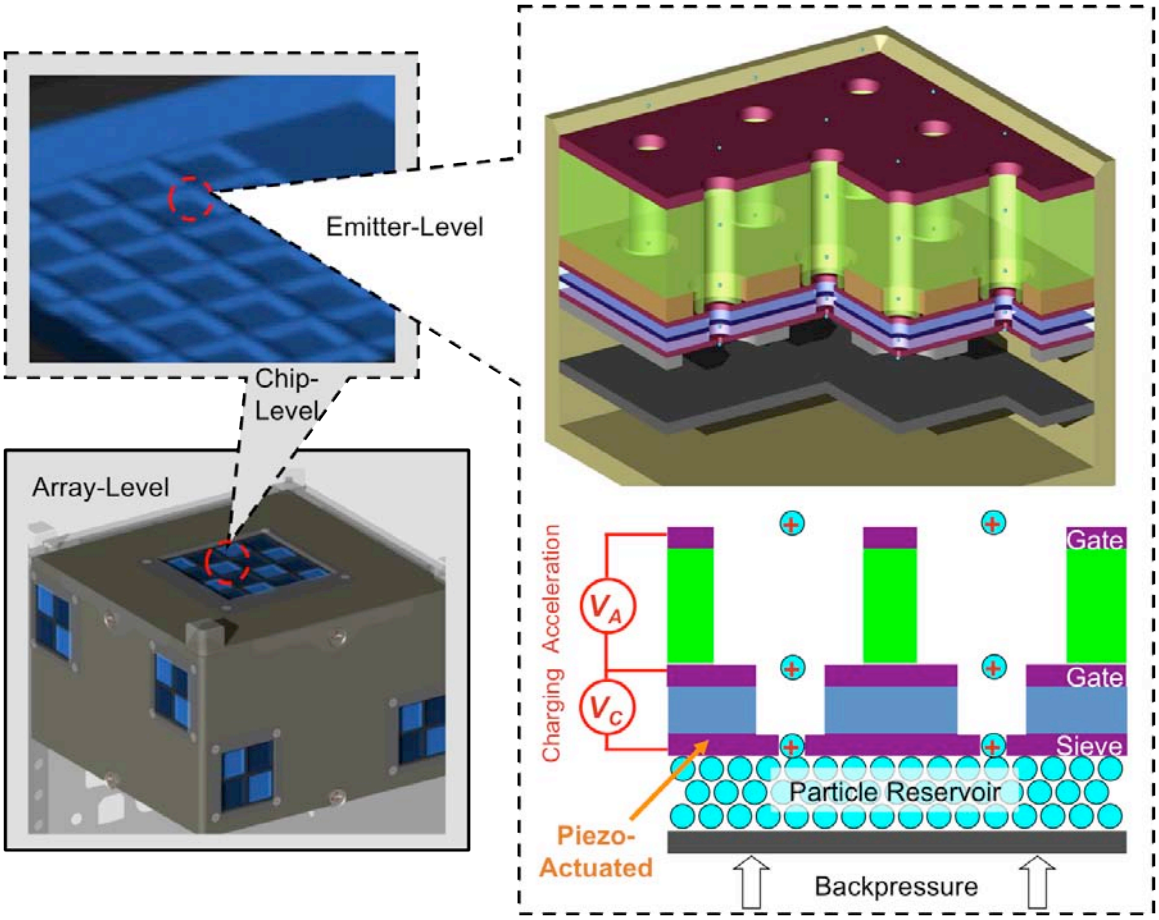

Figure 1.3: Concept views of NanoFET. Scalability is shown from the emitter (*upper right:* particles in reservoir not shown; *lower right:* cross-sectional view) up to the chip (*upper left*) and array (*lower left*) size scales. An integrated NanoFET propulsion module is shown (*lower left*) taking up half the volume of a 1-unit cubesat.

A different configuration for NanoFET also exists in which suspended particles, transported in a recirculating microfluidic feed system, are electrostatically charged and extracted from a low vapor pressure liquid reservoir via stacked electrode gates [22]. However, this liquid configuration has the disadvantage of increased parasitic mass compared to the dry particle approach due to the mass of the liquid reservoir, which does not generally contribute to propulsive thrust. Consequently, the liquid-NanoFET

configuration has a lower specific thrust (i.e., ratio of thrust to thruster mass), which makes it less attractive for space applications. Issues associated with the liquid-NanoFET configuration are examined in Chapter 6. The remainder of the dissertation concerns the use of dry powder propellant in NanoFET.

1.3.2 Benefits of Variable Specific Impulse

With the propellant electrostatically charged rather than ionized, NanoFET can tune the propellant's charge state via the charging electric field. Unlike multiple ionization processes that suffer from increasing ionization costs, NanoFET can adjust its propellant's specific charge without an apparent impact on efficiency. Equation (1.10) shows that $I_{sp} \propto (q/m)^{1/2}$ as well as the operating voltage, so NanoFET may be considered a variable-I_{sp} thruster whose widely-throttleable performance (Figure 1.4) may be optimized by adjusting the operational voltage at each point during an orbit maneuver to minimize propellant use or trip time in addition to accomplishing dynamic retasking of the host spacecraft [23].

From a system analysis point of view, a variable-I_{sp} engine is akin to having infinitely many constant-I_{sp} engines in one (i.e., a constant-I_{sp} engine's performance is a subset of the performance available to a variable-I_{sp} engine). For this reason, a variable-I_{sp} engine will always consume less propellant than a constant-I_{sp} engine. In certain cases, dual-mode constant-I_{sp} engines can approach the minimal propellant cost given by variable-I_{sp} systems [24]. The caveat to achieving the near-equivalent performance requires that the dual-mode constant-I_{sp} engine be designed specifically for the mission. This requirement is a significant problem because designing, testing, and validating an engine can take years [25]. Also, in order to optimize the engine, the mission profile

would have to be known before development began. If during development the thrust profile changes, then the engine would become non-optimal. A variable-I_{sp} engine eliminates the need for optimizing engines specifically for missions because the thrust profile can be made propellant-optimal without redesigning the engine, a particularly attractive feature for missions requiring rapid deployment of spacecraft.

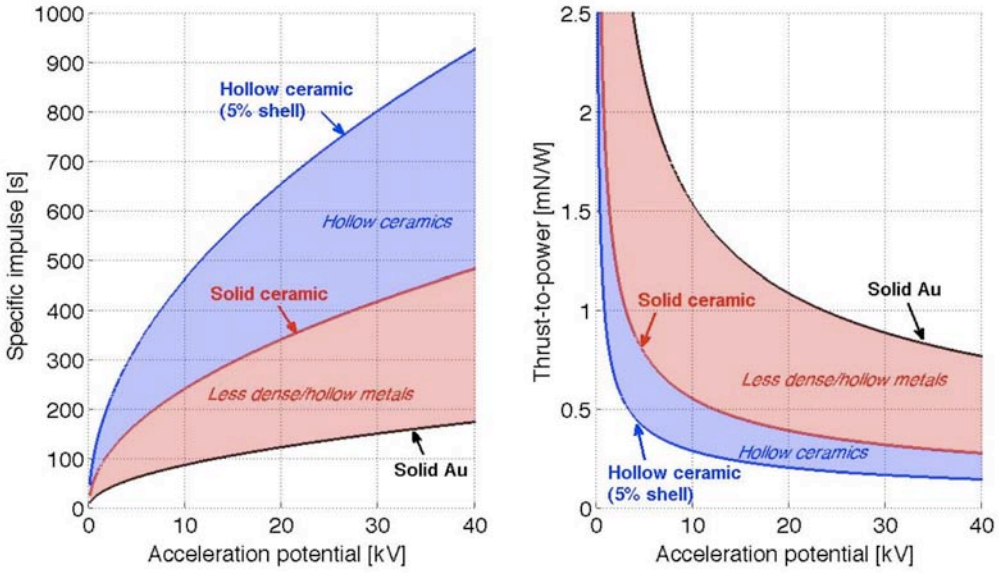

Figure 1.4: Theoretical NanoFET performance. 50-nm particles are charged in 400-V/μm electric fields. Particle properties are summarized in **Table 4.1**.

For missions that require unplanned or unknown maneuvers, such as remote sensing or observation missions, variable-I_{sp} engines are also beneficial. If a constant-I_{sp} engine is chosen for a spacecraft, then it will not be propellant optimal for the unknown future maneuvers, since they were not taken into account during the specific impulse optimization. If instead a variable-I_{sp} engine is used, then the specific impulse can be varied over time to ensure that the orbit change utilizes the minimum amount of propellant. Using a variable-I_{sp} engine thus allows a time-propellant trade to be conducted. If the propellant amount is fixed, the minimum time in which a maneuver can

be accomplished will be lower for the variable-I_{sp} engine, since it can deliver the necessary acceleration when it can be best utilized simply by adjusting the specific impulse [26].

1.4 Dissertation Overview

The remainder of the dissertation seeks to map out the design space for a NanoFET system capable of meeting the performance needs for nano-satellite missions. Chapter 2 presents numerical simulations for particles undergoing contact charging in diode configurations as well as diode design considerations for optimizing particle charging. Chapter 3 examines the effect of using piezoelectrics to help overcome electrode-particle adhesion and inter-particle cohesion. Chapter 4 presents a system-level NanoFET performance model. Chapter 5 discusses the design and testing of a micro-particle extractor prototype for NanoFET. Chapter 6 addresses the issue of liquid instability in a liquid-NanoFET configuration. Chapter 7 summarizes the research contributions of this dissertation and recommends future work.

Chapter 2

Electrostatic Charging of Particles in Diodes

For electrostatic propulsion systems such as NanoFET, increasing the propellant's specific charge is generally desirable. Equation (1.10) shows that for higher specific charges, lower operating voltages would be necessary to reach a target specific impulse. This voltage reduction could simplify power system designs and improve operational reliability.

Particles can be charged by various means, including in dusty plasmas [27], via ion or electron beams [28,29,30], or through contact charging. Trottenberg *et al.* compared these charging mechanisms and concluded that contact charging, particularly with needle electrodes at high electrostatic potential, along with electron beam charging yield the highest specific charges [31]. Electron beam charging, however, increases system complexity with the need for an electron source. NanoFET utilizes contact charging but forgoes the use of needle charging electrodes, which have the disadvantage of inconsistent charging (e.g., particles charge more at the needle's tip than on the lateral sides); propellant transport to existing needle electrode configurations is also inefficient, being a random walk of particles oscillating in response to time-varying electric fields and swirling due to Coulomb repulsion [32,33,34]. Instead, NanoFET directly back-feeds particles into a diode charging stage housing a background electric field.

2.1 Charging in a Uniform Background Electric Field

Consider an isolated, spherical particle of diameter d in contact with an infinite planar charging electrode and exposed to a uniform axial background electric field E_0 as shown in Figure 2.1. An electric field that points towards the charging electrode results in a negative particle charge; reversing the field vector changes the charge polarity.

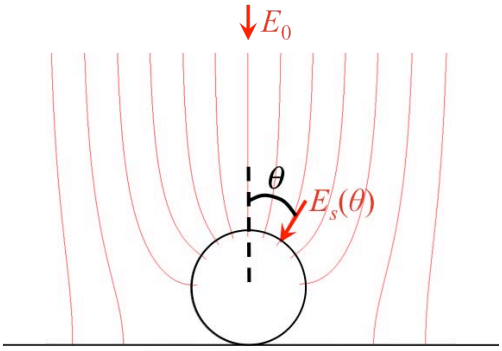

Figure 2.1: Particle charging negatively in a uniform background electric field. The charging electrode represents an infinite plane.

At the particle surface, the field enhancement factor β is defined as

$$\beta(\theta) \equiv \frac{E_s(\theta)}{E_0}, \tag{2.1}$$

where E_s is the surface electric field and θ is the polar angle. The particle charge q can be determined by applying the integral form of Gauss's law,

$$q = \varepsilon \oiint_S \mathbf{E}_s \bullet d\mathbf{A}, \tag{2.2}$$

where Gaussian surface S coincides with the particle surface, $\mathbf{E}_s$ is the surface electric field vector, and ε is the permittivity of the surrounding medium [35]. Taking advantage of azimuthal symmetry and the absence of steady-state tangential electric fields at the particle surface yields

$$q = \frac{\pi}{2} B \varepsilon E_0 d^2, \tag{2.3}$$

where the integrated field enhancement factor B is defined as [36]

$$B \equiv \int_0^{\pi} \beta(\theta) \sin\theta \, d\theta. \tag{2.4}$$

Implicit in this analysis is the assumption that the particle charges classically (i.e., quantum effects are not significant). In addition, the maximum allowable electric field E_{max} at the particle surface must be below the electron field emission (~10^3 V/μm) or ion evaporation (~10^4 V/μm) thresholds for negatively and positively charged particles [37], respectively, lest charge is lost from the particle due to quantum tunneling effects.

Félici, using the Kelvin inversion method to calculate the particle surface electric field, determined the saturation charge q_0 acquired by the particle in Figure 2.1 to be

$$q_0 \approx \frac{\pi^3}{6} \varepsilon E_0 d^2, \tag{2.5}$$

with a peak field enhancement factor of $\beta(\theta = 0) = 4.208$ [38], resulting in an integrated field enhancement factor of $B \approx \pi^2/3$. Consequently, to avoid charge loss from the particle, Equation (2.1) suggests that a background electric field no greater than $E_{max} / 4.208 \approx 0.24\, E_{max}$ may be applied.

While the particle is being charged, it will repel from the charging electrode if the electrostatic force acting on the charged particle is greater than the sum of the restraining forces. Charge will then transfer from the particle into the surrounding medium with characteristic time τ_c defined as

$$\tau_c \equiv \frac{\varepsilon}{\sigma}, \tag{2.6}$$

where σ is the electrical conductivity of the surrounding medium [39]. Redistribution of charge on the particle also occurs. In particular, a steady-state, uniform surface charge density is achieved if the particle enters a field-free region; from Equation (2.2), the corresponding constant surface electric field magnitude is

$$E_s = \frac{q}{\pi \varepsilon d^2} = \frac{B}{2} E_0 . \tag{2.7}$$

2.2 Diode Configurations

Particles in NanoFET emitters are electrostatically charged in background electric fields generated by the charging sieve and extractor gate electrodes. Because the background electric fields in such a diode (i.e., dual-electrode) configuration are not necessarily uniform due to diode geometry effects, Félici's charging model must be modified. The charging stage for a single NanoFET emitter can be represented by a gate-sieve diode. This diode configuration is shown in Figure 2.2 as the result of successive refinements of a planar diode, which does have a uniform background electric field apart from edge effects. An understanding of the nature of particle charging in these diode configurations is desirable to refine Equation (2.5) to predict NanoFET charge levels.

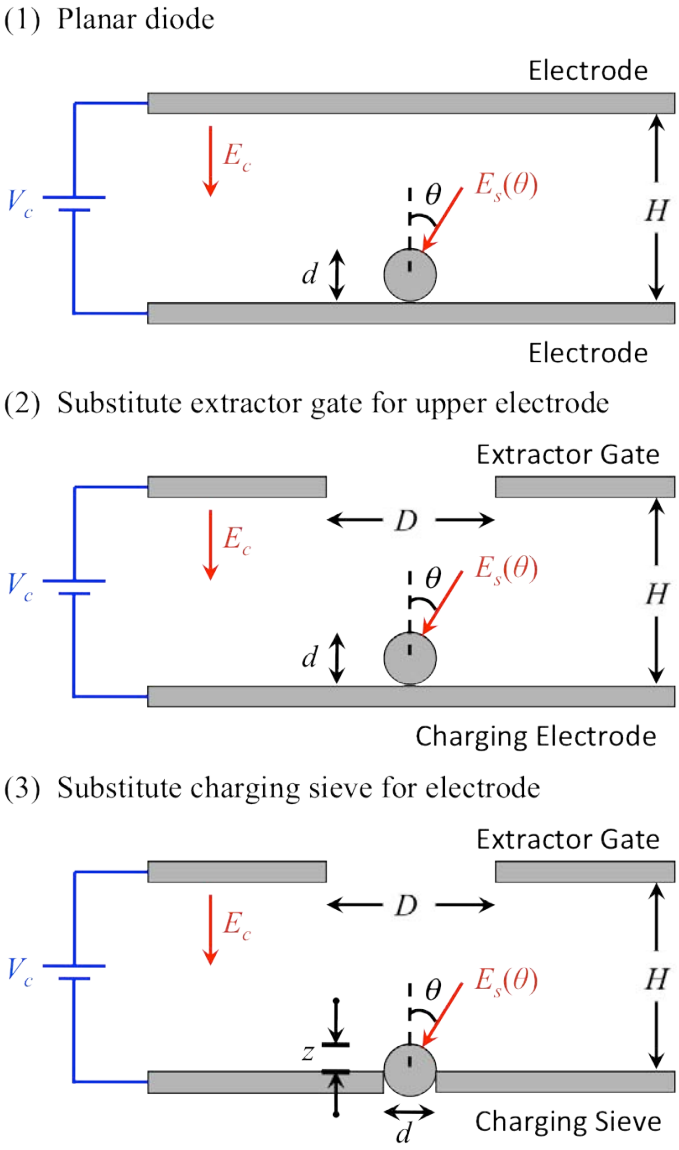

Figure 2.2: Particle charging in diode configurations. (*1*) Planar diode, (*2*) gated diode, and (*3*) gate-sieve diode represent successively better representations of an individual NanoFET emitter's charging stage.

2.2.1 Planar Diode

A uniform background electric field can be generated, apart from edge effects, in the planar diode shown in Figure 2.2(*1*) by applying a charging voltage V_c between two parallel plane electrodes with separation H. The background charging electric field E_c is defined as

$$E_c \equiv \frac{V_c}{H}, \tag{2.8}$$

and the normalized electrode separation distance $\zeta_{H,d}$ is defined as

$$\zeta_{H,d} \equiv \frac{H}{d}, \tag{2.9}$$

where $1/\zeta_{H,d}$ lies in the range (0,1); the upper bound is set to avoid having a particle that fully bridges the separation distance and shorts out the diode.

Dynamic and current measurements of particles charged in planar diodes have been previously performed [40,41]. In these studies, a particle lifts off the bottom electrode and moves towards the upper electrode if the electrostatic force acting on the charged particle is greater than the sum of the restraining forces. Upon contact with the upper electrode, the particle is charged opposite its initial polarity and is directed back towards the bottom electrode. The sequence then repeats, resulting in particle oscillations between the plates. These experiments have validated Félici's model provided that the following conditions are met:

1. The particles do not lift off until after saturation charging is achieved. This condition is facilitated by having particles and electrodes with high surface conductivities.
2. The time scale τ_c associated with particle charge transfer to the surrounding medium is large compared to the oscillation period (i.e., particle charge can be treated as constant during the transit between electrodes). This condition is facilitated by having a surrounding medium with low electrical conductivity.
3. The particles are small compared to the inter-electrode spacing (i.e., $d \ll H$). This condition is due to the field enhancement factor's dependence on $\zeta_{H,d}$, as can be

readily seen by considering the case where $\zeta_{H,d}$ approaches unity (i.e., $d \rightarrow H$). The effective diode separation distance then approaches $H - d$ at $\theta = 0$, resulting in the peak electric field and the corresponding field enhancement factor approaching $V_c / (H - d)$ and $(1 - 1/\zeta_{H,d})^{-1}$, respectively [42]. For values of $\zeta_{H,d}$ approaching unity, the maximum allowable background charging electric field E_c is necessarily reduced to avoid exceeding $E_{\max}$ at the particle surface.

2.2.2 Gated Diode

In a gated diode, the upper electrode in a planar diode is replaced with an extractor gate electrode that permits particles to leave the system. Figure 2.2(*2*) shows a gated diode with the gate orifice of diameter D centered about the particle; this setup is representative of physical NanoFET configurations in which each individual emitter has its own extractor gate. The aspect ratio $\zeta_{D,H}$ of the extractor gate is defined as

$$\zeta_{D,H} \equiv \frac{D}{H} = \frac{\zeta_{D,d}}{\zeta_{H,d}}, \tag{2.10}$$

where the normalized gate orifice diameter $\zeta_{D,d}$ is defined as

$$\zeta_{D,d} \equiv \frac{D}{d}. \tag{2.11}$$

$1/\zeta_{D,d}$ lies in the range (0,1); the upper range bound is set to permit particle extraction (i.e., $d < D$). As both $\zeta_{D,d}$ and $\zeta_{H,d}$ approach unity (i.e., $d \rightarrow D$ and $d \rightarrow H$), the particle surface approaches the gate electrode and causes the peak field enhancement factor to increase. Therefore, the maximum allowable background charging electric field E_c is necessarily reduced to avoid exceeding $E_{\max}$ at the particle surface.

2.2.3 Gate-Sieve Diode

In a gate-sieve diode, the lower electrode in a gated diode is replaced with a charging sieve. Figure 2.2(*3*) shows a gate-sieve diode with the sieve orifice being the same diameter d as the particle to permit contact charging. For a physical NanoFET charging stage, the sieve orifice is necessarily larger than the particle diameter to facilitate particle passage.

The particle tip protrudes a distance z above the sieve plane, yielding a normalized particle protrusion height $\zeta_{z,d}$ defined as

$$\zeta_{z,d} \equiv \frac{z}{d}. \tag{2.12}$$

$\zeta_{z,d}$ may be a negative value if the particle does not protrude above the sieve plane at all, and $\zeta_{z,d} > ½$ can occur in a physical gate-sieve diode due to the presence of other particles below the sieve pushing up the test particle.

2.3 Particle Charging Simulation Methodology

An understanding of the achievable particle charge in diode configurations can yield insights into scaling relations for optimizing NanoFET's charging stage. As such, electrostatic simulations using the finite element method were conducted to determine the particle surface electric field maps for each diode configuration. Equations (2.1), (2.3), and (2.4) were then used to determine the saturation charges acquired by the particles. The geometry of each diode configuration was parametrically varied to observe the particle charge's sensitivity to the various diode-scaling factors.

Simulations were conducted in COMSOL Multiphysics®, a commercial finite element analysis software package. COMSOL has been previously used in numerical

studies of particle contact charging with good agreement to analytical models [43,44]. Because the diode configurations are axisymmetric, the cylindrical coordinate (i.e., *r*-*z* space) form of Poisson's equation with electric potential ϕ and space charge density ρ_c was solved for the simulations [45]:

$$-\begin{bmatrix} \dfrac{\partial}{\partial r} \\ \dfrac{\partial}{\partial z} \end{bmatrix}^T \bullet \left(r\varepsilon \begin{bmatrix} \dfrac{\partial \phi}{\partial r} \\ \dfrac{\partial \phi}{\partial z} \end{bmatrix} \right) = r\rho_c . \tag{2.13}$$

2.3.1 Simulation Domain in COMSOL Multiphysics®

Figure 2.3 shows a conceptual view of a gated diode's simulation domain, which is 2-D axisymmetric with $r = 0$ being the centerline axis of symmetry. The gate electrode, with orifice diameter D and thickness t_G (whose effect on simulation results was shown to be minor unless the particle was in close proximity to the gate electrode), is modeled as an equipotential region at a fixed separation distance H and fixed potential difference V_c relative to the grounded ($\phi = 0$) charging electrode. Zero-charge/symmetry ($\mathbf{n} \cdot \mathbf{D} = 0$) boundary conditions are in place at the top and right boundaries of the simulation domain; they are placed far enough away from the particle to avoid artificial boundary effects, as confirmed when simulation results become independent of further increases in domain size. The medium surrounding the particle has free-space permittivity, and the rigid, grounded, spherical particle of diameter d contacts the charging electrode at the *r*-*z* space's origin. Simulation domains for the other diode configurations were similarly constructed.

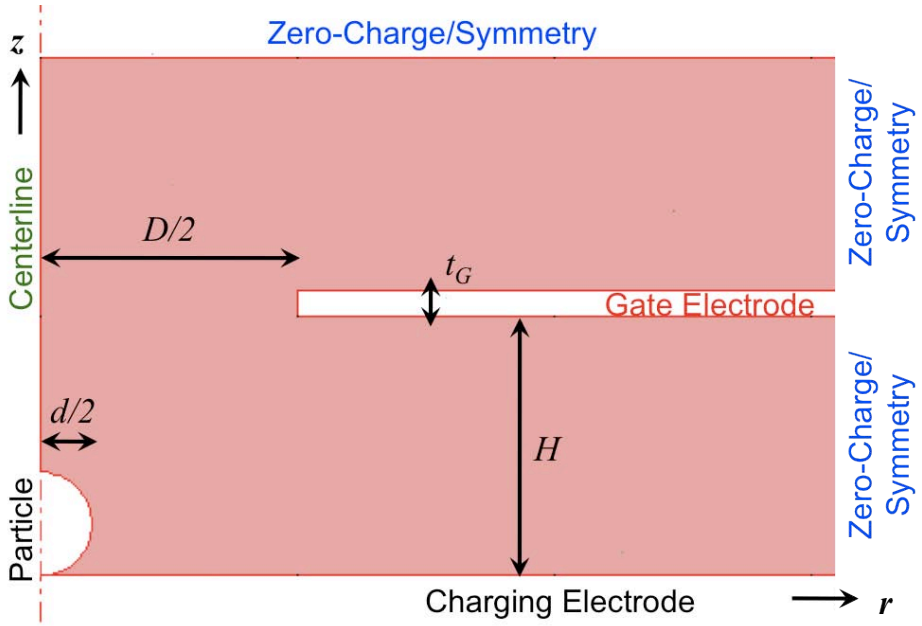

Figure 2.3: Conceptual simulation domain for gated diode. Boundary conditions shown in *r*-*z* space with a gate electrode biased relative to the grounded charging electrode.

Figure 2.4 shows the near-particle region of the simulation space for a representative gated-diode simulation in COMSOL. A free mesh of triangular elements was constructed with the finest mesh about the particle in order to acquire high-resolution particle surface electric field maps. Mesh refinement was done by dividing each element into four triangular elements, and the process continued until a mesh-independent solution was acquired. Simulation results were obtained via COMSOL's stationary, weak solution-form solver of Equation (2.13). The same approach was used for the other diode configurations.

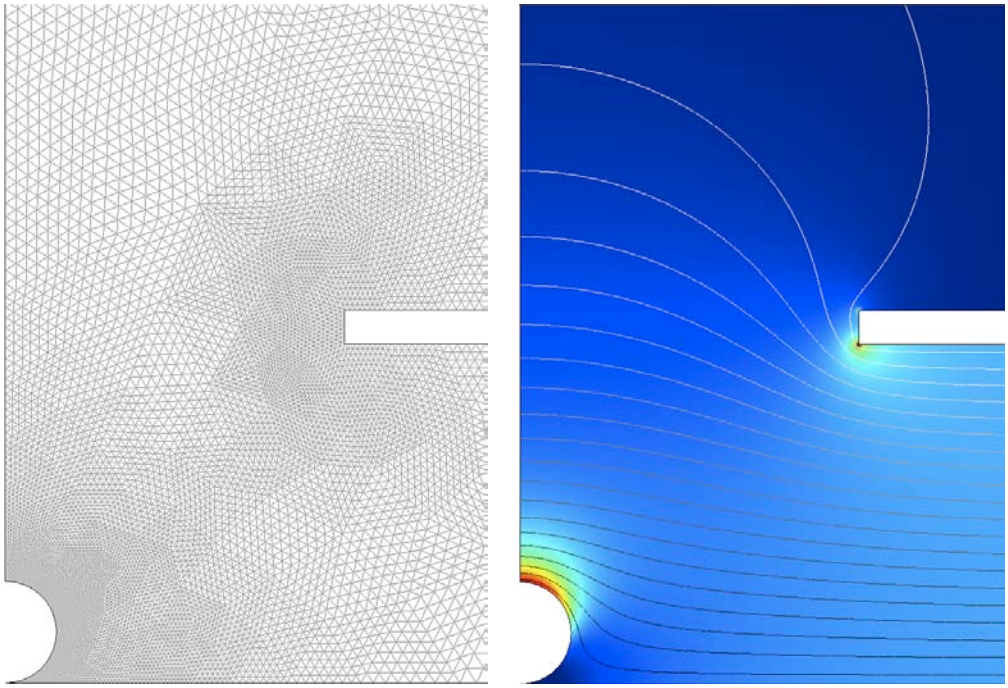

Figure 2.4: Representative isolated-particle simulation in COMSOL for gated diode. The near-particle region of the simulation domain is shown in *r-z* space. (*Left*) Unstructured mesh. (*Right*) Solved electric field magnitudes (with higher fields at the particle tip and gate corner) and equipotential lines.

2.3.2 Proximal-Particle Configurations

In any physical NanoFET charging stage with more than a single emitter, a particle at a given emitter will not be charged in isolation due to the presence of particles in adjacent emitters. The effect of proximal particles on contact charging was investigated by modifying the planar and gate diode configurations. As shown in Figure 2.5, a ring torus was used to represent the proximal particles in the simulation domain. This toroidal representation preserves the axisymmetric nature of the simulation domain and approximates the maximum packing of proximal particles of diameter d at a distance R (center-to-center) about the central particle. Figure 2.6 shows the suppression of the central particle's surface electric field due to the presence of proximal particles. A physical NanoFET charging stage would not have such close packing of the proximal particles, so the simulations provide a worst-case estimate of proximal-particle effects.

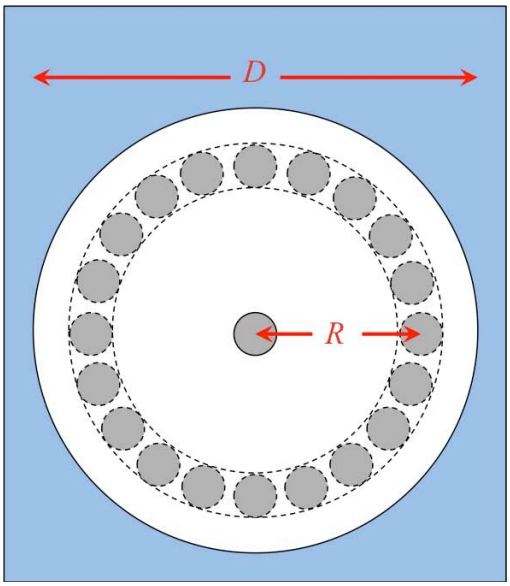

Figure 2.5: Top concept view of proximal-particle configuration for gated diode. Single gate orifice with proximal particles capable of being extracted through gate orifice.

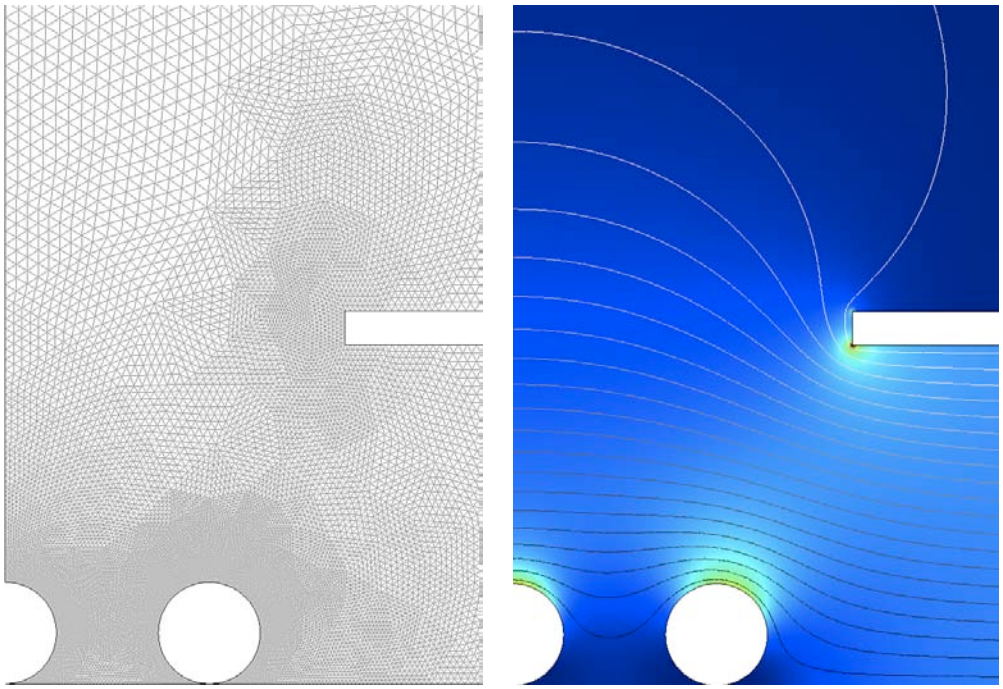

Figure 2.6: Representative proximal-particle simulation in COMSOL for gated diode. The near-particle region of the simulation domain is shown in *r*-*z* space. (*Left*) Unstructured mesh. (*Right*) Surface electric fields on central particle are reduced as compared to Figure 2.4.

The normalized proximal distance $\zeta_{R,d}$ is defined as

$$\zeta_{R,d} \equiv \frac{R}{d}. \tag{2.14}$$

$\zeta_{R,d}$ can be no smaller than unity (i.e., $R = d$), which corresponds to proximal particles in direct contact with the central particle. Proximal particles may also be extracted through the gate orifice for $\zeta_{R,d} < \zeta_{D,d} / 2 - ½$.

2.4 Simulation Results for Constant Background Charging Field

The results presented below are from simulations where charging voltage V_c and the diode separation distance H were kept constant. Therefore, the results correspond to the application of a constant background charging field E_c, which is the situation in a physical NanoFET. Care must be taken to ensure that the maximum resulting surface particle electric field does not exceed the field strength limit $E_{\max}$ for electron field emission or ion field evaporation for negatively and positively charged particles, respectively.

2.4.1 Planar Diode

Figure 2.7 shows representative isolated-particle surface electric fields in a planar diode. The peak electric field occurs at the particle tip ($\theta = 0$). For $d/H \rightarrow 0$, Félici's model is recovered, thus serving to validate the simulations. As d/H increases (i.e., increasing particle size), the surface electric field also increases, dramatically so for $d/H > 0.6$ as the effective diode separation decreases. The resulting particle charge q_1 is greater than what is expected from Félici's model (i.e., $q_1 > q_0$) by the planar-diode isolated-particle charging factor α_{10}, defined as

$$\alpha_{10}\left(\zeta_{H,d}\right) \equiv \frac{q_1}{q_0}. \tag{2.15}$$

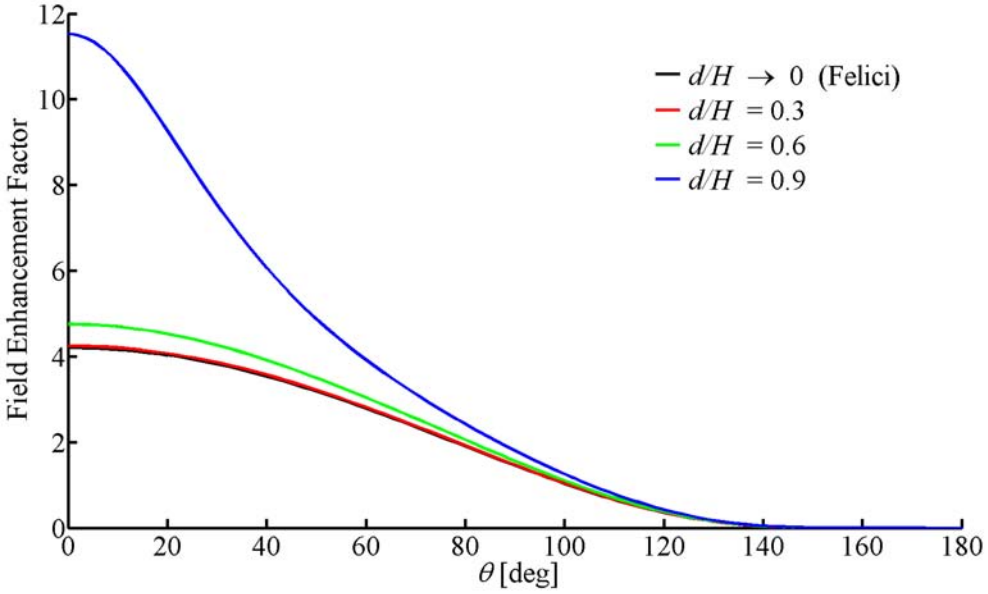

Figure 2.7: Electric field behavior at isolated particle surface for planar diode. Field enhancement factor increases with increasing d/H. The curve for $d/H \rightarrow 0$ essentially overlaps the $d/H = 0.3$ curve.

Figure 2.8 shows the dependence of α_{10} (i.e., $R/d \rightarrow \infty$) with d/H. For $d/H \leq 0.5$, α_{10} is within 5% of unity (i.e., exact agreement with Félici's model) and increases rapidly for larger d/H. In the presence of proximal particles, the effective charging factor is reduced, with closer proximal particles yielding greater reductions in the effective charging factor.

Figure 2.9 shows representative proximal-particle surface electric fields for the central particle in a planar diode. For $R/d \rightarrow \infty$, the isolated-particle results in Figure 2.7 are recovered, thus serving to validate the simulations. As particle separation decreases, the surface electric field also decreases. The presence of proximal particles thus results in a particle charge $q_{1p} < q_1$, the particle charge when in isolation.

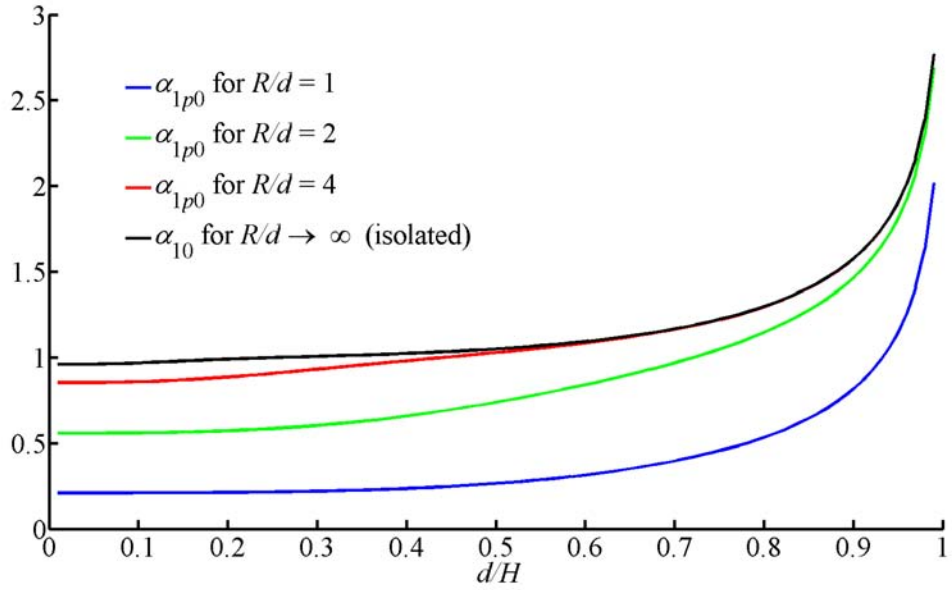

Figure 2.8: Charging factors for planar diode vs. *d*/*H*. A unity charging factor exactly agrees with Félici's model.

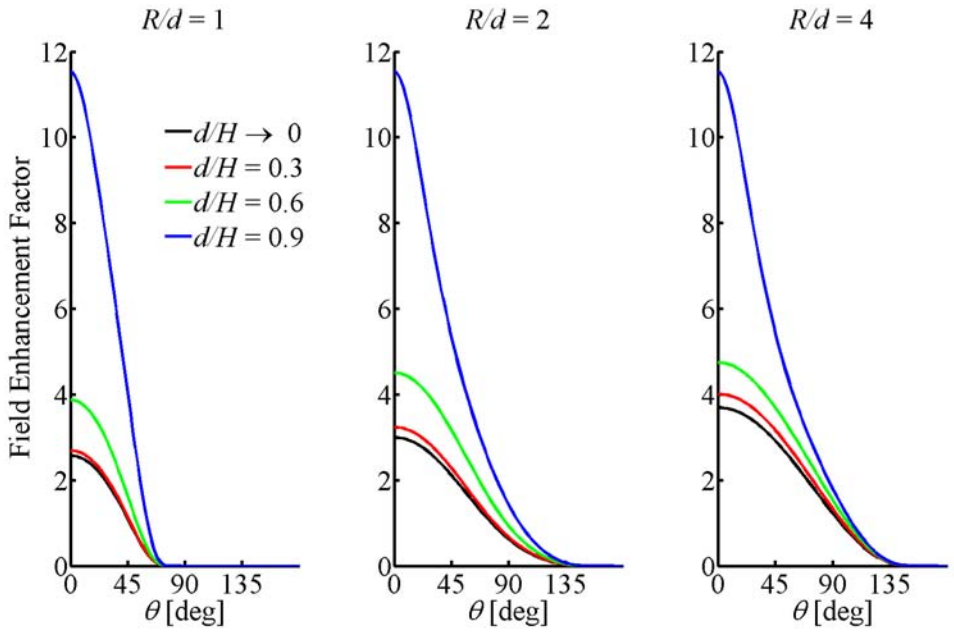

Figure 2.9: Electric field behavior at central particle's surface for proximal-particle planar diode. Field enhancement factor increases with increasing R/d.

This decrease in particle charge due to proximal particles is represented by the planar-diode proximal-particle charging factor α_{1p}, defined as

$$\alpha_{1p}\left(\zeta_{R,d}\right) \equiv \frac{q_{1p}}{q_1}, \tag{2.16}$$

which is only a function of R/d. The net planar-diode proximal-particle charging factor is thus α_{1p0}, defined as

$$\alpha_{1p0}\left(\zeta_{H,d}, \zeta_{R,d}\right) \equiv \frac{q_{1p}}{q_0} = \alpha_{1p}\left(\zeta_{R,d}\right)\alpha_{10}\left(\zeta_{H,d}\right), \tag{2.17}$$

with its dependence on d/H and R/d shown in Figure 2.8 and Figure 2.10, respectively.

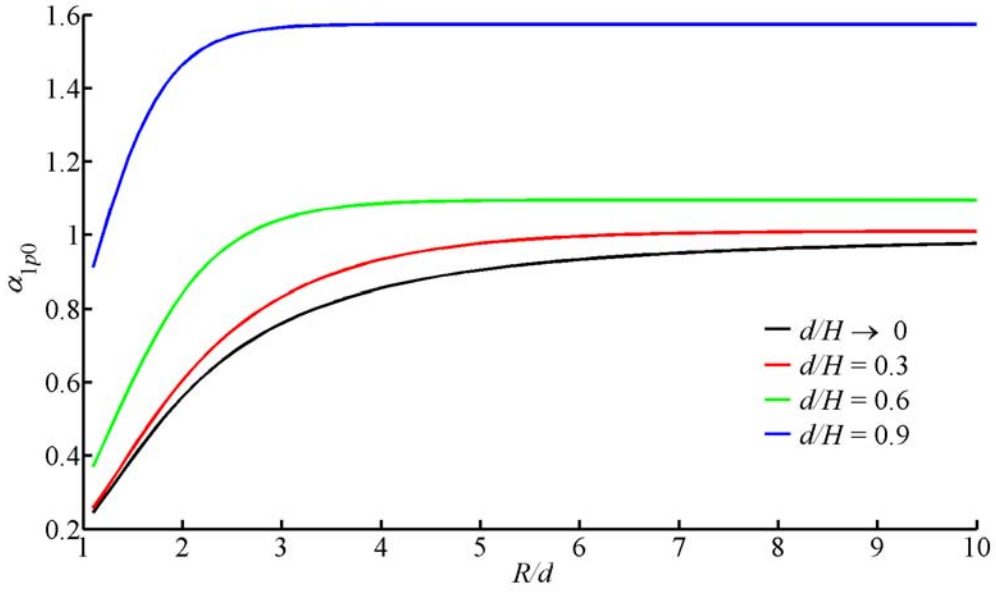

Figure 2.10: Net charging factors for planar diode vs. *R/d*. A unity charging factor exactly agrees with Félici's model.

While large values of d/H are desirable to maximize particle charge in a planar diode, caution is needed to avoid exceeding E_{max} due to the rapid increase in the maximum surface electric field. Large values of R/d are also desirable, with a fixed d/H configuration acquiring over 90% of its isolated-particle charge for $R/d \geq 5$.

2.4.2 Gated Diode

Figure 2.11 shows representative isolated-particle surface electric fields in a gated diode. In general, the peak electric field occurs at the particle tip ($\theta = 0$). Exceptions occur for $d/H > 0.6$ and $D/H < 3$, where the edges of the gate orifice approach the particle surface and effects due to the gate thickness are apparent. At a given particle size (i.e., fixed d/H), the surface electric field decreases as the gate orifice diameter increases (i.e., aspect ratio D/H increases). The results for a planar diode are recovered for $D/H \rightarrow 0$, thus serving to validate the simulations.

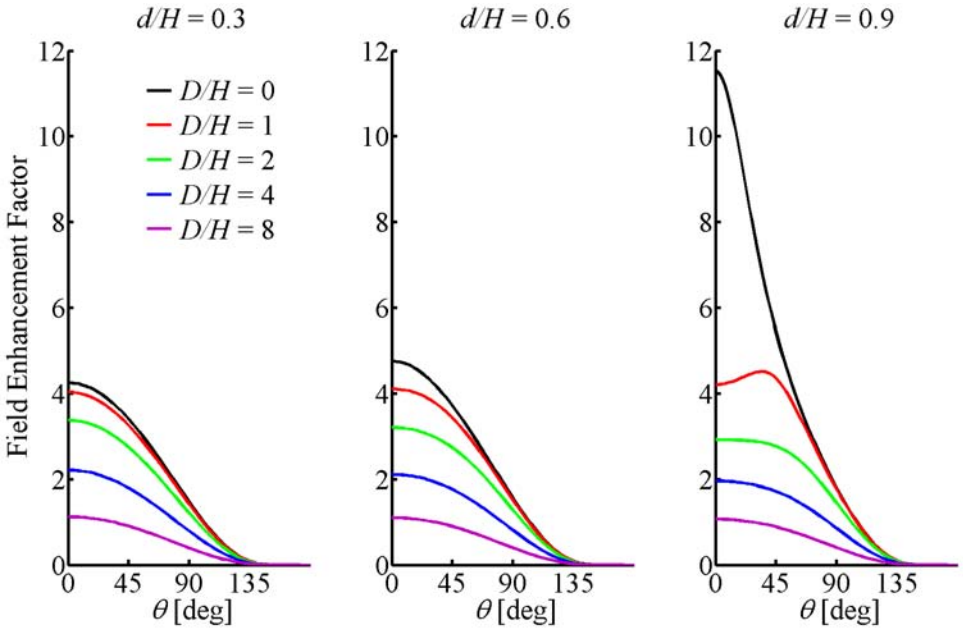

Figure 2.11: Electric field behavior at isolated particle surface for gated diode. Field enhancement factor decreases with increasing D/H.

The presence of the gate orifice results in a particle charge $q_2 < q_1$, the particle charge with no gate orifice. This decrease in contact charging is represented by the gated-diode isolated-particle charging factor α_{21}, defined as

$$\alpha_{21}\left(\zeta_{D,d},\zeta_{H,d}\right) \equiv \frac{q_2}{q_1}, \tag{2.18}$$

which is shown in Figure 2.12. For a given particle size d and diode spacing H, α_{21} decreases with larger gate orifice diameters (i.e., smaller d/D); for a given particle size and gate orifice diameter D, α_{21} increases with larger diode spacing (i.e., smaller D/H). Thus, for a given particle size, a smaller gate aspect ratio D/H yields a greater charging factor. As an example, $d/H < 0.3$ results in $\alpha_{21} > 0.96$ for aspect ratios less than unity. Two distinct regimes exist for a given gate aspect ratio: α_{21} is essentially constant for small particles (i.e., small d/H) and decreases rapidly for $d/H > 0.6$.

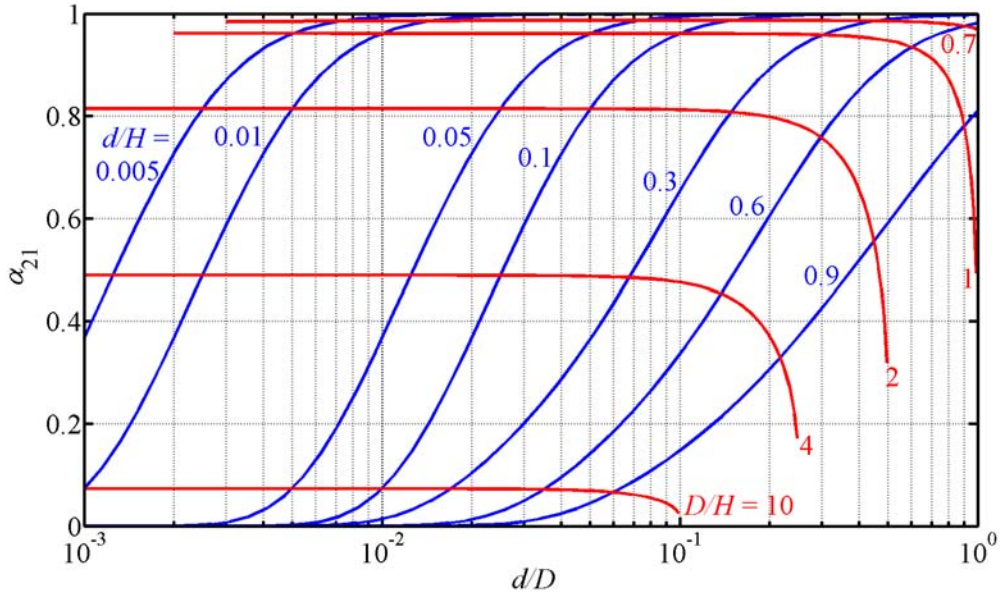

Figure 2.12: Isolated-particle charging factor for gated diode. Particle extraction is possible for $d/D < 1$.

The acquired charge q_2 for an isolated particle in the gated diode configuration depends on the net gated-diode isolated-particle charging factor α_{20}, defined as

$$\alpha_{20}\left(\zeta_{D,d},\zeta_{H,d}\right) \equiv \frac{q_2}{q_0} = \alpha_{21}\alpha_{10}. \tag{2.19}$$

As shown in Figure 2.13, α_{20} is insensitive to d/H for $d/H \leq 0.5$ or $D/H > 1$. α_{20} decreases with increasing aspect ratio (i.e., increasing D/H); equivalently, for a given particle size and diode spacing, α_{20} decreases for larger gate orifice diameters. While having both large d/H and small D/H provide a net charging factor greater than unity, caution is needed due to the large field enhancement and the increased risk of gate-particle shorting in these cases. A more conservative approach to optimizing the net charging factor would be to have $d/H \leq 0.5$ and $D/H \leq 1$.

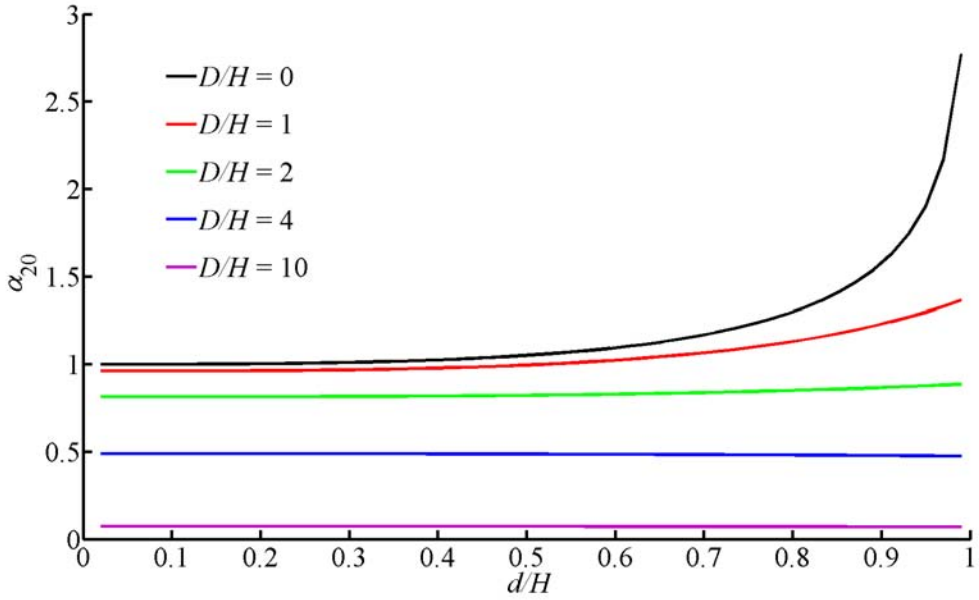

Figure 2.13: Net isolated-particle charging factor for gated diode. A unity charging factor exactly agrees with Félici's model.

The decrease in particle charge due to proximal particles is represented by the gated-diode proximal-particle charging factor α_{2p}, defined as

$$\alpha_{2p}\left(\zeta_{R,d}\right) \equiv \frac{q_{2p}}{q_2}, \tag{2.20}$$

which is only a function of R/d. The net gated-diode proximal-particle charging factor is thus α_{2p0}, defined as

$$\alpha_{2p0}\left(\zeta_{D,d},\zeta_{H,d},\zeta_{R,d}\right) \equiv \frac{q_{2p}}{q_0} = \alpha_{2p}\left(\zeta_{R,d}\right)\alpha_{20}\left(\zeta_{D,d},\zeta_{H,d}\right). \tag{2.21}$$

Figure 2.14 shows representative net proximal-particle charging factors for a planar and gated diode. For $R/d \to \infty$, the isolated-particle results are recovered for both diode configurations, thus serving to validate the simulation. As with the isolated-particle cases, the presence of the gate orifice serves to lower the net charging factor, with larger orifices resulting in lower charging.

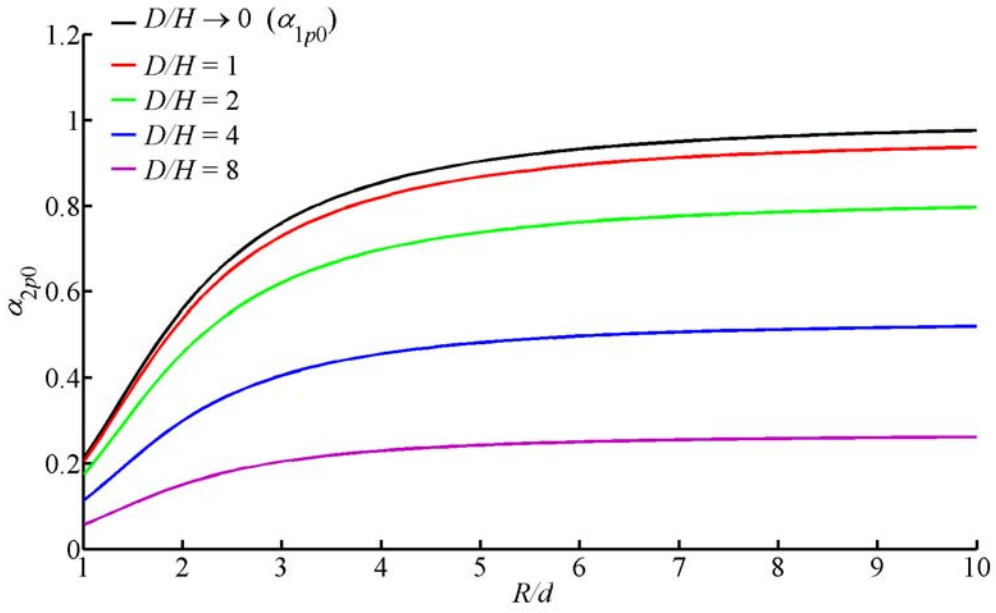

Figure 2.14: Net proximal-particle charging factors for planar and gated diodes. $d/H = 0.05$ for all configurations.

2.4.3 Gate-Sieve Diode

Figure 2.15 shows representative isolated-particle surface electric fields in a gate-sieve diode. As more of the particle becomes exposed above the sieve plane, the surface electric field increases across more of the particle surface. For $z/d \rightarrow 1$ (i.e., fully exposed particle), the results approach expectations for a gated diode, thus serving to validate the simulations. Configurations with $z/d > ½$ are physically realizable by having particles below but in contact with the sieve pushing up on the test particle.

The decrease in particle charge due to lack of exposure is represented by the gate-sieve-diode isolated-particle charging factor α_{32}, defined as

$$\alpha_{32}\left(\zeta_{z,d}\right) \equiv \frac{q_3}{q_2}, \tag{2.22}$$

which is only a function of z/d. The net gate-sieve-diode isolated-particle charging factor is thus α_{30}, defined as

$$\alpha_{30}\left(\zeta_{D,d}, \zeta_{H,d}, \zeta_{z,d}\right) \equiv \frac{q_3}{q_0} = \alpha_{32}\left(\zeta_{z,d}\right)\alpha_{20}\left(\zeta_{D,d}, \zeta_{H,d}\right). \tag{2.23}$$

Figure 2.16 is a representative plot of α_{30}, with charging greatly reduced by the effects of sieve obscurement; the unity aspect ratio configuration only has $\alpha_{30} = 0.44$ when the upper hemisphere of a particle is exposed (i.e., $z/d = 0.5$), and $\alpha_{30} > 0.9$ requires that $z/d > 0.94$ (i.e., essentially full exposure).

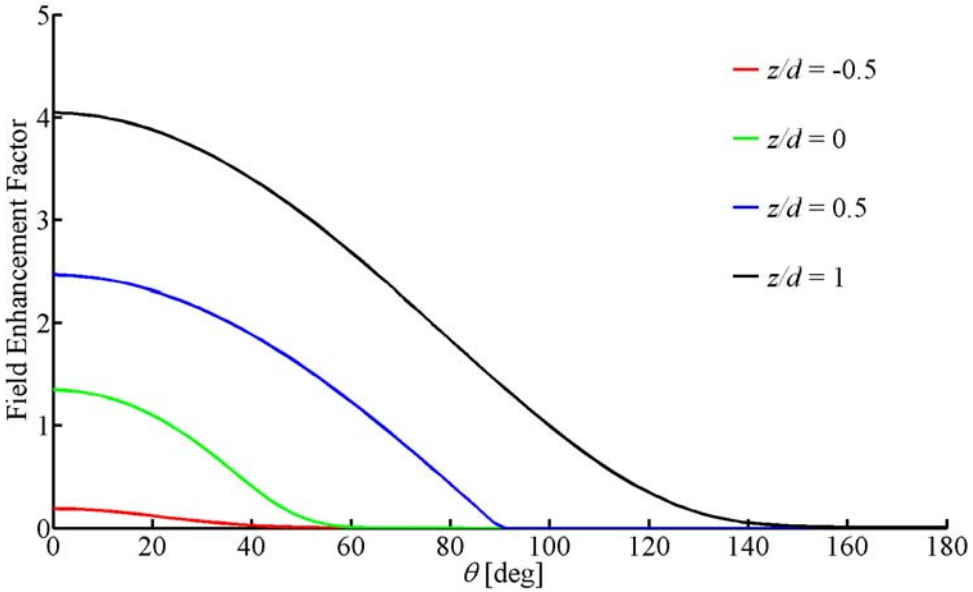

Figure 2.15: Electric field behavior at isolated particle surface for gate-sieve diode. Unity gate aspect ratio and $d/H = 0.3$ for all configurations.

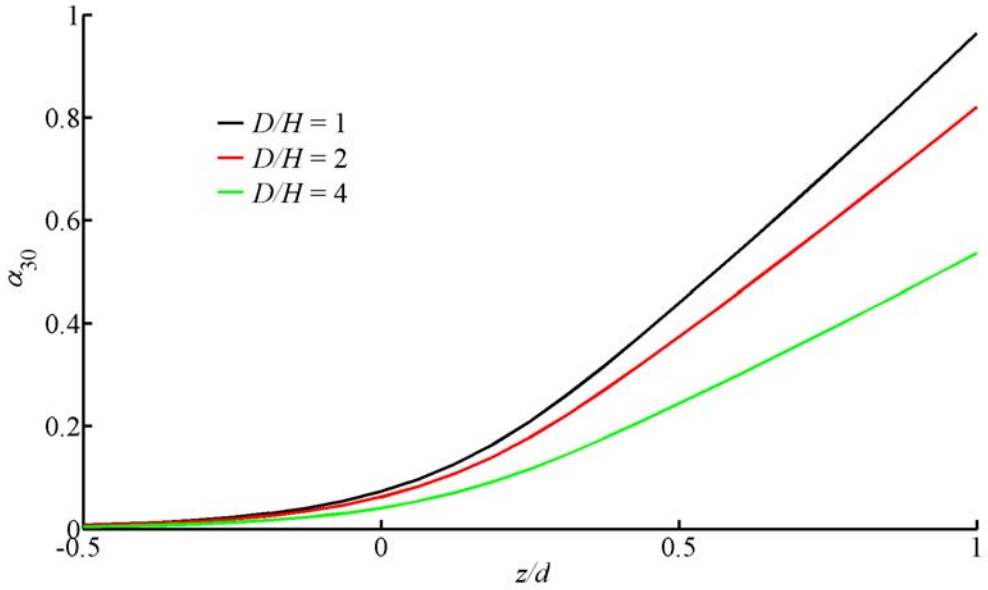

Figure 2.16: Net isolated-particle charging factor for gate-sieve diode. $d/H = 0.1$ applies for all configurations.

2.5 Implications for NanoFET

The electrostatic simulations on the various diode configurations provide gate design considerations for optimizing particle charge in physical NanoFET charging

stages. While large values of d/H maximize the acquired charge, the corresponding high field enhancement factors require caution to avoid exceeding E_{max}; in addition, larger values of d/H also increase the risk of gate-particle shorting. A more conservative optimization approach would be to have $d/H \leq 0.5$ and minimize the adverse charging effects due to the gate orifice, proximal particles, and sieve obscurement; this approach seeks to preserve a unity net charging factor. Since $D/H \gg 1$ suffer reduced charging levels and $D/H \ll 1$ is difficult to fabricate, having $D/H \sim 1$ is a reasonable compromise. Because $R/d < 5$ suffers reduced charging levels, an optimum extractor gate would have an emitter-to-emitter spacing (i.e., pitch) of at least five particle diameters; $R/d > 10$ may be undesirable because it provides little additional benefit to charging while decreasing NanoFET's thrust density. Charged particles should also be extracted upon full exposure from the charging sieve to maximize charging.

Chapter 3

Vibration-Assisted Extraction of Particles

For particles to be extracted after charging, the adhesive and cohesive forces holding the particles to the charging electrode and to each other must be overcome. Consider a rigid, spherical particle of diameter d at a surface-to-surface separation distance z_s from another entity (e.g., another particle or a plane surface). The resulting attractive van der Waals force F_V is

$$F_V\left(z_s\right) = \frac{H_A}{12\left(1+\delta_{ij}\right)}\frac{d}{z_s^2}, \tag{3.1}$$

where H_A is the Hamaker constant of the materials and δ_{ij} is the Kronecker delta, in which $\delta_{ij} = 1$ for particle-particle interactions (i.e., cohesion) and $\delta_{ij} = 0$ for particle-plane interactions (i.e., adhesion); Equation (3.1) is applicable in the small separation limit, where the separation distance is much smaller than the particle diameter (i.e., $z_s \ll d$) [46]. The closest surface-to-surface separation distance z_{s0} is typically set at 0.4 nm [47], yielding the maximum van der Waals force $F_V(z_s = z_{s0})$.

Because the van der Waals force is conservative (i.e., $F = -dU/dx$, for conservative force F, potential energy U, and displacement x), the resulting potential energy U_V in the system is

$$U_V\left(z_s\right) = -\frac{H_A}{12\left(1+\delta_{ij}\right)}\frac{d}{z_s}, \tag{3.2}$$

in which $U_V(z_s \to \infty) = 0$. To completely remove the particle from the plane surface, an amount of work equivalent to $-U_V(z_s = z_{s0})$ must be done. Figure 3.1 shows a representative interaction between a particle and a plane surface, both of which are metals.

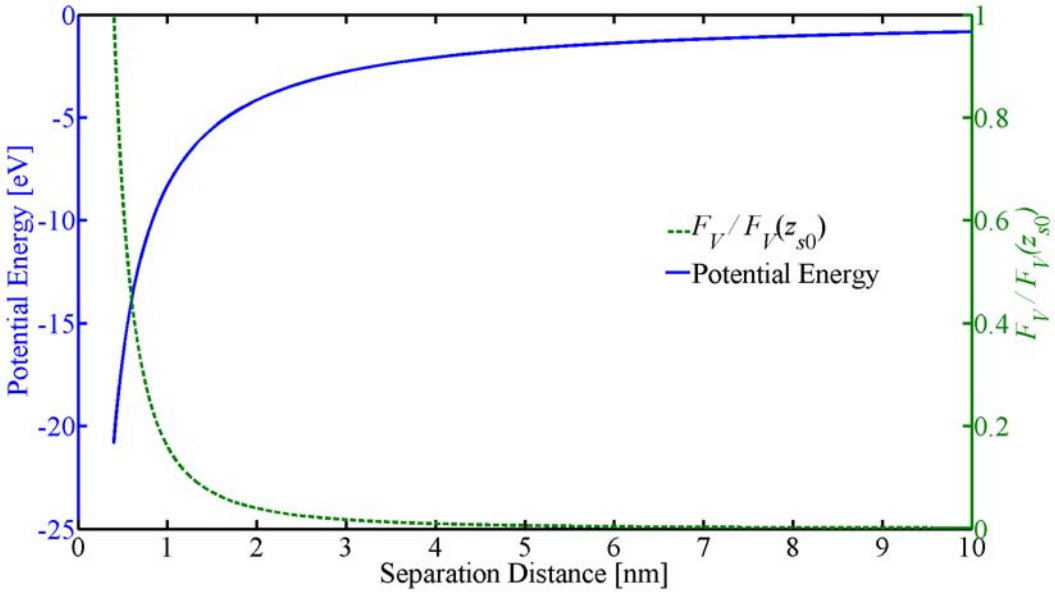

Figure 3.1: Particle-plane van der Waals interaction. For the 50-nm particle with z_{s0} = 0.4 nm, $H_A \sim 2$ eV is used to represent metal-to-metal contact (Reference 47).

In NanoFET, the kinetic energy acquired by a charged particle upon extraction and acceleration is $K = qV_o$. Comparing the work required to remove the particle to the particle kinetic energy yields

$$\frac{-U_V(z_{s0})}{K} = \frac{H_A}{2(1+\delta_{ij})z_{s0}\alpha_0 \varepsilon E_c V_o} d^{-1}, \tag{3.3}$$

where α_0 is the net particle charging factor discussed in Chapter 2, ε is the permittivity of the ambient environment, E_c is the charging electric field, and V_o is the operating voltage. Consider a baseline NanoFET configuration in which d = 50 nm, E_c = 400 V/μm,

V_o = 40 kV, and α_0 is approximately unity; the corresponding ratio of energies for $H_A \sim 2$ eV and $z_{s0} = 0.4$ nm is $-U_V/K \sim 10^{-5}$. Thus, the energy required to overcome adhesive and cohesive forces is a small fraction of the final particle kinetic energy; for NanoFET, this small fraction suggests the potential for high thrust efficiency. As discussed in Chapter 4.1, use of lower density and hollow particles would enable larger particles to be used to meet a given specific impulse target; adhesion and cohesion issues are less significant for these larger particles, thus improving the propellant's dry storage capability and reducing the risk of feed system jamming in NanoFET.

3.1 Electrostatic Liftoff of Particles

Consider a charged particle in contact with a planar electrode. The electrostatic force F_E acting on the particle is

$$F_E = \gamma_c q E_c = \gamma_c \alpha_0 \frac{\pi^3}{6} \varepsilon E_c^2 d^2, \tag{3.4}$$

with $\gamma_c = 0.832$ to account for the image charge effect [38]. A gravitational force F_G, including the effects of buoyancy, acts on the particle as

$$F_G = \frac{\pi}{6}(\rho - \rho_0) g d^3, \tag{3.5}$$

where ρ is the particle mass density, ρ_0 is the mass density of the ambient environment, and g is the gravitational acceleration. The minimum electric field required for particle liftoff from the electrode satisfies

$$E_L^2 = \frac{1}{\pi^2}(\gamma_c \alpha_0 \varepsilon)^{-1} \left[\frac{1}{2\pi(1+\delta_{ij})} \frac{H_A}{z_{s0}^2} d^{-1} + (\rho - \rho_0) g d \right]. \tag{3.6}$$

As particle size decreases, the gravitational contribution becomes negligible, and $E_L \propto d^{-1/2}$. Thus, higher electric fields are necessary to lift off smaller particles. For a 50-nm, metalized (i.e., $H_A \sim 2$ eV) particle, the minimum required liftoff electric field is ~300 V/μm. Since $E_L \propto H_A^{1/2}$ and $E_L \propto z_{s0}^{-1}$ for small particles, the liftoff threshold electric field can be decreased by lowering the Hamaker constant with a different material combination or by increasing the separation distance via a surface coating. Figure 3.2 shows representative electric field thresholds. For bipolar operations, NanoFET's baseline charging field is 400 V/μm, which appears sufficient to extract optimally charged particles > 30 nm in diameter.

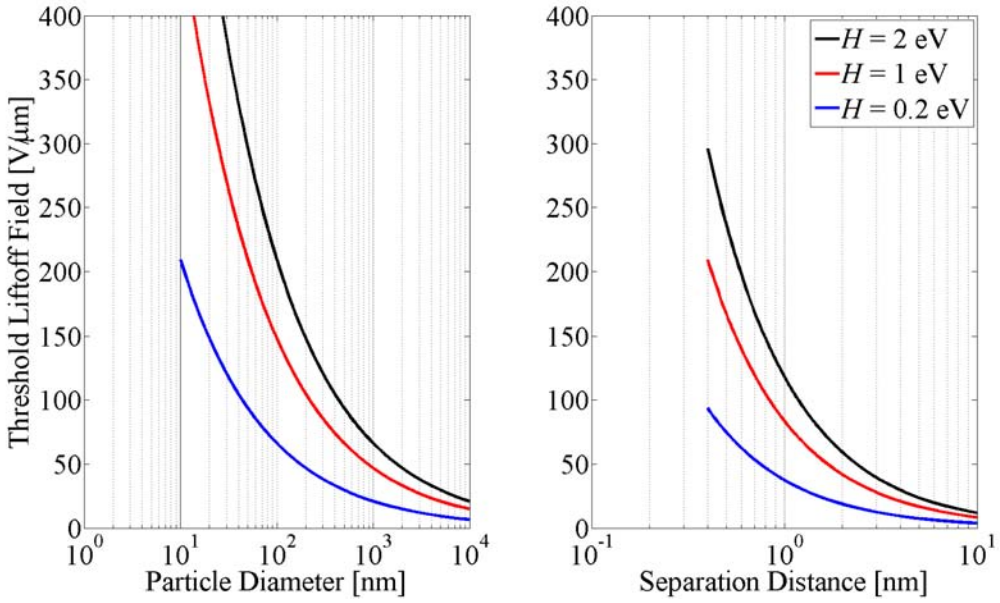

Figure 3.2: Threshold electric field for particle liftoff from plane electrode. Particles are assumed to be optimally charged (i.e., approximately unity net charging factor). (*Left*) $z_{s0} = 0.4$ nm. (*Right*) $d = 50$ nm.

3.2 Effect of Inertial Forces

Application of an inertial force $F_I = ma_I$, where $m = \pi\rho d^3/6$ is the particle mass and a_I is the inertial acceleration, to the charged particle-electrode system reduces the liftoff threshold by

$$\Delta E_L^2 = \frac{1}{\pi^2}\frac{\rho a_I}{\gamma_c \alpha_0 \varepsilon} d. \tag{3.7}$$

A greater reduction in the liftoff threshold occurs for more massive particles and larger applied inertial accelerations. In an inertial reference frame, this inertial force may be imparted to the particle by accelerating the charging electrode. Piezoelectric actuators, devices that undergo mechanical deformation due to crystalline polarization effects when subjected to an applied electric field, represent an attractive means of generating such accelerations due to their high spatial resolutions, quick response times, low power consumption, and compact form factors. For a piezoelectric undergoing sinusoidal oscillations (i.e., $a_I = 4\pi^2 f^2 x_{\mathrm{PZT}}$), the corresponding liftoff threshold reduction is

$$\Delta E_L^2 = \frac{4\rho x_{\mathrm{PZT}} f^2}{\gamma_c \alpha_0 \varepsilon} d, \tag{3.8}$$

where x_{PZT} and f are the oscillation peak-to-peak amplitude and frequency, respectively.

Past studies have shown the feasibility of using piezoelectrics to move micro-particles [48]. Equating the inertial force provided by a piezoelectric with Equation (3.1) yields the threshold inertial acceleration a_I^* required to overcome van der Waals forces:

$$a_I^* = \frac{1}{2\pi\left(1+\delta_{ij}\right)}\frac{H_A}{\rho z_{s0}^2} d^{-2}. \tag{3.9}$$

This threshold acceleration is smaller for more massive particles, since $a_I^* \propto (\rho d^2)^{-1}$. Less inertial acceleration is also needed for smaller Hamaker constants, since $a_I^* \propto H_A$, and larger surface-to-surface separation distances, since $a_I^* \propto z_{s0}^{-2}$.

Relying on just inertial forces to manipulate nano-particles is more challenging compared to micro-particles due to the decreased particle mass. For example, to overcome inter-particle cohesive forces for a 50-nm, metal particle (i.e., $H_A \sim 2$ eV) with $z_{s0} = 0.4$ nm, $\sim 10^8$ g of inertial acceleration must be supplied; this level of acceleration corresponds to a piezoelectric operating at $x_{\mathrm{PZT}} = 1$ μm and $f \sim 10$ MHz. Such high frequency demands may be impractical, both from mechanical limits due to the high dynamic forces as well as current limitations, since the piezoelectric's current draw I_{rms} scales linearly with frequency as

$$I_{\mathrm{rms}} = \frac{\pi}{\sqrt{2}} C_{\mathrm{PZT}} V_{\mathrm{PZT}} f, \tag{3.10}$$

where C_{PZT} and V_{PZT} are the capacitance and peak-to-peak voltage bias for the piezoelectric, respectively [49].

Less demanding piezoelectric operational requirements are possible if the particles are coated so as to increase z_{s0}. In the above example, adding a 4-nm-thick coating to the particles (i.e., $z_{s0} = 8$ nm) decreases the frequency requirement to ~1 MHz. For NanoFET, frequency requirements to ensure particle passage through the charging sieve may be further reduced due to the presence of strong charging electric fields to provide an electrostatic force at the sieve. High inertial accelerations may also be achievable at lower frequencies by using non-sinusoidal waveforms for piezoelectric actuation.

3.3 Proof-of-Concept Experiment

The experimental setup for examining a piezoelectric-driven charging electrode is shown in Figure 3.3. The charging electrode consisted of a 100-mm diameter, 500-μm-thick glass wafer on which a 300-nm-thick layer of gold with a 30-nm thick chromium adhesion layer was deposited via plasma vapor deposition. Atomic force microscopy indicated that the roughness of the gold surface was about 20 nm. A Noliac CMAP09 piezoelectric actuator was mounted to the back of the glass wafer using epoxy. Charging electric fields were provided by suspending, at 1-cm separation in air, an identical wafer connected to an UltraVolt negative-polarity high-voltage power supply (HVPS). The entire electrode assembly was mounted on a vibration-isolated optical table.

The piezoelectric actuator's driving signal was provided by an Agilent 33220A arbitrary waveform generator, amplified via a Kepco BOP 100-2M bipolar operational power supply, and monitored with a Tektronix TDS2024B oscilloscope. During operations, health monitoring of the piezoelectric's current draw and capacitance was performed, and a thermocouple probe in contact with the actuator ensured that operational temperatures were kept well below the piezoelectric's Curie temperature of 350 °C, at which point the actuator loses its piezoelectric properties. Displacement of the charging electrode was measured with a Philtec D100 fiberoptic sensor. Due to the need to operate the sensor in the near field to obtain the necessary measurement sensitivity, the sensor was not used when a bias voltage was placed across the electrodes. Instead, the charging electrode's displacement upon activation of the piezoelectric actuator was checked before and after the experiment.

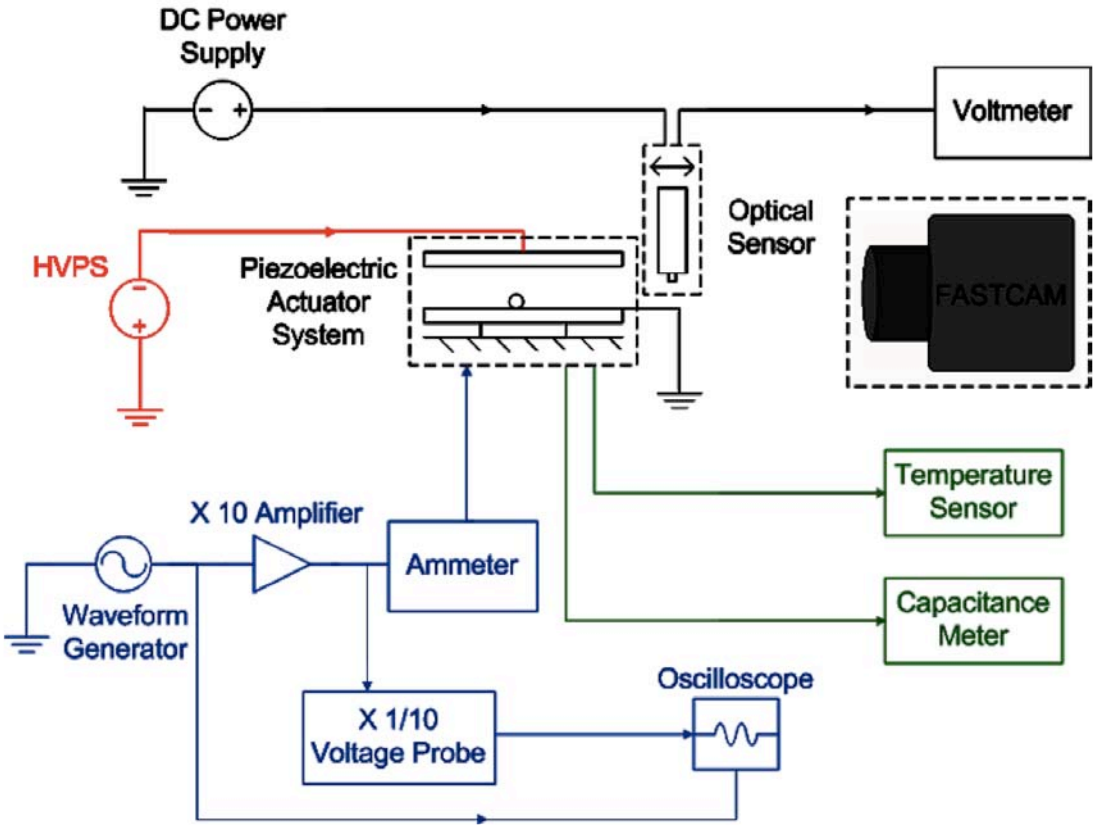

Figure 3.3: Block diagram of setup testing piezoelectric-driven charging electrodes. The open-loop setup required regular use of the fiberoptic sensor and the voltage probe to check the piezoelectric actuator's motion and driving signal, respectively.

The particles used in the experiments were silver-coated, soda-lime glass spheres from Mo-Sci Corporation with a diameter d of 196 ± 16 μm and mass density of 2.5 g/cm^3. Ten particles, as shown in Figure 3.4 (*top*), were placed on the charging electrode for each test run with center-to-center particle spacing R of 1.43 ± 0.03 mm; this spacing, which corresponds to $R/d \approx 7.3$ and a net charging factor of 0.95 (Figure 2.10), helped to minimize proximal particle effects. The use of multiple particles per test run provided a statistical means of accounting for variations in particle size and contact interface conditions. Particle dynamics following liftoff were monitored with a Photron FASTCAM-X 1024 PCI high-speed imaging system.

Particles were first allowed to charge in an electric field well below the liftoff threshold, and the electric field was then gradually raised throughout each test. Square pulses of rise time t_{rise} were sent to the piezoelectric actuator (Figure 3.4 (*bottom*)), resulting in effective inertial accelerations of approximately

$$a_I \approx \frac{x_{\text{PZT}}}{t_{\text{rise}} t_{99\%}}, \tag{3.11}$$

where $t_{99\%}$ is the settling time from the peak pulse overshoot to 99% of the nominal pulse height. These pulses were at a frequency of 10 Hz and 1% duty cycle, which is below the resonant frequency of the system, and the piezoelectric was kept within its linear operating regime. All tests were conducted under ambient conditions of 24 ± 1 °C and 49 ± 1% relative humidity.

As shown in Figure 3.5, particles remained in contact with the charging electrode until a large enough electric field, together with the applied inertial acceleration, was sufficient for particle lift off. At each acceleration test case, the particles displayed a wide range of liftoff electric fields, suggesting the impact of variations in local surface conditions as well as humidity effects that reduced the measured effective Hamaker constant (i.e., assuming that z_{s0} = 0.4 nm) to 0.14 eV; while this value is low by an order of magnitude compared to published results [50,51,52], one possible explanation is to consider the presence of an oxide coating or adsorbed materials that increase the effective surface-to-surface separation (e.g., an increase in z_{s0} to ~2 nm would be sufficient to account for the discrepancy in Hamaker values). Nevertheless, the data indicates general agreement with Equations (3.6) and (3.7) concerning the use of inertial forces to reduce the electric field liftoff threshold.

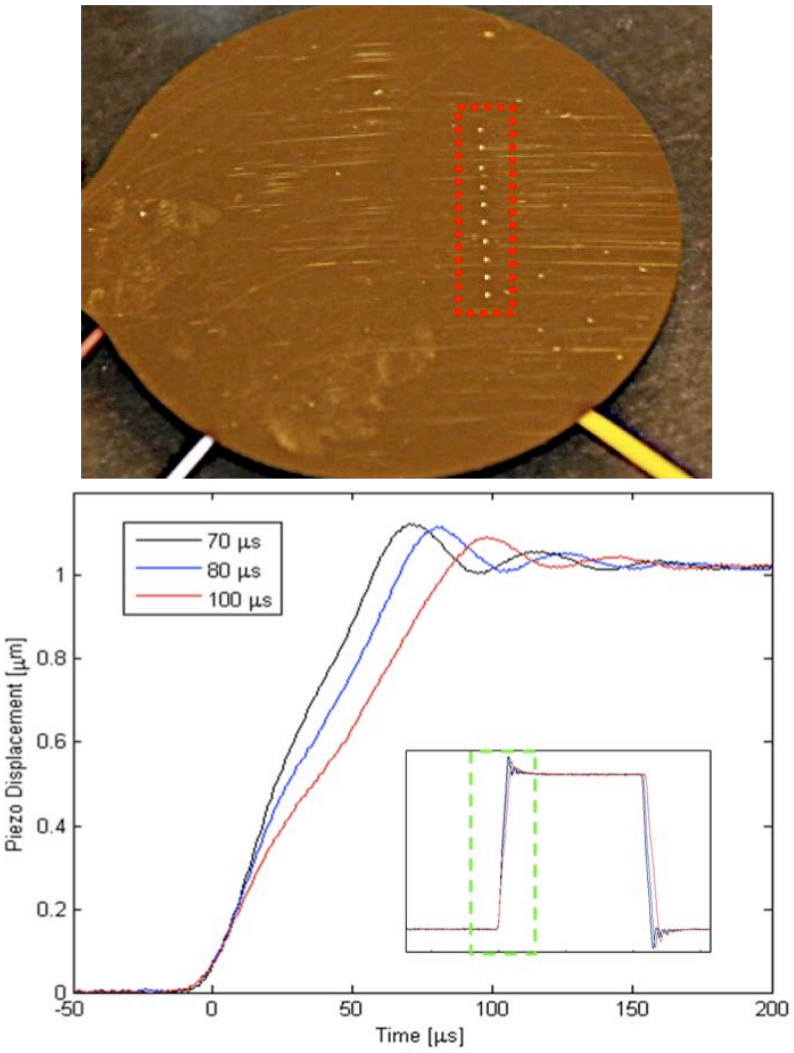

Figure 3.4: Piezoelectric-driven charging electrode experiment. (*Top*) Silver-coated glass spheres on gold electrode. (*Bottom*) Representative piezoelectric pulses and rise times used in experiment.

The large variability in liftoff thresholds seen in Figure 3.5 may be attributed to a number of factors. First, as previously discussed, the presence of surface impurities or oxide layers would modify the effective Hamaker constant as well as the surface-to-surface separation. Second, the distribution of particle sizes impacts the adhesive force, since $F_V \propto d$ per Equation (3.1). Third, surface roughness and relative orientation of the materials in contact can have significant impact on the van der Waals force [53].

Multiple points of contact due to surface features leads to an increase in the van der Waals force relative to Equation (3.1), as does surface deformations that increase the contact area.

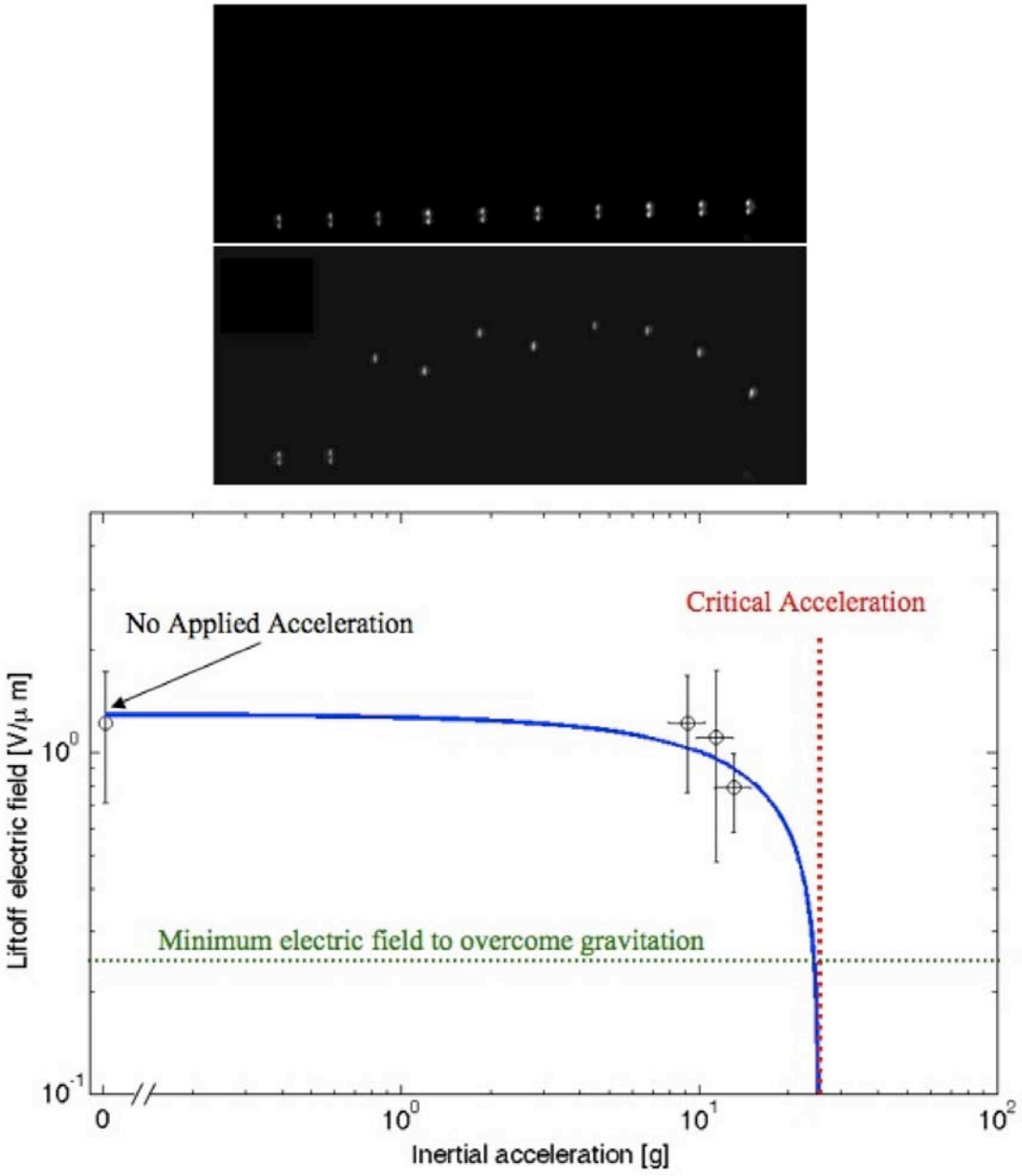

Figure 3.5: Charged particle liftoff with piezoelectric actuation. (*Top*) Particles charging on electrode without inertial acceleration. (*Center*) Particle liftoff following inertial acceleration. (*Bottom*) Reduction in liftoff electric field (averages with standard deviation) with inertial acceleration. Fitted curve is for effective H_A = 0.14 eV and z_{s0} = 0.4 nm.

3.4 Implications for NanoFET

Inertial forces from piezoelectrics provide a means of overcoming adhesive and cohesive forces in NanoFET to facilitate dry particle transport and controlled particle extraction from the charging sieve. Particles with small Hamaker constants are desirable, and concerns with premature particle liftoff (i.e., saturation charge not achieved) with small Hamaker constants are not great due to the generally fast characteristic charging times (e.g., $\sim 10^{-18}$ s for metals using Equation (2.6)).

While better transport of particles can be achieved at greater piezoelectric displacements and frequencies, care must be taken to avoid over-stressing the emitter array (e.g., mechanical fatigue, heating from piezoelectric dissipation, etc.) and to isolate the piezoelectric vibrations from the rest of the spacecraft. The available current limits from the spacecraft power supplies will also provide an upper bound on the allowable piezoelectric frequencies. Better propellant feeding may be accomplished in NanoFET by the use of non-sinusoidal waveforms for the piezoelectrics (i.e., pulsed operations) and the coating of particles (e.g., several nanometer thick layers) to increase the effective surface-to-surface separation distance. Such coatings must not substantially degrade the surface electrical conductivities of the particles lest they contribute to decreased charging (i.e., premature liftoff) or thrust efficiency (i.e., increased resistive losses during electrostatic charging).

Chapter 4

NanoFET System Performance Model

To evaluate the suitability of NanoFET designs for nano-satellite missions, a NanoFET system performance model is presented. As a case study, the three candidate 50-nm propellant summarized in Table 4.1 are examined with the performance model. The ceramic particles are assumed to be either semiconducting or coated with a conductive material (e.g., metal or carbon) to facilitate particle charging; if the ceramic particles are metalized, then all three particles would have similar inter-particle cohesion and sieve-particle adhesion effects. Depending on the specific impulse I_{sp} and thrust T needs, different propellant may be loaded into NanoFET to optimize the mission, thus giving mission designers flexibility.

The baseline NanoFET configuration maintains a constant electric field in the charging stage and assumes optimal charging (i.e., close to unity net charging factor per Chapter 2.5); the acceleration potential (e.g., up to 40 kV) and the piezoelectric frequency (e.g., up to 100 kHz) are variable for thruster throttling. A baseline charging electric field of 400 V/μm is chosen such that the peak surface electric field remains below the E_{max} value for electron field emission (i.e., ~10^3 V/μm); this electric field level allows for bipolar NanoFET operations. However, NanoFET particles at positive polarity may theoretically have charging fields that are an order of magnitude higher, thereby resulting in an order of magnitude increase in charge, to remain below the E_{max} value for ion field

evaporation (i.e., ~10^4 V/μm). Practically, the increased allowable charging fields for positively charged particles must remain below the electrical breakdown limits of the charging stage's insulator materials (e.g., ~10^3 V/μm for thin-film SiO_2 [54]).

Operating Mode	Material	Type	Specific Gravity
Low I_{sp} & High T	Gold	Solid	19.3
Intermediate I_{sp} & T	Ceramic	Solid	2.5
High I_{sp} & Low T	Ceramic	Shell	0.68

Table 4.1: Propellant candidates for NanoFET case study. Particles are at 50-nm diameter with hollow ceramic particles having 5% shell thickness relative to the particle diameter.

4.1 Specific Charge

Specific charge q/m is a performance driver for electrostatic propulsion systems such as NanoFET. Increasing the specific charge permits higher specific impulses to be attained for the same operating voltage or for a specific impulse target to be met at lower operating voltages. For a solid, spherical particle of mass m that acquires saturation charge q_0 via contact charging, use of Félici's charging model (Equation (2.5)) yields

$$\frac{q_0}{m} = \pi^2 \frac{\varepsilon E_c}{\rho_s d}, \tag{4.1}$$

where ε is the permittivity of the surrounding medium, E_c is the charging electric field, ρ_s is the solid particle's mass density, and d is the particle diameter. Smaller particles, less dense materials, and higher charging electric fields all result in higher specific charges.

While particles of the same size acquire the same charge during contact charging for a given electric field, a particle with lower mass density would acquire a higher specific charge. Lower mass density may also be achieved by using hollow rather than

solid particles; a hollow particle (with ρ_h as the mass density of the shell material and t_w as the shell wall thickness) has an effective mass density ρ given as

$$\rho = \rho_h \left[1 - \left(1 - 2\zeta_{t,d} \right)^3 \right], \tag{4.2}$$

where the normalized shell wall thickness $\zeta_{t,d}$ is defined as

$$\zeta_{t,d} \equiv \frac{t_w}{d}. \tag{4.3}$$

A solid particle corresponds to $t_w = d/2$.

The specific charge enhancement factor $\alpha_{q/m}$ for a hollow particle of shell wall thickness t_w compared to a solid particle of the same diameter d is

$$\alpha_{q/m} \equiv \frac{(q/m)_h}{(q/m)_s} = \frac{m_s}{m_h} = \frac{\rho_s}{\rho_h} \left[1 - \left(1 - 2\frac{t_w}{d} \right)^3 \right]^{-1}. \tag{4.4}$$

For t_w « d, the specific charge enhancement factor can be approximated as $\alpha_{q/m} \approx (6t_w/d)^{-1}$, which is within 10% of the true value for $t_w/d \leq 0.05$. The corresponding specific impulse enhancement factor α_{Isp} in an electrostatic propulsion system for a fixed operating voltage is

$$\alpha_{\mathrm{Isp}} \equiv \frac{(I_{\mathrm{sp}})_h}{(I_{\mathrm{sp}})_s} = \sqrt{\alpha_{q/m}}. \tag{4.5}$$

Both enhancement factors are shown in Figure 4.1. While having small t_w/d yields greater specific charge and specific impulse gains, consideration of the reduced mechanical robustness of thin-shell particles is necessary, since the particles would be subjected to compressive stresses in the propellant reservoir and inertial forces from the

piezoelectrics. Currently, solid or hollow ceramic (metalized [55] or semiconductor [56]) particles already exist with t_w/d approaching 5%.

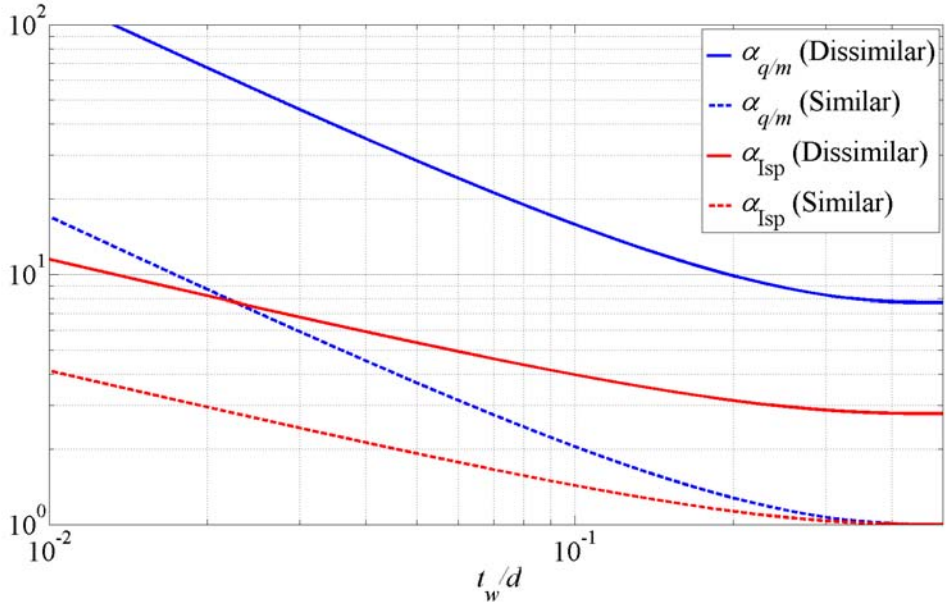

Figure 4.1: Enhancement of specific charge and specific impulse for hollow compared to solid particles. Dissimilar materials compare gold solid to ceramic shell particles.

Accounting for the use of hollow particles as propellant and the gate configuration's effect on particle charging (Chapter 2), Equation (4.1) can be modified to yield the theoretical specific charge q/m from a NanoFET emitter,

$$\frac{q}{m} = \alpha_0 \pi^2 \frac{\varepsilon E_c}{\rho d}, \tag{4.6}$$

where α_0 is the net charging factor. Figure 4.2 (*left*) shows NanoFET's theoretical specific charges, which increases with smaller or less dense particles.

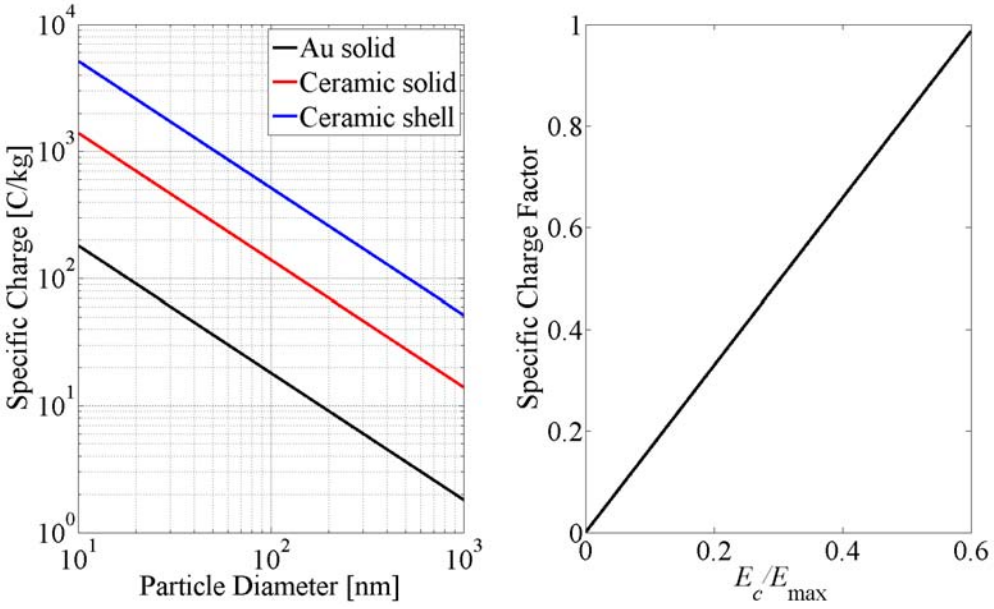

Figure 4.2: Theoretical NanoFET specific charges. (*Left*) Representative particles are optimally charged (i.e., approximately unity net charging factor) in 400-V/μm electric fields. (*Right*) Specific charge factor variation with charging electric field.

Using Equation (2.7), the theoretical maximum specific charge $(q/m)_{max}$ for a spherical particle occurs if a uniform surface field at E_{max} is present; this upper limit for the specific charge is

$$\left(\frac{q}{m}\right)_{max} = 6\frac{\varepsilon E_{max}}{\rho d}. \tag{4.7}$$

Comparing with Equation (4.6) results in a specific charge factor $\eta_{q/m}$ (Figure 4.2 (*right*)):

$$\eta_{q/m} = \alpha_0 \frac{\pi^2}{6}\frac{E_c}{E_{max}}. \tag{4.8}$$

At the baseline charging field E_c = 400 V/μm, the specific charge factor is $\eta_{q/m} \approx 0.66$ for negative-polarity particles. Compared to ions (e.g., a xenon ion has a specific charge of 7.5×10^5 C/kg), however, the particle propellants in NanoFET have much smaller

specific charges. Hence, NanoFET is naturally better suited for modest specific impulse applications.

4.2 Specific Impulse

Incorporating Equation (4.6) into Equation (1.10) yields the theoretical specific impulse I_{sp} from a NanoFET emitter as

$$I_{sp} = \frac{\pi\sqrt{2}}{g_0}\left(\frac{\alpha_0 \varepsilon E_c V_o}{\rho d}\right)^{\frac{1}{2}}, \tag{4.9}$$

with the net operating voltage V_o being the summation of the voltages from the charging (V_c) and acceleration (V_A) stages. Figure 4.3 shows NanoFET's theoretical specific impulses, which increases for smaller or less dense particles as $I_{sp} \propto (q/m)^{1/2}$. Because of the modest specific charges attainable by NanoFET, tens of kilovolts of operating voltage are necessary to achieve specific impulses of several hundred seconds or more. Note that in the case of particles at positive polarity, higher electric fields could again be applied; from Equation (4.9), the result would be higher specific impulses or lower operating voltages, since $I_{sp} \propto E_c^{1/2}$ and $V_o \propto E_c^{-1}$. For a fixed charging electric field and particle propellant, NanoFET becomes a variable-I_{sp} thruster by adjusting its operating voltage with $I_{sp} \propto V_o^{1/2}$ (Figure 1.4 (*left*)).

The density specific impulse I_d is defined as

$$I_d \equiv \frac{\rho}{\rho_{H2O}} I_{sp}, \tag{4.10}$$

where ρ_{H2O} is the mass density of water; equivalently, the density specific impulse is the product of the specific impulse with the propellant's specific gravity [57]. I_d is an indicator of how compact a propulsion system (i.e., propellant needs) is from a

volumetric standpoint. For mission architectures like nano-satellites that are volume-limited, a high density specific impulse means that more of the spacecraft's volume envelope is available for payload. Using Equation (4.9) yields

$$I_d = \frac{\pi\sqrt{2}}{\rho_{\mathrm{H2O}} g_0}\left(\frac{\alpha_0 \varepsilon E_c V_o \rho}{d}\right)^{\frac{1}{2}}, \tag{4.11}$$

in which $I_d \propto \rho^{1/2}$. As shown in Figure 4.3, NanoFET is expected to achieve high density-I_{sp} (i.e., > 1000 s) using high mass density propellants such as solid metal particles, compared to < 300 s for common monopropellants on small satellites [58].

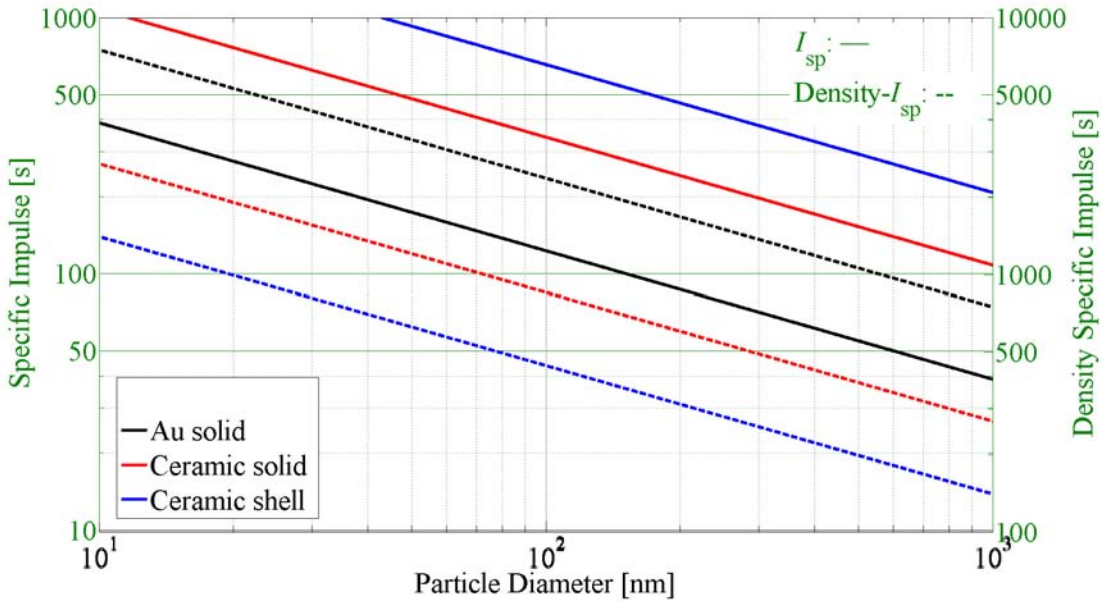

Figure 4.3: Theoretical NanoFET specific impulses. Representative particles are optimally charged (i.e., approximately unity net charging factor) in 400-V/μm electric fields with 40-kV operating voltage.

Accounting for particle packing within the propellant reservoir, the required volume V_p to house the propellant mass m_p is

$$V_p = \frac{m_p}{\eta_p \rho}. \tag{4.12}$$

The particle packing factor η_p for rigid spheres can be as high as $\pi/\sqrt{18} \approx 0.74$, as predicted by the Kepler conjecture [59] and manifested in either face-centered cubic or hexagonal close packing [60]. Experiments and numerical simulations of random close packing suggest a more realistic $\eta_p \sim 0.6$ [61,62,63,64,65].

From Equations (1.7) and (4.9), NanoFET can theoretically achieve, with fixed propellant mass fraction ξ_p, a mission velocity increment ΔV of

$$\Delta V = -g_0 I_{\mathrm{sp}} \ln\left(1-\xi_p\right) = \pi\sqrt{2}\left(\frac{\alpha_0 \varepsilon E_c V_o}{\rho d}\right)^{\frac{1}{2}} \ln\left(\frac{1}{1-\xi_p}\right). \tag{4.13}$$

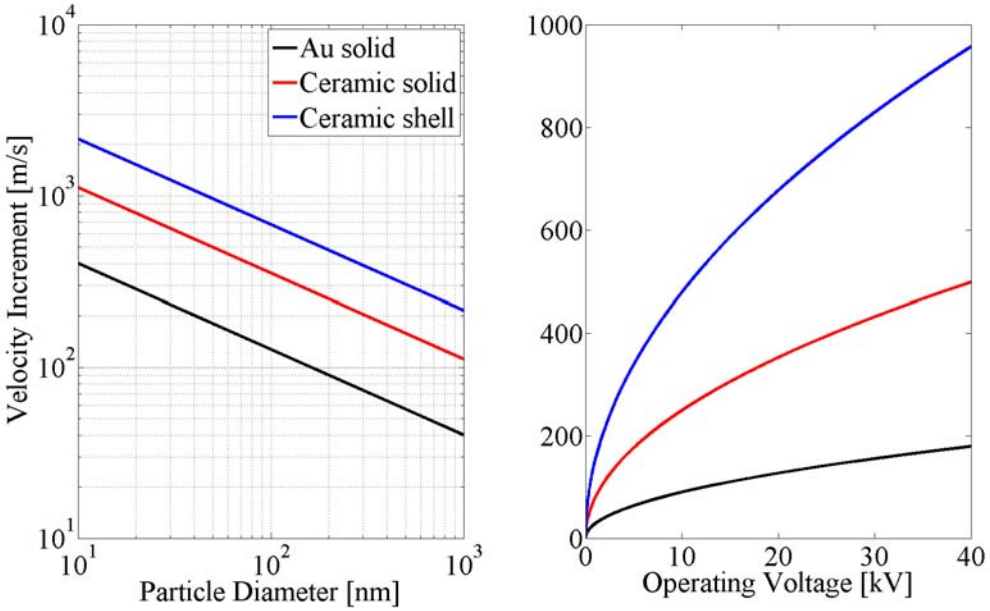

Figure 4.4: Theoretical NanoFET mission velocity increments. Representative particles are optimally charged (i.e., approximately unity net charging factor) in 400-V/μm electric fields with 10% propellant mass fraction. (*Left*) 40-kV operating voltage. (*Right*) 50-nm particles.

As shown in Figure 4.4, NanoFET's theoretical velocity increment increases with smaller or less dense particles. If higher specific impulses are achieved via higher charging electric fields or operating voltages, the resultant velocity increments would also

be higher, since $\Delta V \propto E_c^{1/2}$ and $\Delta V \propto V_o^{1/2}$. With only 10% of the spacecraft's wet mass devoted to propellant, NanoFET can theoretically achieve velocity increments that are hundreds of meters per second and in the regime of interest for nano-satellite missions.

4.3 Thrust

From Equation (1.9), NanoFET's modest specific impulses are expected to yield high thrust-to-power T/P performance, possibly > 1 mN/W (i.e., greater than existing electric propulsion systems). Incorporating Equation (4.9) yields

$$\frac{T}{P} = \frac{\sqrt{2}}{\pi}\left(\frac{\rho d}{\alpha_0 \varepsilon E_c V_o}\right)^{\frac{1}{2}} \eta_T, \tag{4.14}$$

where P is the input power to the thruster and η_T is the thrust efficiency.

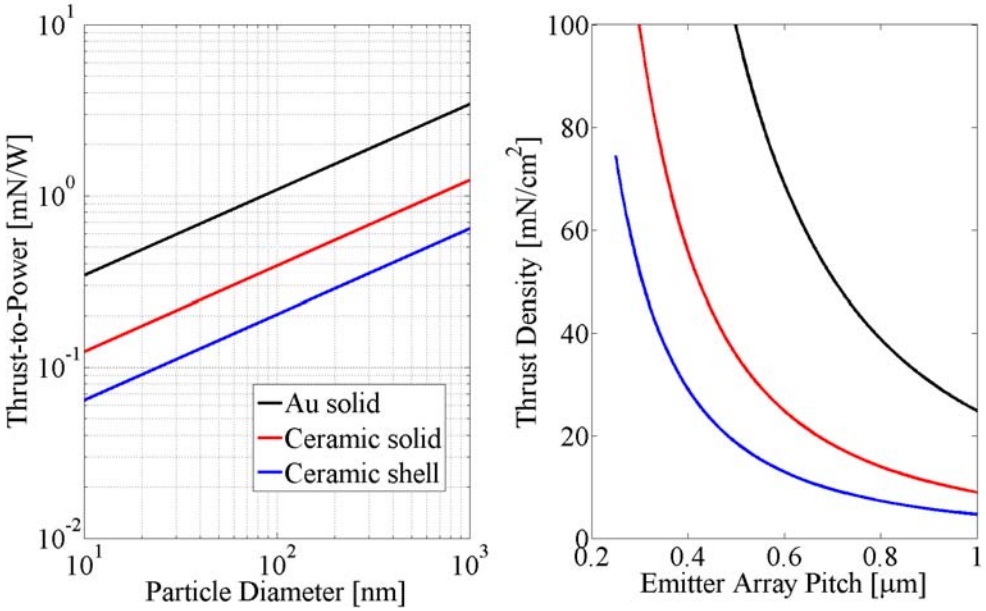

Figure 4.5: Theoretical NanoFET thrust characteristics. Representative particles are optimally charged (i.e., approximately unity net charging factor) in 400-V/μm electric fields with 40-kV operating voltage. (*Left*) Thrust-to-power for assumed 65% thrust efficiency. (*Right*) Thrust density limit for hexagonal array packing and 100-kHz piezoelectric frequency.

Figure 4.5 (*left*) shows NanoFET's theoretical thrust-to-power, which decreases with smaller or less dense particles. For a given propellant and thrust efficiency, the thrust-to-power ratio can be increased by lowering the charging electric field, since $T/P \propto E_c^{-1/2}$, or by lowering the operating voltage, since $T/P \propto V_o^{-1/2}$ (Figure 1.4 (r*ight*)).

The use of piezoelectrics to facilitate particle lift-off from the charging sieve also serves to regulate the mass flow rate of NanoFET. In general, the piezoelectric oscillation period (e.g., > 10 μs for frequency f < 100 kHz) is expected to be much greater than the time scales associated with particle charging (e.g., ~10^{-18} s for metals using Equation (2.6)) or transit through the gates (e.g., ~10 ns for 1-km/s particle to traverse a 10-μm gate stack). The piezoelectric oscillation period thus serves as the characteristic time scale for particle extraction. For a single NanoFET emitter, the extraction of a single particle per piezoelectric oscillation period means that Equation (1.1) becomes $T_0 = mfu_e$, where T_0 is the thrust per emitter, u_e is the characteristic exhaust velocity, and $\dot{m}_0 = mf$ is the mass flow rate per emitter, given as

$$\dot{m}_0 = \frac{\pi}{6}\rho d^3 f. \tag{4.15}$$

Incorporating Equations (1.5) and (4.9) results in

$$T_0 = \frac{\pi^2}{\sqrt{18}}\left(\alpha_0 \varepsilon E_c V_o \rho d^5\right)^{\frac{1}{2}} f. \tag{4.16}$$

The thrust thus increases with denser and larger particles along with higher charging electric fields, operating voltages, or piezoelectric frequencies. For a single emitter, the impulse T_0/f per piezoelectric actuation represents the minimum impulse bit. The total thrust of a NanoFET array housing N emitters is $T = NT_0$, and the total mass flow rate is $\dot{m} = N\dot{m}_0$, corresponding to an emission beam current of $I_b = \dot{m}q/m \propto d^2$. At constant

thrust and mass flow rate, Equation (1.3) gives the total achievable impulse from NanoFET as $I_t = Tm_p / \dot{m}$.

NanoFET's thrust density is dependant on the arrangement of the individual emitters in the overall array. For a regular array of area A in which the pitch (i.e., center-to-center spacing) of the arrays is R, the thrust density T/A is given as

$$\frac{T}{A} = \alpha_A \frac{T_0}{R^2}, \tag{4.17}$$

where α_A is the emitter packing factor; α_A is unity for a rectangular array and $2/\sqrt{3} \approx 1.15$ for a hexagonal array. Equation (4.17) provides an upper limit for the achievable thrust density; the actual thrust density would be lower to account for structural support elements in the array. Figure 4.5 (*right*) shows NanoFET's theoretical thrust density limit, which naturally decreases as emitters are spaced further apart (since $T/A \propto R^{-2}$) as well as with lower piezoelectric frequencies (since $T/A \propto f$). After accounting for the presence of structural support elements in the array, NanoFET may be capable of achieving $T/A \sim 1$ mN/cm^2. Having such high thrust densities is beneficial for nano-satellites, since it reduces the thruster's footprint and frees up spacecraft surface area for other uses (e.g., power generation, sensors, communications, etc.).

4.4 Thrust Efficiency

NanoFET's potential for high thrust-to-power is contingent on achieving high thrust efficiency. In NanoFET, the thrust efficiency η_T can be modeled as

$$\eta_T = \eta_\theta \eta_{\text{PZT}} \eta_{\text{misc}}, \tag{4.18}$$

where η_θ and η_{PZT} are efficiencies due to plume divergence and piezoelectric operations, respectively. η_θ for electrospray systems have been experimentally measured to be

> 98% [66]; NanoFET's divergence efficiency is expected to be comparable. η_{misc} represents other efficiency terms addressing issues such as polydispersity in the propellant specific charge due to non-optimal charging or particle size tolerances, particle losses to the MEMS gates during the extraction process, resistive losses during contact charging, frictional effects from particle passage through the charging sieve, and leakage current losses in the charging and acceleration stages; these additional loss mechanisms, together with the divergence efficiency, would need to be > 86% for NanoFET to be as efficient as electrospray systems utilizing ionic liquid EMI-BF_4 [67].

η_{PZT} is defined as

$$\eta_{\text{PZT}} \equiv \frac{P_T}{P_T + P_{\text{PZT}}}, \tag{4.19}$$

where P_{PZT} is the power dissipation of the piezoelectrics and P_T is the thrust power. Assuming that the piezoelectrics compose a plane layer adjoining the charging sieve, the power dissipation can be determined by considering the issue of power density. Combining Equations (1.9), (4.9), and (4.17) yields the thrust power density P_T/A as

$$\frac{P_T}{A} = \alpha_A \frac{P_{T0}}{R^2} = \frac{\pi^3}{6}\frac{\alpha_A}{R^2}\alpha_0 \varepsilon E_c V_o d^2 f, \tag{4.20}$$

where $P_{T0} = qV_o f$ is the thrust power per emitter. Equation (4.20) provides an upper limit for the achievable thrust power density; the actual thrust power density would be lower to account for structural support elements in the array. Figure 4.6 (*left*) shows NanoFET's theoretical thrust power density limit, which is independent of propellant material and decreases with emitters that are spaced further apart (since $P_T/A \propto R^{-2}$) as well as lower

piezoelectric frequencies (since $P_T/A \propto f$). After accounting for the presence of structural support elements in the array, NanoFET may be capable of achieving $P_T/A \sim 1$ W/cm^2.

Aktakka *et al.* fabricated and tested piezoelectric films that are representative of what is expected for NanoFET; squares of piezoelectric film (< 10-µm-thick) exhibited power dissipation densities of 0.3, 0.8, and 1.2 W/cm^2 for 16, 4, and 2-mm^2 films operated at resonance, respectively [68]. Figure 4.6 (*right*) shows the corresponding η_{PZT} (using Equations (4.19) and (4.20)) for NanoFET operations using such films; as the emitters are placed further apart, η_{PZT} decreases for a given piezoelectric film because of the decrease in thrust power density. The high values (i.e., $\eta_{PZT} > 0.9$) shown in Figure 4.6 (*right*) justifies the $\eta_T = 0.65$ assumption made in Figure 1.4 and Figure 4.5.

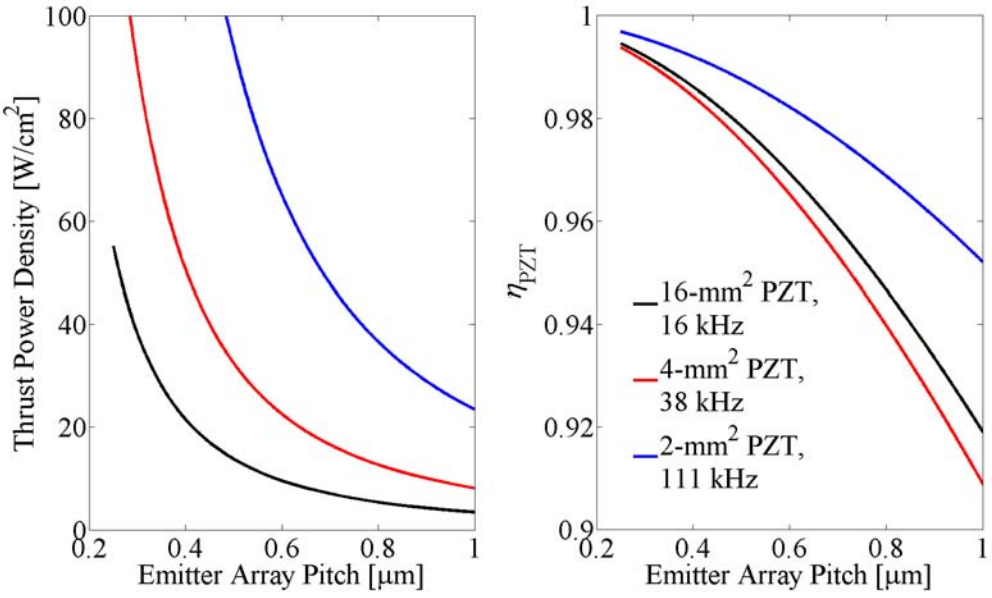

Figure 4.6: Theoretical NanoFET power characteristics. 50-nm particles are optimally charged (i.e., approximately unity net charging factor) in 400-V/µm electric fields with 40-kV operating voltage and hexagonal array packing. Piezoelectric data are from Reference 68. (*Left*) Thrust power density limit. (*Right*) Thrust efficiency effects due to piezoelectric operations.

4.5 Implications for NanoFET

Distinct operating regimes are apparent using the representative propellants in Table 4.1. To achieve high specific impulses comparable to colloidal thrusters (i.e., > 600 s), high specific charges are necessary. This high-I_{sp} regime is attractive for long duration missions and requires the use of hollow shell particles as well as the highest operating voltages. In contrast, larger or more massive particles are preferred for NanoFET to compete with cold gas thrusters or resistojets. This high-thrust mode is attractive for time-critical missions requiring high spacecraft accelerations.

By using both the operating voltage and the piezoelectric actuation as independent means of throttling the thruster, NanoFET has a large performance envelope that provides flexibility for mission optimization. The use of low-power piezoelectrics for propellant flow rate control allows for high thrust efficiency, high thrust-to-power, and the potential for high thrust resolutions and fine impulse bits during pulsed piezoelectric operations. Optimization of NanoFET's array design offers the potential for high thrust densities (i.e., ~ 1 mN/cm^2). This feature, coupled with a high density specific impulse, makes NanoFET attractive for surface area- and volume-limited nano-satellites.

Chapter 5

Micro-Particle Extractor Prototype

Prototyping efforts on the NanoFET concept first began with single-shot, millimeter-sized particle extractors similar to the test cells to be discussed in Chapter 6. While the particles used were orders of magnitude larger than what is envisioned for the actual NanoFET design, these simple, proof-of-concept prototypes enabled timely examination and improved understanding of the fundamental physics concerning NanoFET (e.g., particle charging and liftoff). With each set of prototypes, the relevant features (i.e., particles and sieves) continued to decrease in size. The focus of this chapter is on the first-generation micro-particle extractor prototype.

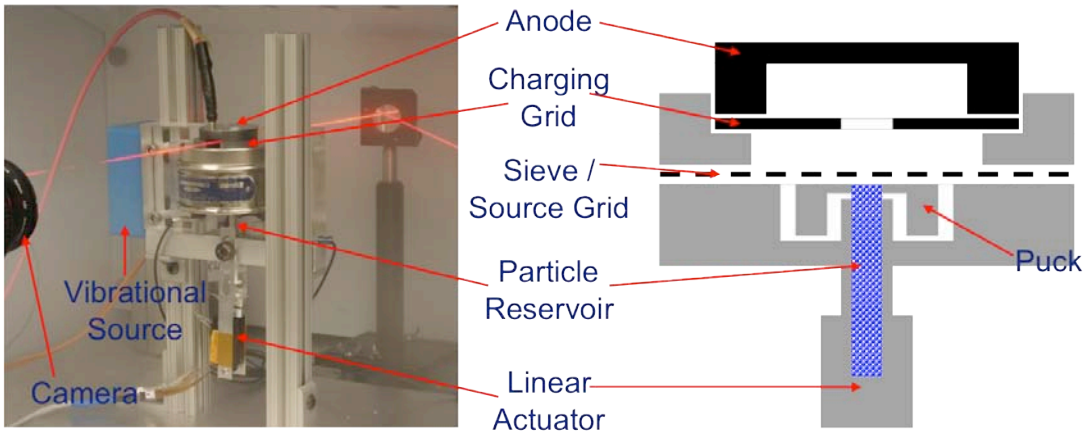

Figure 5.1: Zeroth-generation micro-particle extractor prototype. The removable collection anode was used to study deposited films from the extracted particles.

Figure 5.1 shows the first NanoFET-concept prototype (zeroth-generation) to charge and extract dry micro-particles. The charging sieve was formed from woven

stainless steel mesh with orifice feature sizes of ~20 μm. Within the syringe reservoir were 8-20 μm aluminum particles, which were compacted toward the charging sieve by a linear actuator displacing the syringe plunger. Force and displacement feedback for the linear actuator resulted in a relatively uniform compressive pressure ranging from 0.3 to 0.6 N/mm^2. To reduce sieve blinding, a solenoid-driven, polyvinyl chloride slide (i.e., puck) was swept along the bottom of the sieve at the syringe interface at ~1 Hz. Additional vibration of ~0.1 *g* was supplied to the prototype mount by a motor to further reduce sieve blinding. During operations, the charging sieve was kept at common ground potential with high voltage applied to the single-orifice extractor gate.

5.1 First-Generation Prototype Design Objectives

While the zeroth-generation prototype was successful in transporting, charging, and extracting micro-particles, it did so with a solenoid-driven slide and external vibration source that would not be present in the envisioned flat-panel NanoFET design. As an intermediate step towards a NanoFET prototype capable of handling nano-particles, a more refined micro-particle extractor was desired to validate a piezoelectric-based propellant feed system design, improve understanding of particle-sieve interactions, and demonstrate consistent emission of 1-10 μm particles. Developing proficiency in addressing these issues is desirable prior to testing with nano-particles. In addition, the new micro-particle extractor could be designed to permit future operation with nano-particles simply by replacing the existing micro-sieves with nano-sieves under development; this approach would permit earlier demonstration of nano-particle operations without the need for a time-intensive and costly MEMS development effort.

5.2 First-Generation Prototype Design Features

Figure 5.2 shows the design of the first-generation micro-particle extractor prototype. This configuration was designed to be vacuum compatible, so materials were generally chosen to have a total mass loss less than 1% in vacuum. Vented screws and vent paths were implemented to promote rapid leaking of trapped air pockets when the system is placed under vacuum; this approach reduced the likelihood of having virtual leaks that may increase the risk of Paschen breakdown between the high-voltage electrodes.

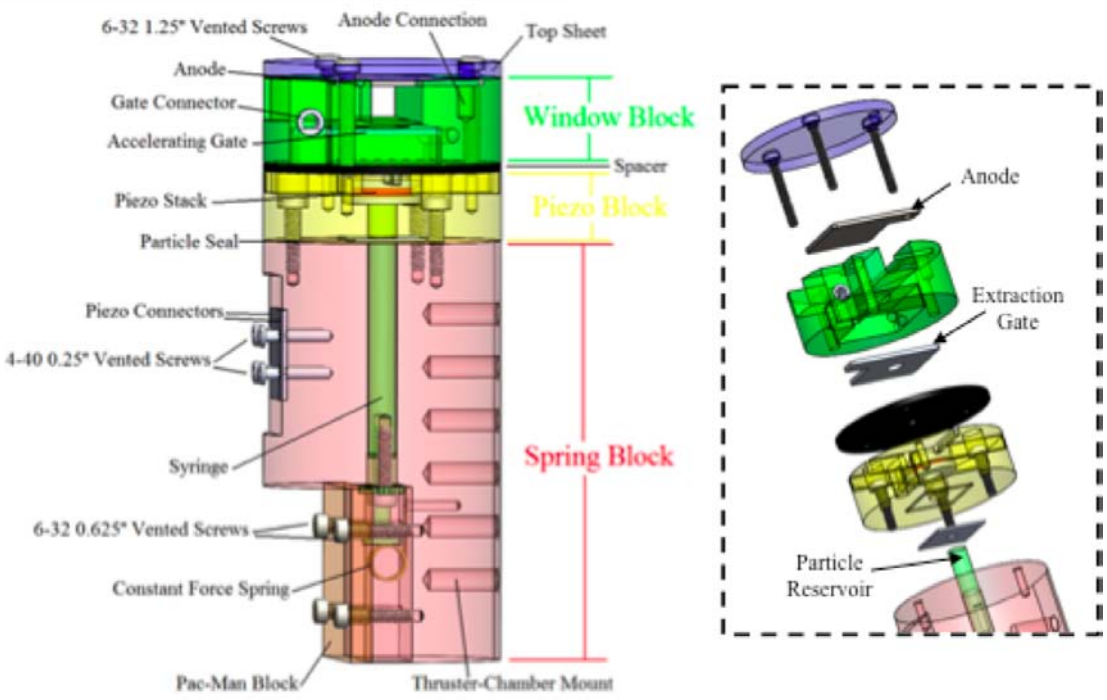

Figure 5.2: First-generation micro-particle extractor design. Blocks are modular.

5.2.1 Spring Block

The polycarbonate spring block provides the mounting interface to the vacuum chamber and houses the particle reservoir. As with the zeroth-generation prototype, a modified medical syringe serves as the particle reservoir, since the original, tapered tip

tended to promote particle binding. The plunger end in direct contact with the particles has a rubber seal to prevent particles from escaping, and the other plunger end is pressed upon by a constant-force spring. Instead of a linear actuator to generate the backpressure as in the zeroth-generation prototype, the constant-force spring provides a passive (i.e., no power draw) and more reliable approach. Following each test firing, the particle reservoir is replaced with another loaded syringe. The spring block also houses the strain-relief interface between the piezoelectric lead wires and drive cables from the vacuum chamber's electrical feedthrough.

5.2.2 Window Block

Also made from polycarbonate, the window block houses the high-voltage electrodes in the extractor prototype. The stainless steel, single-orifice extractor gate is placed 1 cm away from the charging sieve. A removable collection anode can be placed to monitor particle deposition following extraction; if left in place, the anode is biased to the same electric potential as the extractor gate so that a field-free region exists between them. Openings in the window block permit laser access to the emitted particles for laser velocimetry.

5.2.3 Piezo Block

The polycarbonate piezo block houses the charging sieve and a piezoelectric assembly, which together comprises the particle feed system for the micro-particle extractor prototype. An electroformed, nickel sieve (Figure 5.3 (*right*)) is held at common ground potential and used to charge the particle propellant in the presence of the extractor gate. The sieve is mounted to the piezoelectric assembly, composed of a Noliac CMAR04 ring piezoelectric sandwiched between alumina washers as stiff mounting

substrates, using vacuum-rated epoxy (Scotch-Weld 1838 B/A green epoxy and Kurt J. Lesker silver conductive epoxy KL-325K). A particle seal made from Buna-N rubber is sandwiched between the piezo and spring blocks.

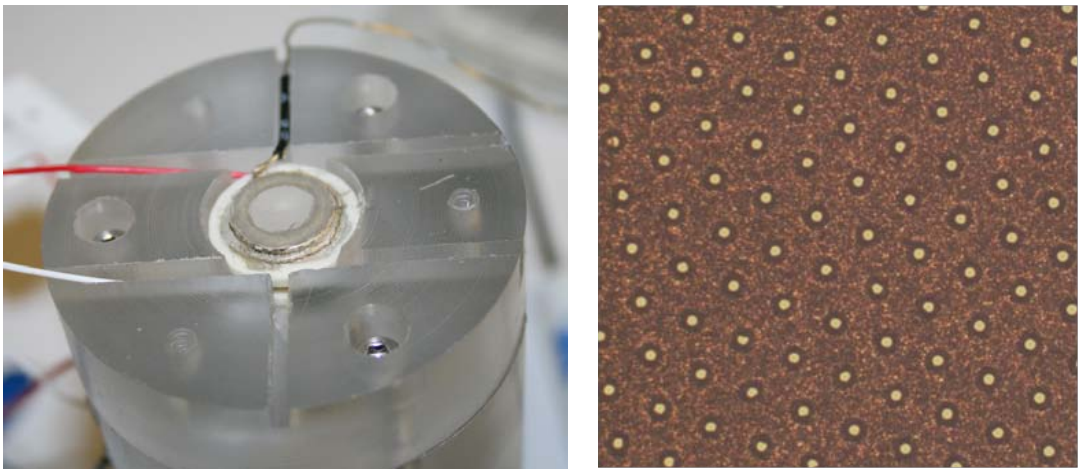

Figure 5.3: Piezoelectric-driven particle feed system. (*Left*) Piezoelectric assembly and charging sieve mounted over particle reservoir. (*Right*) Electroformed, nickel sieve with 10-µm orifices and 50-µm pitch.

5.3 Functional Characterization

Table 5.1 shows the baseline operating parameters for the micro-particle extractor prototype [69]. A gate aspect ratio less than unity was used to promote optimal particle charging. 1-10 µm, silver-coated, soda lime glass particles from Mo-Sci Corporation were used as propellant compatible with the 10-µm sieve orifices. With a sieve pitch of 50 µm, the nominal, normalized proximal distance for the particles is $\zeta_{R,d} \geq 5$ to reduce proximal-particle effects. The near-mesh size nature of the particles, intended to help promote extraction of individual particles, has been observed by other researchers to generate noticeable sieve blinding [70,71]. Standish, however, observed that the sieve blinding effect was reduced in the presence of oversized particles; sieving efficiency is improved due to the oversized particles pushing through embedded near-mesh particles

and opening up orifices for other particles [72]. This strategy was implemented on the micro-particle extractor prototype by including a ~50% monolayer of 53-μm, silver-coated, soda lime glass particles from Mo-Sci Corporation at the top of the particle reservoir (Figure 5.4 (*bottom right*)).

Parameter	Value
Operating voltage	15 kV
Charging electric field	1.5 V/μm
Gate aspect ratio	0.635
Piezoelectric frequency	15 kHz
Piezoelectric displacement	1.4 μm
Backpressure	2.9 N
Charging sieve orifice	10 μm
Charging sieve pitch	50 μm
Propellant size	1-10 μm
Propellant mass density	2.5 g/cm^3
Oversized particle size	53 μm

Table 5.1: Baseline operational parameters. Throttling is accomplished by varying the operating voltage and the piezoelectric actuation.

Figure 5.4 shows the micro-particle extractor prototype in operation. Testing was performed in a 12-in, spherical vacuum chamber at the Plasmadynamics and Electric Propulsion Laboratory. With a turbomolecular pump and dry diaphragm backing pump, the chamber was evacuated to < 10^{-5} Torr and kept there for at least six hours prior to each test. A 150-mW, 500-nm wavelength laser was used to illuminate the particle

emission for laser velocimetry using a FASTCAM-X 1024 PCI high-speed imaging system at 90° to the incident laser beam; the shutter speed was set as the reciprocal of the frame rate. High voltage was supplied with a Glassman EH30N3 negative-polarity, high-voltage power supply, and the piezoelectric was driven by input signals from an Agilent 33220A arbitrary waveform generator amplified via a Kepco BOP 100-2M bipolar operational power supply.

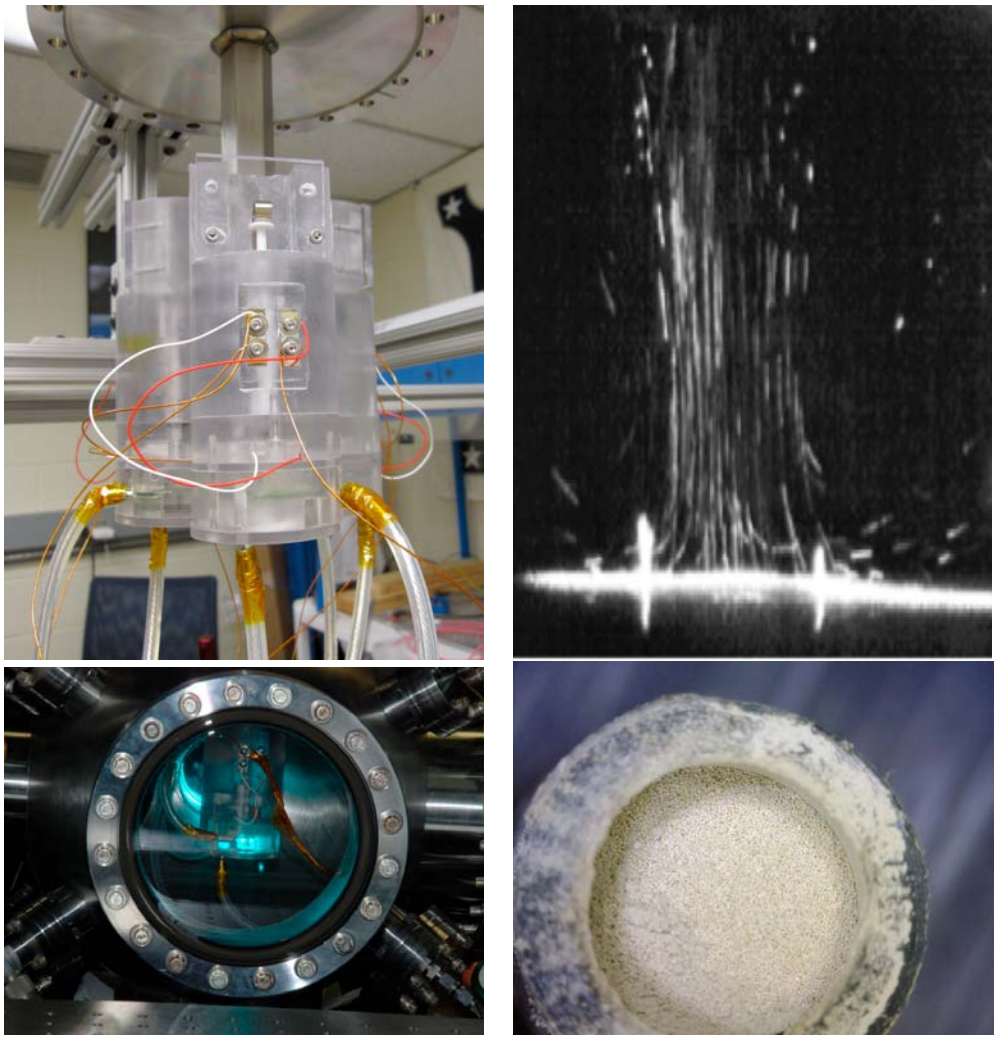

Figure 5.4: Micro-particle extractor prototype in operation. (*Top left*) Three prototype extractors, orientated downwards, being prepared for integration into vacuum chamber. (*Bottom left*) Laser illumination of window block. (*Top right*) Representative emission illuminated by laser with particles impacting and depositing on collection anode. (*Bottom right*) Top view of particle reservoir with layer of oversized particles.

5.4 Test Results

Figure 5.5 shows representative behavior of the piezoelectric during baseline operations.

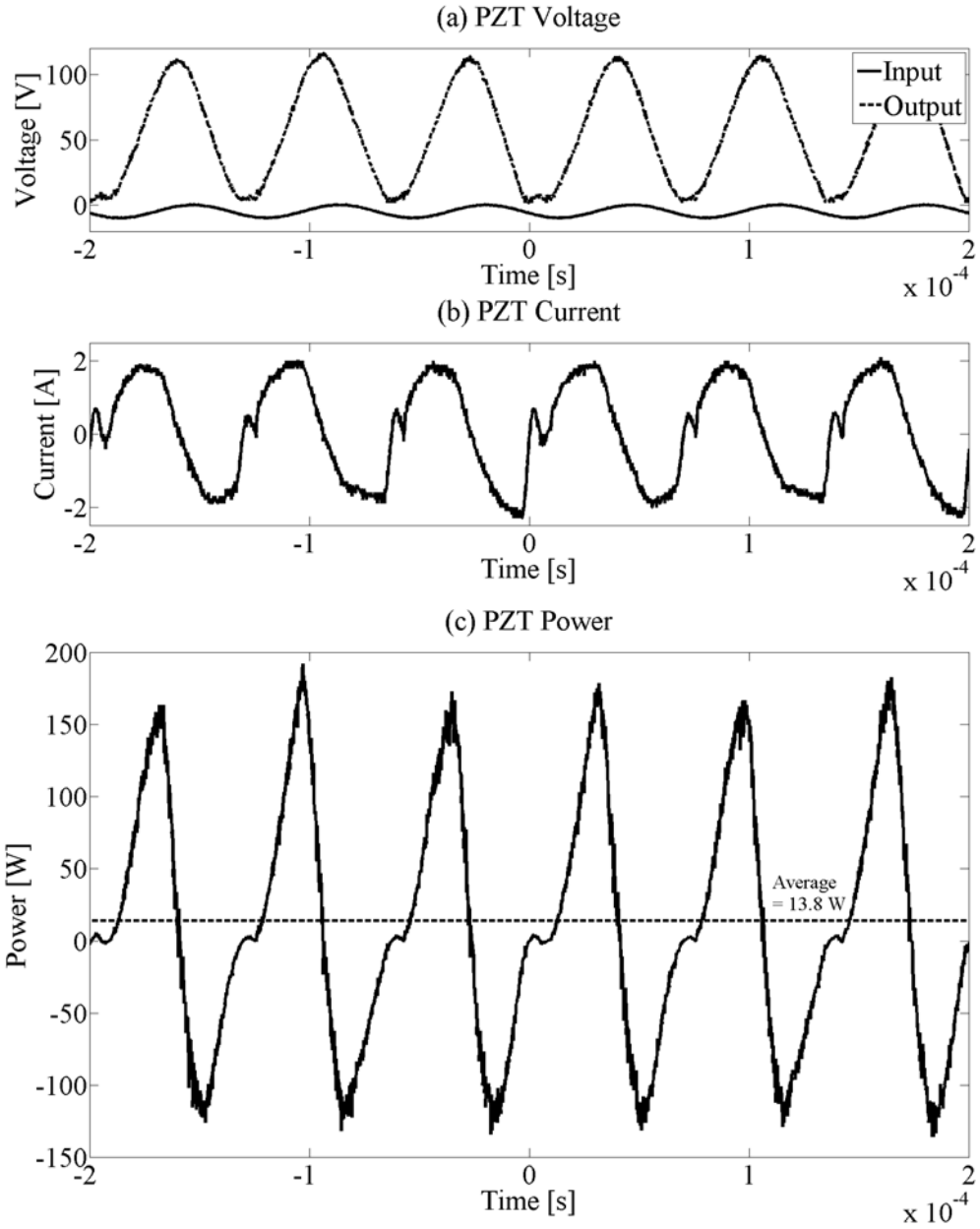

Figure 5.5: Piezoelectric behavior at 15 kHz in micro-particle extractor prototype. (*a*) Voltage bias prior to (i.e., input) and following (i.e., output) amplification by bipolar operational power supply. (*b*) Current draw. (*c*) Instantaneous and average power draw.

A phase shift of 44° was present between the input (i.e., pre-amplified) and output (i.e., post-amplified) piezoelectric voltage signals due to bandwidth limitations on the bipolar operational power supply. During each oscillation cycle, higher frequency modes appeared when the free end of the piezoelectric returned to its null-displacement state. The current draw agreed well with Equation (3.10) and changed polarity as the piezoelectric alternatively stored and released energy. Under the baseline test conditions, the piezoelectric load was mostly reactive, with the voltage and current signals having a phase shift of 66°. The average real power draw (i.e., heat dissipation in the piezoelectric) during baseline testing was thus 13.8 W, which corresponds to a power density of 12.2 W/cm^2. This power density is at least an order of magnitude greater than those of piezoelectric films in Reference 68, thus indicating the desirability of utilizing thin-film piezoelectrics in future prototypes.

With a 150-mW laser, only ~1 kfps frame rates could be achieved with the high-speed imaging system; higher frame rates resulted in insufficient image intensity for analysis. The lower than ideal frame rates (i.e., ~10 kfps) resulted in substantial streaking in the particle images (Figure 5.4 (*top right*)) that made image auto-correlation algorithms difficult to implement. Since each pixel in the high-speed images corresponds to ~20 μm and each particle streak in an image was made during the camera's shutter time, an estimate of the particle velocities can be made by counting the number of pixels along the length of each streak. Doing so yielded a mean speed measurement during baseline operations of ~1.5 m/s. While this speed is greater than the effect due to gravity (i.e., 0.6 m/s), it is an order of magnitude less than expectations. Assuming a near-unity net charging factor, which is not unreasonable (apart from sieve obscurement and

proximal particle effects) for the baseline configuration (i.e., $d \ll H$ and $D/H = 0.635$), a 5- μm and 10-μm propellant particle would be expected to achieve 18 m/s and 13 m/s exhaust speeds, respectively, using Equation (4.9).

Figure 5.6 shows post-test images taken with a scanning electron microscope. The poly-disperse nature of the propellant is readily apparent in these images, and clusters of these particles are present at each sieve orifice. Consequently, the assumption of a near-unity net charging factor does not hold. From Figure 2.14, the net charging factor in a gated diode configuration for a mono-disperse particle set is ~0.2 for $R/d = 1$.

Figure 5.6 (*bottom*) shows the collection anode's surface following a brief extraction period. No ordered array arrangement of particle deposition is seen, indicating the presence of sieve blinding or dispersion due to the piezoelectric acting on the charging sieve. While some of the particles appear to have been extracted individually, many others are present in the form of clusters. Either subsequent particles were deposited in close proximity to the ones that came before, or the clusters seen at the sieve in Figure 5.6 (*top*) were extracted together. If the latter case, then the corresponding specific charge and thus the exhaust velocity of the cluster would be lower than if the particles were extracted individually. Furthermore, since the scattering cross-section varies as the quadratic of the particle size for micro-particles 1-10 μm in diameter [73], particle clusters would be more visible due to higher image intensities than the individual particles (which may even be below the detection threshold), thus skewing the velocity measurements towards lower values. Plans to address these shortcomings in future tests are in works.

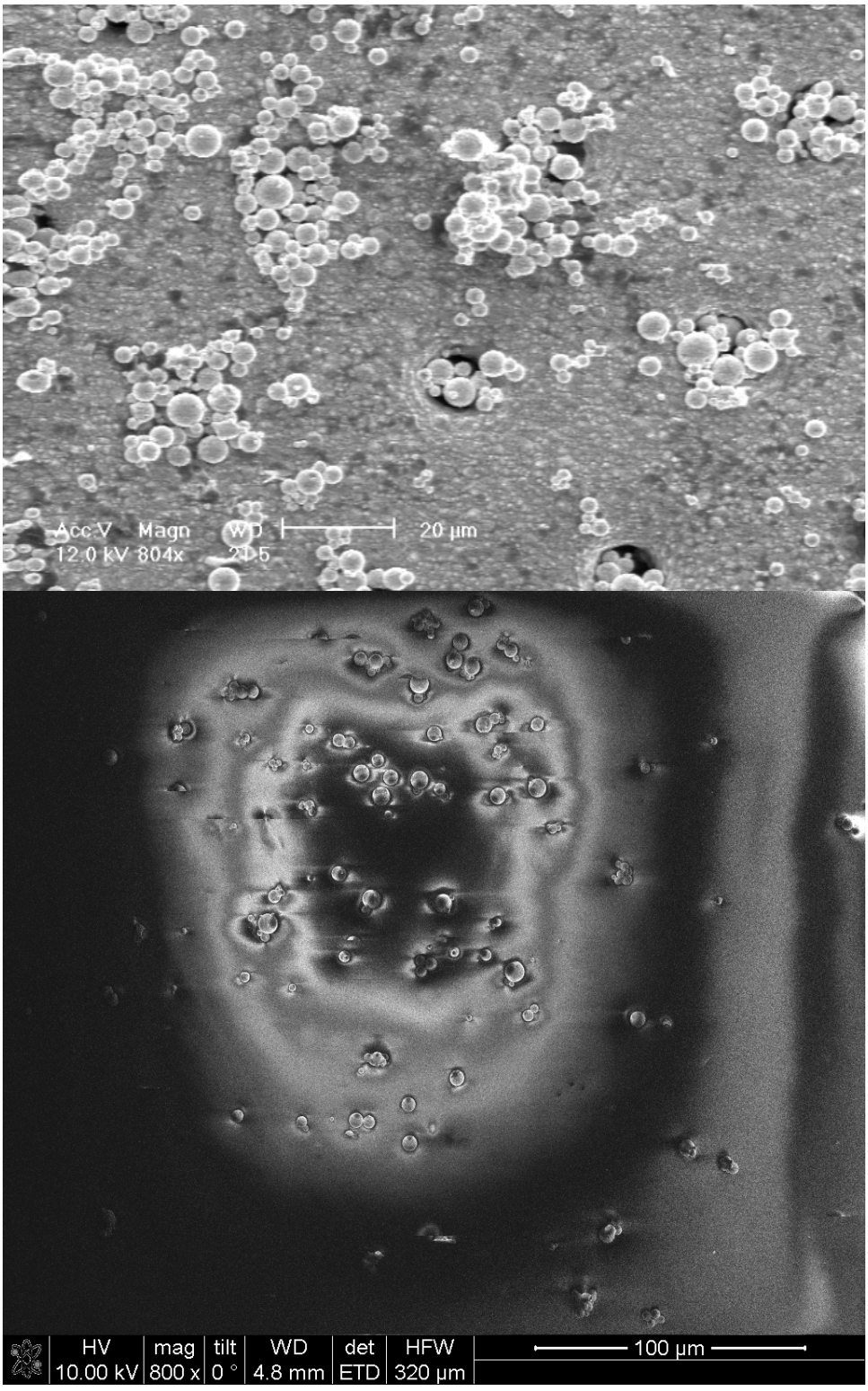

Figure 5.6: Post-test scanning electron microscopy characterization. (*Top*) Top side of charging sieve. (*Bottom*) Pulsed deposition on glass collection anode. Ripples are image artifacts from the glass substrate charging under the electron beam.

5.5 Implications for NanoFET

While the feasibility of using a piezoelectric-driven feed system was demonstrated with the first-generation micro-particle extractor prototype, the lower than expected velocity measurements suggest the need for good control of propellant particle size distributions. Having mono-disperse particles just smaller than the sieve's orifice size is expected to limit formation of particle clusters and the attendant reduction in specific charge. However, these near-mesh particle sizes have increased sieve blinding, which while not permanent due to the presence of oversized particles, would reduce the average mass flow rate; this phenomenon could be addressed to lower the thrust and power density projections in Chapter 4 by incorporating a sieving efficiency factor. The effect of oversized particles on local warping and mechanical wear of the charging sieve are additional issues that must be considered from a performance and lifetime perspective. Future prototyping work, especially as features are scaled down in size to the MEMS scale, should make use of thin-film piezoelectrics that have lower heat dissipation to improve thrust efficiency.

Chapter 6

Liquid-NanoFET Surface Instabilities

A liquid-based NanoFET configuration (Figure 6.1), while reducing inter-particle cohesion issues due to having the particle propellant in a liquid suspension, has a number of liquid-associated concerns that makes it less appealing for space propulsion. To do so, the liquid-based system would need to maintain a stable liquid-vacuum interface during thruster operations as well as minimize particle wetting and the resultant fluid loss during particle extraction; viscous drag from the liquid also decreases the achievable current density due to space charge effects [74]. In addition, having a recirculating, microfluidic feed system increases overall system complexity.

Liquid candidates must not react with the particulate propellant and be of low vapor pressure to avoid excessive evaporative loss to the space environment. The liquid should also have low electrical conductivity and viscosity to reduce particle charge loss and viscous drag losses, respectively. Potential terrestrial uses such as filtration and environmental remediation applications are more promising for the liquid-NanoFET, since they generally have less demanding environmental and operational requirements as compared to space propulsion uses.

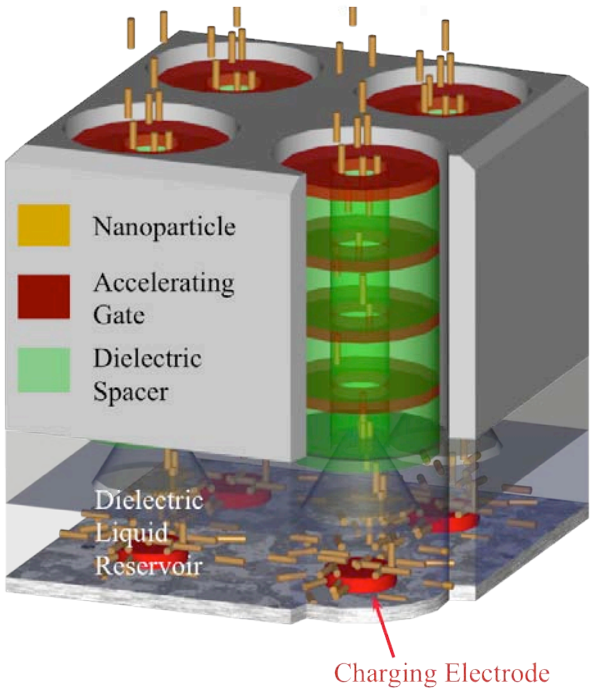

Figure 6.1: Concept view of liquid-NanoFET configuration. Four liquid-NanoFET emitters in operation.

6.1 Electrohydrodynamic Instabilities

As with the NanoFET configuration using dry particle propellant, the specific charge attainable by the liquid-NanoFET configuration is limited by the maximum allowable charging electric field. Whereas NanoFET is limited by field strength limits associated with electron field emission or ion field evaporation as well as electrical breakdown of insulator materials, the liquid-NanoFET has two other limiting factors. The first is the liquid's electrical breakdown strength; the second, possibly lower, limit is the threshold for liquid surface instabilities.

When a liquid surface is subjected to sufficiently high electric fields, the resulting electric pressure on the charged liquid surface can overcome gravity and surface tension. The result is the formation of Taylor cones on the liquid surface [75] that may result in the ejection of liquid droplets as in an electrospray thruster. Such features are

undesirable for propulsion applications because they lead to fluid loss in the system as well as reduced thrust precision due to droplet emission in addition to particle extraction.

Following Tonks's approach [76], as diagramed in Figure 6.2, a balance of electrostatic, hydrostatic, and surface tension forces at the liquid surface results in the liquid surface first becoming unstable at the instability threshold $E_{\min}$, given as

$$E_{\min} = \left(\frac{4\gamma\rho_l g}{\varepsilon_0^2} \right)^{\frac{1}{4}}, \tag{6.1}$$

where γ is the surface tension coefficient, ρ_l is the liquid mass density, g is the gravitational acceleration, and ε_0 is the permittivity of free space. If the derivation is redone by neglecting gravitational forces for a system of characteristic size L in which the Bond number Bo, defined as

$$Bo \equiv \frac{\rho_l g L^2}{\gamma}, \tag{6.2}$$

is much smaller than the critical value Bo^*, then the threshold for liquid surface instability becomes

$$E_{\min} = \left(\frac{8\gamma}{\varepsilon_0 \lambda} \right)^{\frac{1}{2}}, \tag{6.3}$$

where $\lambda/2$ is defined in Figure 6.2 as the effective perturbation hump diameter. The instability threshold, which is independent of a spatial scale when gravitational effects are important, varies with the inverse square root of the system's characteristic length when gravitational effects are negligible.

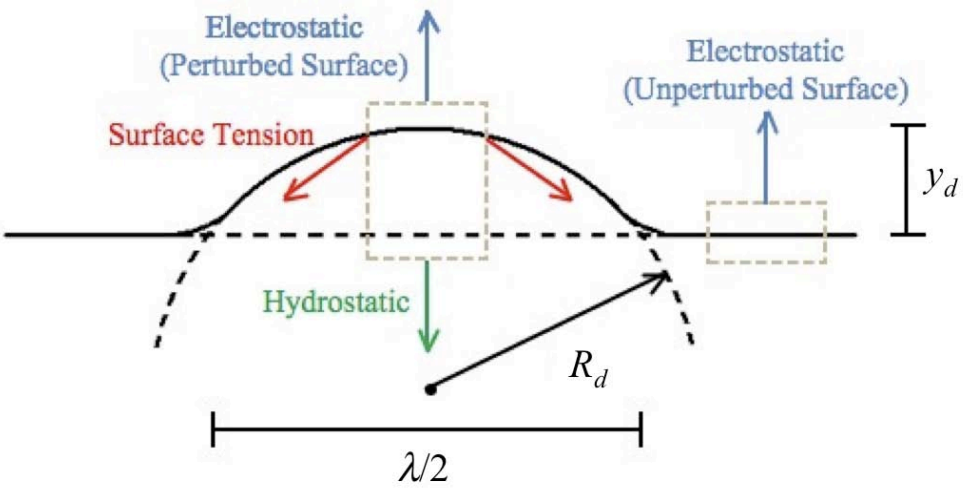

Figure 6.2: Free-body diagram for Tonks's derivation of the liquid surface instability threshold. The free liquid surface is assumed to be uniformly charged, and the incipient distortion (i.e., $y_d \ll \lambda/2$) on the liquid surface is assumed to be a hemispherical boss of radius R_d.

6.2 Investigating Electrohydrodynamic Behavior in Microgravity

To investigate the impact of liquid-NanoFET operating in the low *Bo* regime, which is likely due to small emitter feature sizes and possible use in space environments, a series of microgravity flight experiments were conducted in cooperation with the University of Michigan Student Space Systems Fabrication Laboratory, a student-led organization dedicated to providing university students with practical space systems design-build-test-fly experiences [77], and NASA's Reduced Gravity Student Flight Opportunities Program [78]. The experimental objectives were to determine, in microgravity, the electric field thresholds for liquid surface instabilities and to observe the liquid-wall interactions of the liquid reservoirs [79].

6.2.1 Test Cell Design

Polycarbonate test cells were used to contain the test liquid in flight. A dual-channel configuration for the test cells housed independent test channels, thereby permitting one channel to be tested while monitoring the adjacent passive channel for

microgravity effects. Following a previous microgravity experiment [80], knife-edge orifices were fabricated from polycarbonate plates to pin the liquid surface as passive valves and prevent the test liquid from climbing the channel walls due to capillary effects. The knife-edge orifice functions due to the principle that a pressure barrier develops when the cross-section of a channel abruptly enlarges; for the knife-edge geometry shown in Figure 6.3, a passive valve is formed if the knife-edge expansion angle meets the criterion $\beta_k > 90° - \theta_c$ [81]. Knife-edges used in flight all have an expansion angle of $\beta_k = 90°$.

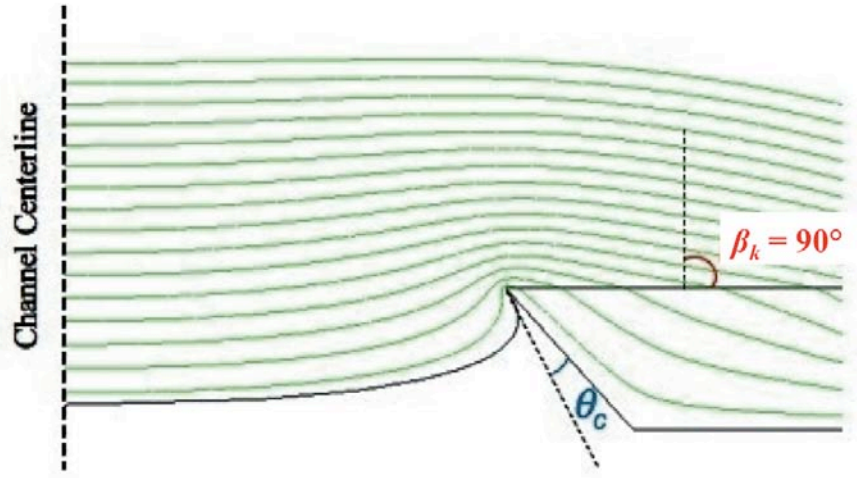

Figure 6.3: Charged liquid surface pinned at the knife-edge. Equipotential lines indicate an intensification of the applied electric field at the knife-edge. $\beta_k = 90°$ in the figure.

As shown in Figure 6.4, each test cell channel housed a stainless steel electrode flush with the bottom of the channel. An electrode was biased to high voltage to charge the liquid, and an electric field was generated between the charged liquid surface and the grounded glass anode coated with indium tin oxide (ITO). The test cells were sealed against leaks by rubber Buna-N gaskets at the transparent front and back faceplates.

Soybean oil (0.91 specific gravity, 3.2 ± 0.3 relative permittivity, 2 mS/m electrical conductivity, and 30.1 mN/m surface tension [82,83]) was used for the liquid instability study due to its fast characteristic charging time (i.e., τ_c = 14 ns per Equation (2.6)) that permitted the liquid surface to become fully charged during each microgravity test period; the equilibrium contact angle θ_c = 15.9° of soybean oil to polycarbonate was measured via confocal laser scanning microscopy.

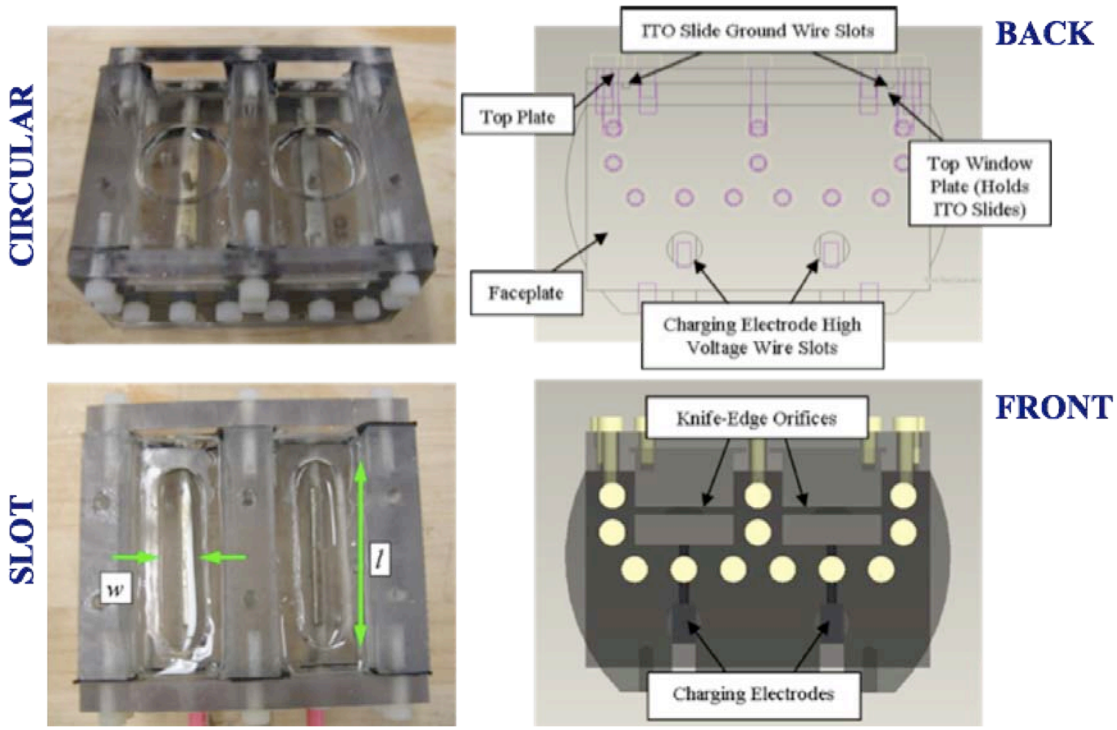

Figure 6.4: Dual-channel test cell design for observing liquid surface instabilities in microgravity. The test cells used in flight included both circular (*top left*) and slot (*bottom left*) knife-edge orifices. The ends of the slots are semicircles. (*Top right*) The back of a test cell houses electrical connections to the high-voltage charging electrodes and the grounded ITO anode. (*Bottom right*) Liquid is filled to just below the knife-edge, leaving an air gap from the knife-edge to the anode.

6.2.2 Experiment Setup

The experiment layout onboard the NASA C-9B aircraft is shown in Figure 6.5.

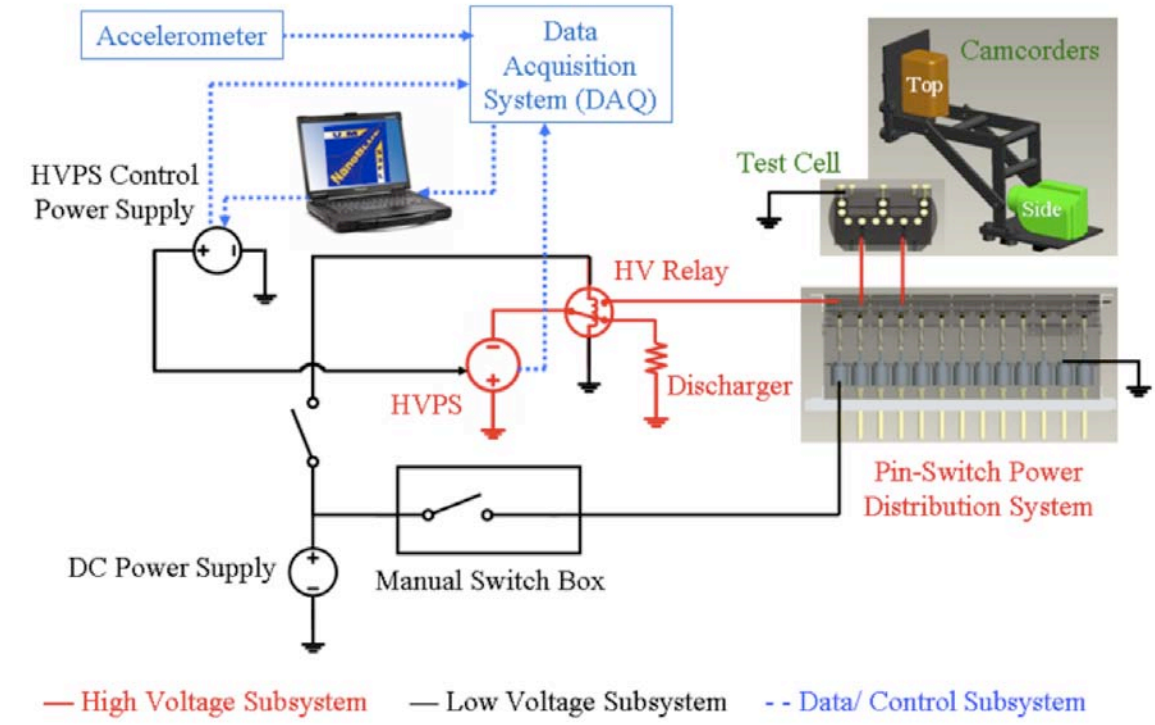

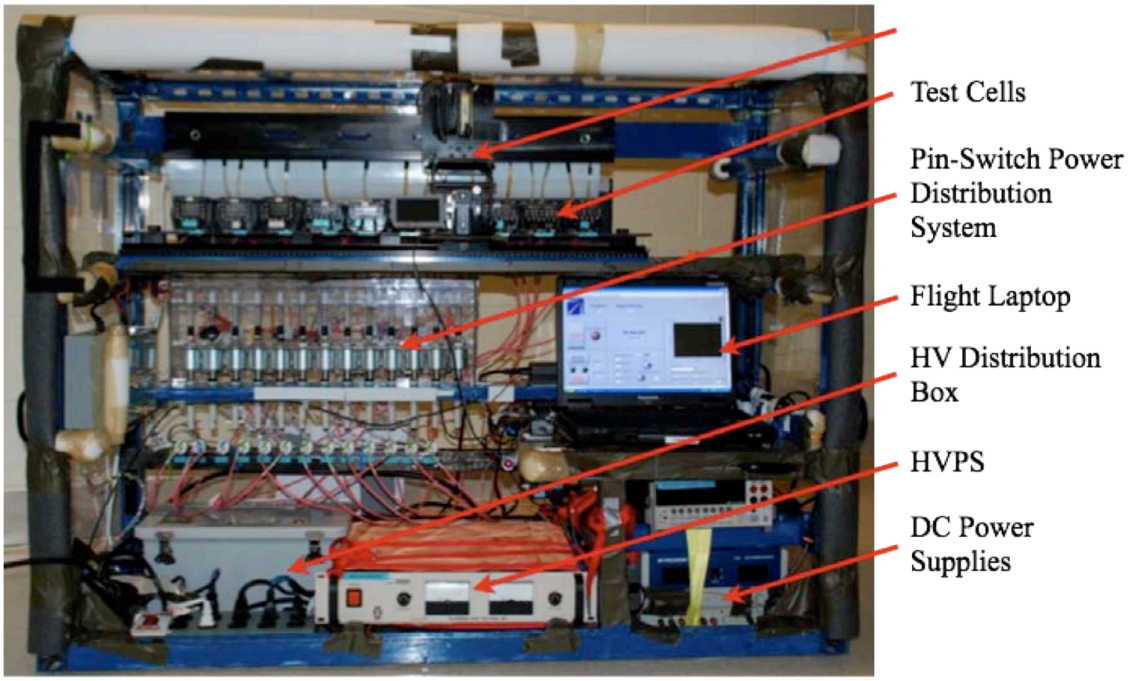

Figure 6.5: Microgravity experimental setup. Multiple test cells were connected to the pin-switch power distribution system. Power and flight accelerometer readings were provided by the C-9B aircraft. (*Top*) Block diagram. (*Bottom*) Setup integrated onboard aircraft.

A Glassman EH30N3 negative-polarity, high-voltage power supply (HVPS) was commanded remotely via a LabVIEW-controlled Keithley 2400 sourcemeter. A Gigavac high-voltage single-pole/double-throw relay connected the pin-switch power distribution system to either the HVPS (i.e., to bias the test cells) or to a high-power resistor (i.e., to discharge the test cells in between tests). The pin-switch power distribution system, when activated via manual switches, permitted specific test channels to be electrically biased. The experiment's aluminum unistrut frame served as the electrical ground through direct bolting to the aircraft cabin's floor.

Two camcorders were mounted on a sliding track to view the test cells during flight. A Sony DCR-DVD505 Handycam provided a front view of the test cells at 60 fps while a Sony DCR-HC26 Handycam provided a top view of the test cells at 30 fps. Current-voltage data was obtained with a Keithley KUSB-3102 data acquisition module connected to a Panasonic Toughbook 52 semi-rugged laptop running the LabVIEW test code. Three-axis accelerometer readings from the aircraft were recorded, and both the aircraft cabin temperature and relative humidity were monitored in flight.

6.2.3 Flight Operations

Sets of parabolic flights were conducted with each parabola providing approximately 20 s of microgravity test time. On average, the aircraft cabin had a temperature of 16 ± 2 °C with a relative humidity of 15 ± 3% during the flights. During microgravity periods, the HVPS increased the voltage bias to the test cells by 1-kV steps every second, as seen in Figure 6.6. This voltage profile was implemented so that each test voltage set point may be held for at least the duration of the characteristic Taylor cone formation time t_T, given as

$$t_T = \pi\sqrt{27}\,\frac{\gamma}{E^3}\left(\frac{\rho_l}{\varepsilon_0^3}\right)^{\frac{1}{2}}, \tag{6.4}$$

where E is the applied electric field at the liquid surface [84]. For soybean oil under the test conditions, the characteristic Taylor cone formation times are less than 0.3 s, thus justifying the applied voltage profile. A single test channel was tested during each microgravity period, which was followed by about 50 s of up to 1.8-*g* exposure. No tests were conducted during these high-gravity periods.

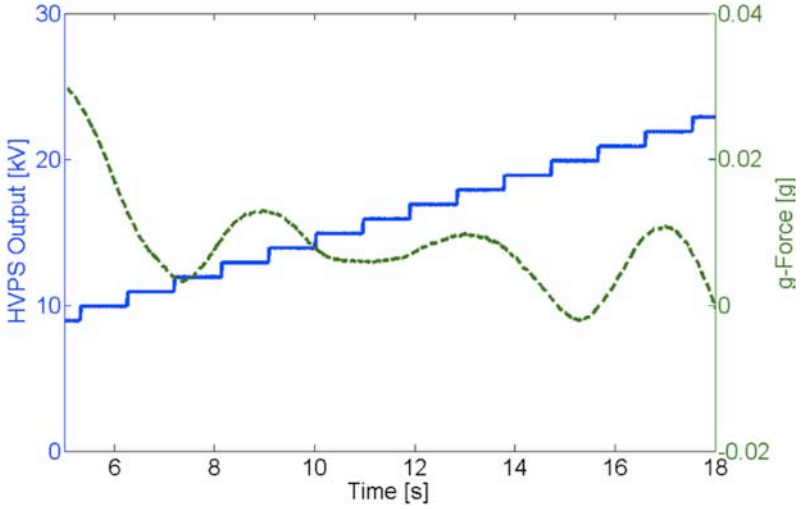

Figure 6.6: Representative microgravity test conditions. Time elapsed since the start of the microgravity test period is shown along with in-flight sensor data.

6.3 Microgravity Test Results

Prior to flight, each test cell was filled such that the liquid meniscus remained below the top of the knife-edge. In microgravity, the meniscus level decreased from its preflight height, suggesting liquid climbing of the knife-edge shelf walls. However, no liquid spillage out of the passive valves prior to Taylor cone formation was apparent with the application of electric fields during testing.

Figure 6.7 shows a typical Taylor cone observed during flight, with cone formation occurring at the knife-edge rather than within the orifice. As shown in Figure 6.3, the liquid must maintain its equilibrium contact angle with the wall while pinned at the knife-edge, resulting in a liquid surface that is concave upwards. Consequently, the electric field is intensified at the knife-edge's triple junction, where Taylor cones would be expected to form first. Some liquid spilled from the larger knife-edge orifices during aircraft takeoff; however, subsequent Taylor cone formation occurred away from these spill sites, suggesting that the spills did not impact test results.

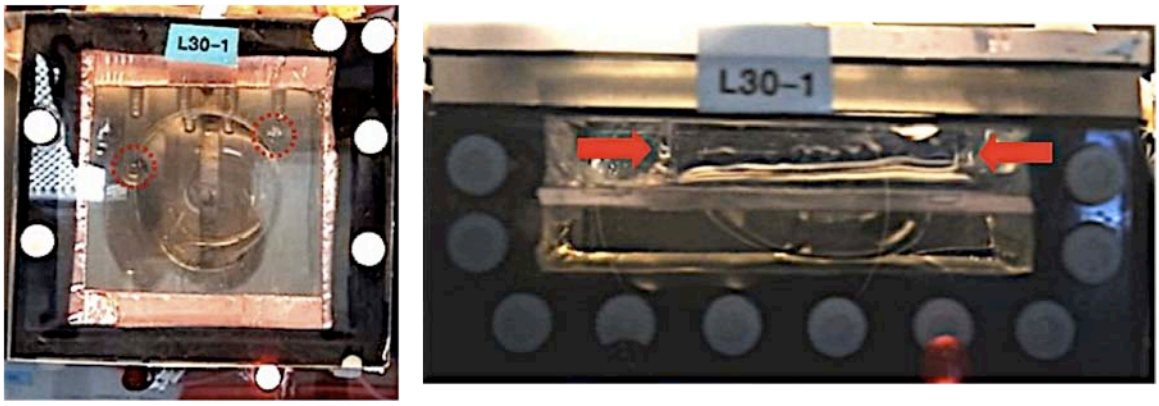

Figure 6.7: Soybean oil Taylor cone formation in microgravity. (*Left*) Two cones (circled) are visible for the 30-mm diameter knife-edge orifice. (*Right*) Front view of the same test cell shows the Taylor cones (arrows) along with associated liquid escape from the passive valve, resulting in a dip in the liquid meniscus.

With the charged liquid pinned at the knife-edge in microgravity, the effective gap distance may be assumed to be the separation of the ITO anode from the top of the knife-edge. On the ground, the effective gap distance is the nominal fill height (i.e., midway between the bottom and top of the knife-edge shelf) corrected for the capillary climb height h_c [85], given as

$$h_c = \frac{4\gamma \cos\theta_c}{\rho_l g D}, \tag{6.5}$$

where D is the orifice diameter.

Figure 6.8 shows that in microgravity, liquid surface instabilities become excitable at lower electric fields as the orifice diameter increases. The microgravity test flight data are in good agreement with

$$E_{\min} = \left(\frac{8n\gamma}{\varepsilon_0 D} \right)^{\frac{1}{2}}, \tag{6.6}$$

where $n = 3$. Comparison with Equation (6.3) suggests that the orifice diameter is six times larger than the effective perturbation hump diameter. Assuming that the perturbation may be treated as a standing wave across the orifice with the effective hump diameter being a half wavelength, Equation (6.6) indicates that the orifice diameter is three times larger than the perturbation wavelength.

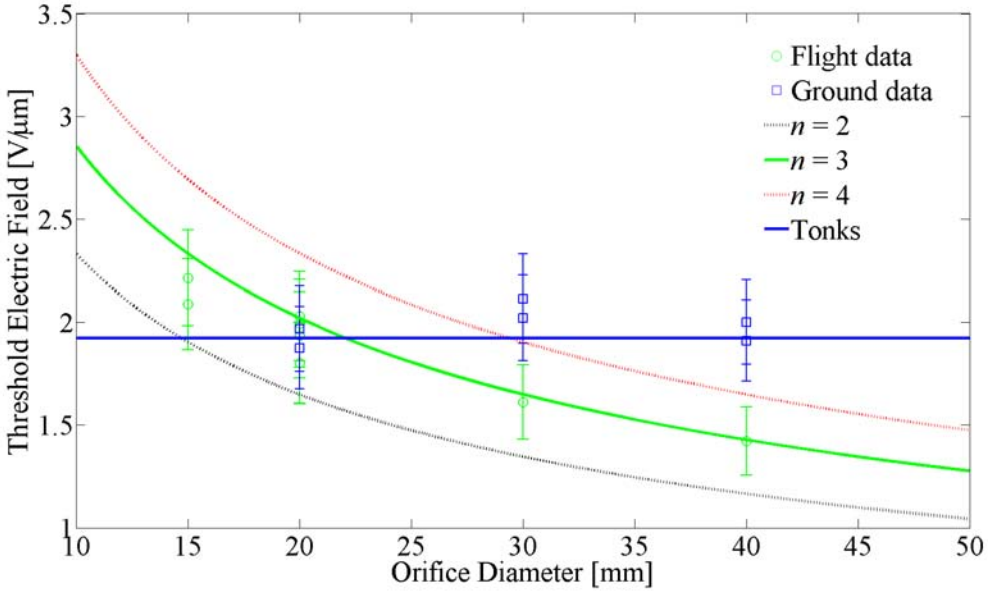

Figure 6.8: Onset of liquid surface instabilities in soybean oil for circular knife-edge orifices. The electric field is defined as the ratio of the test cell bias voltage to the effective gap distance, with $n = 3$ of Equation (6.6) providing the best fit to the flight data.

Ground test results, at 23 ± 1 °C with a relative humidity of 55 ± 4%, obtained using the same in-flight voltage profile are in good agreement with Equation (6.1), which, when equated with Equation (6.6) (n = 3), gives the critical orifice diameter D^* as

$$D^* = \left(\frac{144\gamma}{\rho_l g} \right)^{\frac{1}{2}}. \tag{6.7}$$

Comparison with Equation (6.2) suggest that when using the orifice diameter as the characteristic length, systems with Bo « 144 are dominated by surface tension effects, and Equation (6.6) (n = 3) may be used to determine the electric field threshold for liquid surface instability. Otherwise, gravitational effects play an important role in the system, and Equation (6.1) should be used. This critical Bond number (i.e., Bo^* = 144) for the largest test orifices corresponds to 0.3 g, which is significantly larger than the onboard g-forces shown in Figure 6.6 and confirms that the C-9B flights provided a test environment sufficient to examine systems dominated by surface tension effects. For soybean oil on the ground, the critical orifice diameter is about 22 mm; as the orifice size decreases from the critical value, the system is expected to be increasingly governed by surface tension effects and Equation (6.6). However, testing of smaller orifices was limited by electrical breakdown in the test cell air gap, especially during ground tests due to the higher humidity levels.

As shown in Figure 6.4, slot knife-edged orifices can be specified by two dimensions, the length l and width w. Figure 6.9 shows the test results for slots with a length of 30 mm. The flight data, with a modest range of slot aspect ratios tested, suggest that in the low Bond number regime, Equation (6.6) may be used for slot orifices by setting $D = l$. This approach is equivalent to stating that the largest orifice dimension

determines the characteristic length. As with the circular orifices, Taylor cones formed at the knife-edges rather than within the orifice.

On the ground, test data display good agreement with Equation (6.1). Use of the smaller slot width dimensions as the characteristic length still results in Bond numbers on the order of Bo^*. Therefore even for the larger slot aspect ratios, gravitational effects remained important in the system for the ground tests, thus justifying the fit to Equation (6.1).

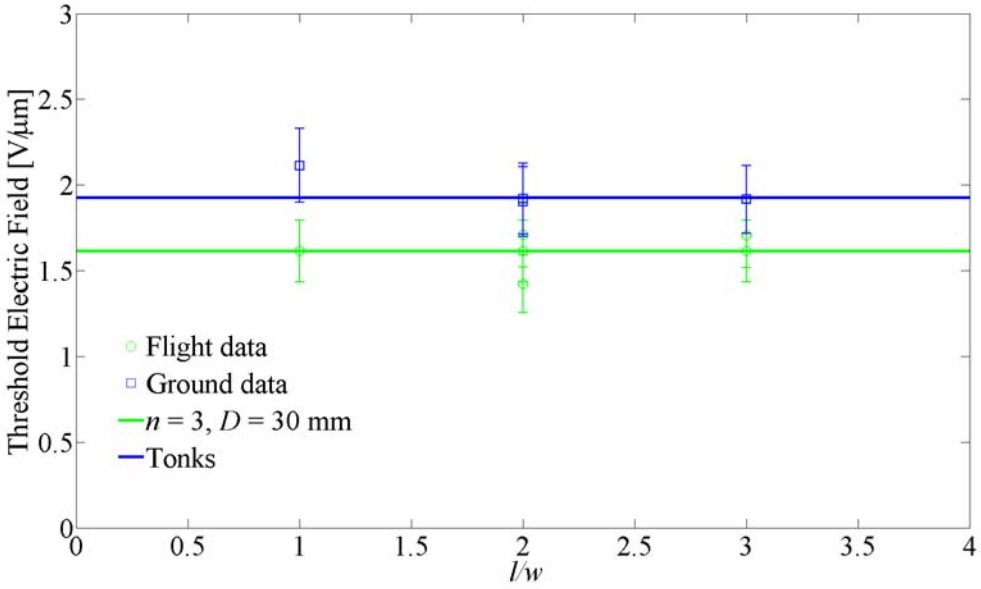

Figure 6.9: Behavior of slot knife-edge orifices (l = 30 mm) in microgravity for soybean oil. l/w = 1 refers to circular orifices.

6.4 Implications for NanoFET

For low Bo regimes (i.e., small feature sizes or operation in space), the electric field threshold for liquid surface instability is increased for smaller channels (i.e., $E_{min} \propto D^{-1/2}$). Higher particle charging electric fields may thus be possible for knife-edge channels at the MEMS scale, resulting in a larger range of specific charge and extraction performance, as long as the applied electric fields also do not exceed the electrical

breakdown limits of the charging stage and liquid. While slot orifice geometries may be easier to microfabricate than large numbers of circular orifices, the trade-off must be evaluated between manufacturing ease and the reduction in the maximum allowable charging electric field relative to an array of circular orifices.

Chapter 7

Summary and Future Work

The previous pages provided a mapping of the design space for NanoFET, an electrostatic propulsion technology that may be well suited for micropropulsion applications due to its operational flexibility (i.e., wide throttleability and variable specific impulse range), high efficiencies, precise thrust control, flat-panel scalability, and compact form factor. Analytical and numerical modeling results, coupled with proof-of-concept and prototype test data, are promising with regard to NanoFET's feasibility and encouraging for continued technology development.

7.1 Research Contributions

This dissertation includes the following new contributions:

- Design space mapping and top-level feasibility study of a novel micropropulsion concept using micro- and nano-particle propellant.
- Numerical model for the electrostatic charging of particles in diodes that accounts for geometric effects of the charging electrodes along with the presence of proximal particles.
- System implementation of piezoelectrics as a source of inertial forces to enable dry particle transport and controlled particle extraction (i.e., mass flow rate) in NanoFET.

- Refined NanoFET performance predictions, including models for thrust and efficiency.
- Micro-particle extractor prototype that demonstrated charging and extraction of 1-10 μm particles along with a piezoelectric-driven propellant feed system.
- Electrohydrodynamic instability suppression using knife-edge orifice geometries and validation via a microgravity flight experiment.

7.2 Recommendations for Future Work

The NanoFET technology is presently under development with efforts in place to continually raise its technology readiness level for an eventual in-flight technology demonstration. Based on the findings and lessons learned from this dissertation's research work, a number of recommendations can be made to help with the ongoing process.

The use of COMSOL as a multi-physics modeling tool permits for straightforward expansion of existing models to provide a more refined understanding of the underlying NanoFET physics. Conversion of the current particle charging models from axisymmetric to full 3D space would allow for higher fidelity representations of NanoFET's charging stage to be constructed, including the incorporation of multiple emitters, surface effects physics to model adhesion and cohesion, and inertial forces from piezoelectrics. Augmented COMSOL models may also be used to understand the effect of gate design configurations on the trajectories of extracted particles (i.e., optimize the gate stack design to minimize beam divergence) as well as strategies for NanoFET neutralization.

Of particular interest from an optimal charging as well as piezoelectric implementation standpoint is the particle feed process through the charging sieve. Charged particle liftoff experiments, including with piezoelectric actuation, should be performed for the entire particle size range of interest to NanoFET, starting with planar electrodes and progressing to charging sieves as nano-sieves are designed, fabricated, and improved. Doing so will refine anticipated NanoFET operating conditions (i.e., charging electric fields and piezoelectric actuations), assess the functionality of potential propellant candidates (e.g., coated particles), evaluate improved feed capability with oversized particles, and provide feedback to refine the nano-sieve design. For larger particles (i.e., ~1 μm diameter), use of a long-distance microscope right at the sieve surface would permit direct observation of the sieving process.

Refined performance characterization is needed to validate performance models and evaluate design improvements. The particle clusters encountered during testing with the first-generation micro-particle extractor prototype may be mitigated by using a more monodisperse particle propellant, and a rigorous investigation (i.e., optimal size, coverage, etc.) of the beneficial impact of oversized particles should be performed. Velocimetry experiments on the micro-particle extractor prototype should be conducted again with a higher power laser to reduce streaking effects on the high-speed images and thus facilitate using auto-correlation routines to determine exhaust velocity distributions as a function of operating voltage and charging electric field. For sub-micron particles, the use of laser velocimetry to resolve emission performance becomes challenging. A better diagnostic to use in the long term is an induction charge detector [86], which measures both the particle charge and time-of-flight. Use of this instrument would

experimentally validate the charging models in Chapter 2 and provide real-time measurements of specific charge states during thruster operations.

A micro-newton thrust stand would eventually be necessary to complete performance characterization of a NanoFET system. For the short term, thrust estimates may be obtained by incorporating a quartz crystal microbalance (QCM) and Faraday probe during extractor prototype testing. Since the QCM provides real-time measurements of the total mass of particles deposited on its surface while the Faraday probe provides the instantaneous emission current, combining the data from both diagnostics yields the specific charge. Using the mass flow rate obtained from the QCM and the emission beam power obtained from the Faraday probe, Equation (1.2) may be used to estimate the thrust level. The time-resolved measurements from this setup would reveal the extent that piezoelectric operations control particle flow rate. If the Faraday probe is constructed of phosphor-coated indium tin oxide (ITO), direct observation of beam size and divergence can also be made.

The design of the micro-particle extractor prototype described in Chapter 5, with its extractor gate at high voltage rather than at the common ground potential, makes probe-based diagnostics challenging (e.g., extracting small signals from a large DC offset). A next-generation micro-particle extractor prototype, incorporating the lessons learned from the first prototype, should be designed and fabricated to better understand integrated system issues prior to scaling down to use sub-micron particles. This second-generation prototype, besides addressing the shortcomings in the initial design (e.g., mechanical tolerancing of components, robustness of electrical connections, etc.) and

being designed for the flexibility to use nano-particles by accommodating a nano-sieve, should make the following three major design changes.

First, multiple gates should be implemented such that the particle charging and acceleration stages may be decoupled. This setup is more representative of the envisioned final NanoFET configuration and also permits greater flexibility during testing. The external gate should be kept at the common ground potential, which brings the prototype into closer alignment with flight thruster systems in which the exposed electrode is close to electrical (i.e., spacecraft) ground to minimize disturbances to the ambient plasma.

Second, having the external gate at the common ground potential results in the particle charging sieve and the particle reservoir being at high voltage with respect to the gate. Therefore, electrical insulation and high-voltage protection of the piezoelectric stack must be implemented. Third, the piezoelectric stack should be instrumented (i.e., strain gauges and thermocouples) to better evaluate propellant feed system performance as well as to enable feedback control of the throughput. A systematic investigation of resonant effects and different piezoelectric actuation schemes on particle feed rates should be done.

While the liquid-NanoFET configuration is less likely to be used for space propulsion applications, an understanding of the liquid surface behavior is still important for use in terrestrial applications. Issues that require more study include particle-induced instabilities and coating of particle surfaces as particles are extracted through the liquid. For applications in which throughput is important, further study of the reduction in achievable current density (Reference 74) due to viscous drag is recommended.

Bibliography

1 Fleeter, R., *The Logic of Microspace*, Microcosm: El Segundo, CA, 2000.

2 Toorian, A., *et al.*, "CubeSats as Responsive Satellites," AIAA-RS3-2005-3001, AIAA 3rd Responsive Space Conference, Los Angeles, CA, 25-28 April 2005.

3 McInnes, C.R., *Solar Sailing Technology, Dynamics and Mission Applications*, Springer-Praxis: London, 1999.

4 Winglee, R., Slough, J., Ziemba, T., and Goodson, A., "Mini-Magnetospheric Plasma Propulsion (M2P2): High Speed Propulsion Sailing the Solar Wind," *Proc. STAIF 2000,* AIP 2000.

5 Cosmo, M.L. and Lorenzini, E.C., *Tethers in Space Handbook*, (3rd ed). prepared for NASA/MSFC by Smithsonian Astrophysical Observatory, Cambridge, MA, 1997.

6 Hill, P.G. and Peterson, C.R., *Mechanics and Thermodynamics of Propulsion*, Prentice Hall: Upper Saddle River, NJ, 1991.

7 Jahn, R.G., *Physics of Electric Propulsion*, McGraw-Hill: New York, 1968.

8 Tsiolkovsky, K.E., "Exploration of the Universe with Reaction Machines" (in Russian), *The Science Review #5*, St. Petersburg, Russia, 1903.

9 Humble, R.W., Henry, G.N., and Larson, W.J., *Space Propulsion Analysis and Design*, McGraw-Hill: New York, 1995.

10 Personal Communications, Dr. William Hargus, Jr. (RZ/SS), Edwards Air Force Base, 2009.

11 Lozano, P. and Martínez-Sánchez, M., "Studies on the Ion-Droplet Mixed Regime in Colloid Thrusters," Ph.D. dissertation, MIT, 2003.

12 Roy, T., Hruby, V., Rosenblad, N., Rostler, P., and Spence, D., "CubeSat Propulsion Using Electrospray Thrusters," SmallSat 2009.

13 Wertz, J.R. and Larson, W.J., *Space Mission Analysis and Design*, Microcosm: El Segundo, CA, 1999.

14 Oleson, S., *Mission Advantages of Constant Power, Variable Isp Electrostatic Thrusters*, NASA/TM 2000-210477, NASA Glenn Research Center, Cleveland, OH, 2000.

15 "VACCO ChEMS Micro-Propulsion System: Micro-Propulsion System Overview," http://www.vacco.com/vacco/pdfs/mips2112.pdf.

16 "Busek Micropropulsion," http://www.busek.com/micro.html.

17 Shelton H., Hendricks, Jr., C.D., and Wuerker, R.F., "Electrostatic Acceleration of Microparticles to Hypervelocities," *J. Appl. Phys.*, **31**:1243 (1960).

18 Morris, D., "Analysis of Space Charge Limits During Electron Emission and Techniques for Improvement Thereof, With Application to Plasmas and In-Space Electric Propulsion," Ph.D. dissertation, University of Michigan, 2004.

19 Massey, D.R., Musinski, L.D., Liu, T.M., Gallimore, A.D., and Gilchrist, B.E., "The Nanoparticle Field Extraction Thruster: NanoFET," JANNAF 3rd Spacecraft Propulsion Subcommittee Meeting, Orlando, FL, 8-12 December 2008.

20 Marrese, C., Gallimore, A., Polk, J., Goodfellow, K., and Jensen, K., "Field Emission Array Cathodes for Electric Propulsion Systems," AIAA-1998-3484, 34th Joint Propulsion Conference, Cleveland, OH, 12-15 July 1998.

21 Fowler, R.H. and Nordheim, L., "Electron Emission in Intense Electric Fields," *Proceedings of the Royal Society of London*, **119**:781 (1928), pp. 173–81.

22 Musinski, L.D., Liu, T.M., Gilchrist, B.E., Gallimore, A.D., and Keidar, M., "Scalable Flat-Panel Nano-Particle MEMS/NEMS Thruster," IEPC-2005-176, 29th International Electric Propulsion Conference, Princeton, NJ, 31 October – 4 November 2005.

23 Liu, T.M., Musinski, L.D., Patel, P., Gallimore, A.D., Gilchrist, B.E., and Keidar, M., "Nanoparticle Electric Propulsion for Space Exploration," in *Space Technology and Applications International Forum − STAIF 2007*, edited by M.S. El-Genk, American Institute of Physics, Albuquerque, NM, 2007, pp. 787-94.

24 Casalino, L. and Colasurdo, G., "Optimization of Variable-Specific-Impulse Interplanetary Trajectories," *Journal of Guidance, Control, and Dynamics*, **27**:4 (2004), pp. 678-84.

25 Sovey, J., *et al.*, *Development of an Ion Thruster and Power Processor for New Millennium's Deep Space 1 Mission*, NASA/TM113129, NASA Lewis Research Center, Cleveland, OH, 1997.

26 Patel, P., Scheeres, D., and Gallimore, A., "Maximizing Payload Mass Fractions of Spacecraft for Interplanetary Electric Propulsion Missions," *Journal of Spacecraft and Rockets*, **43**: 4 (2006), pp. 822-7.

27 Fortov, V.E., Ivlev, A.V., Khrapak, S.A., Khrapak, A.G., and Morfill, G.E., "Complex (Dusty) Plasmas: Current Status, Open Issues, Perspectives," *Physics Reports*, **421** (2005), pp. 1-103.

28 Vedder, J.F., "Charging and Acceleration of Microparticles," *Review of Scientific Instruments*, **34** No. 11 (1963), pp. 1175-83.

29 Cermák, I., Grün, E., and Švestka, J., "New Results in Studies of Electric Charging of Dust Particles," Advances in Space Research, **15** No. 10 (1995), pp. 59-64.

30 Walch, B., Horányi, M., and Robertson, S., "Charging of Dust Grains in Plasma with Energetic Electrons," *Physical Review Letters*, **75** No. 5 (1995), pp. 838-41.

31 Trottenberg, T., Kersten, H., and Neumann, H., "Feasibility of Electrostatic Microparticle Propulsion," *New Journal of Physics*, **10** (2008), pp. 1-15.

32 Friichtenicht, J.F., "Two-Million-Volt Electrostatic Accelerator for Hypervelocity Research," *Review of Scientific Instruments*, **33** No. 2 (1962), pp. 209-12.

33 Stübig, M., Schäfer, G., Ho, T.-M., Srama, R., and Grün, E., "Laboratory Simulation Improvements for Hypervelocity Micrometeorite Impacts with a New Dust Particle Source," *Planetary and Space Science*, **49** (2001), pp. 853-8.

34 Trottenberg, T., Schneider, V., and Kersten, H., "Experiments on Contact Charging for an Electrostatic Microparticle Thruster," IEPC-2009-010, 31st International Electric Propulsion Conference, Ann Arbor, MI, 20-24 September 2009.

35 Cheng, D.K., *Field and Wave Electromagnetics*, Addison-Wesley: New York, 1989.

36 Musinski, L.D., "Investigation of a Micro- and Nano-Particle In-Space Electrostatic Propulsion Concept," Ph.D. dissertation, University of Michigan, 2009.

37 Müller, E.W., "Field Desorption," *Physical Review*, **102** No. 3 (1956), pp. 618-24.

38 Félici, N.-J., "Forces et Charges de Petits Objets en Contact avec une Électrode Affectée d'un Champ Électrique," *Revue Générale de l'Électricité*, **75** (1966), pp. 1145-60.

39 Crowley, J.M., *Fundamentals of Applied Electrostatics*, Wiley: New York, 1984.

40 Tobazéon, R., "Electrohydrodynamic Behaviour of Single Spherical or Cylindrical Conducting Particles in an Insulating Liquid Subjected to a Uniform DC Field," *Journal of Physics D: Applied Physics*, **29** (1996), pp. 2595-608.

41 Musinski, L.D., Liu, T.M., Gilchrist, B.E., and Gallimore, A.D., "Electrostatic Charging of Micro- and Nano-Particles for Use with Highly Energetic Applications," *Journal of Electrostatics*, 4 November 2008, pp. 1-8.

42 Smith, R.C., Carey, J.D., Forrest, R.D., and Silva, S.R.P., "Effect of Aspect Ratio and Anode Location on the Field Emission Properties of a Single Tip Based Emitter," *Journal of Vacuum Science and Technology B*, **23** No. 2 (2005), pp. 632-5.

43 Nader, B.F., Castle, G.S.P., and Adamiak, K., "Effect of Surface Conduction on the Dynamics of Induction Charging of Particles," *Journal of Electrostatics*, **67** (2009), pp. 394-9.

44 Yu, D., Castle, G.S.P., and Adamiak, K., "The Effect of Shape and Roughness on the Maximum Induction Charge for Small Particles," *Journal of Physics: Conference Series*, **142** (2008).

45 *COMSOL Multiphysics® Modeling Guide*, Version 3.5a, 2008.

46 Podczeck, F., *Particle-Particle Adhesion in Pharmaceutical Powder Handling*, Imperial College Press: London, 1998.

47 Bowling, R., "Analysis of Particle Adhesion on Semiconductor Surfaces," *J. Electrochem. Soc.*, **132** (1985), pp. 2208-14.

48 Hein, K., Hucke, T., Stintz, M., and Ripperger, S., "Analysis of Adhesion Forces Between Particles and Walls Based on the Vibration Method," *Part. Part. Syst. Charact*., **19** (2002), pp. 269-76.

49 Personal communications, Dr. Alfredo Carazo, Micromechatronics, 2009.

50 Krupp, H., "Particle Adhesion Theory and Experiment," *Advances in Colloid Interface Sciences*, **1** (1967), pp. 111-239.

51 Bohm, G., Krupp, H, and Schnabel, W., "Molecular Processes at Solid Surfaces," McGraw-Hill: New York, 1969.

52 Fowkes, F., *Surfaces and Interfaces*, Syracuse University Press: Syracuse, 1967.

53 Rabinovich, Y., Adler, J., Ata, A., Singh, R., and Moudgil, B., "Adhesion Between Nanoscale Rough Surfaces," *Journal of Colloid and Interface Science*, **232** (2000), pp. 17-24.

54 Klein, N. and Gafni, H., "The Maximum Dielectric Strength of Thin Silicon Oxide Films," *IEEE Transactions on Electron Devices*, **13** No. 12 (1966), pp. 281-9.

55 Hirsch, L.R., Gobin, A.M., Amanda, R.L., Tam, F., Drezek, R.A., Halas, N.J., and West, J.L., "Metal Nanoshells," *Annals of Biomedical Engineering*, **34** No. 1, (2006), pp. 15–22.

56 Koktysh, D.S., Liang, X., Yun, B-G., Pastoriza-Santos, I., Matts, R.L., Giersig, M., Serra-Rodríguez, C., Liz-Marzán, L.M., and Kotov, N.A., "Biomaterials by Design: Layer-by-Layer Assembled Ion-Selective and Biocompatible Films of TiO_2 Nanoshells for Neurochemical Monitoring, *Advanced Functional Materials*, **12** No. 4 (2002), 255-65.

57 Sutton, G.P. and Biblarz, O., *Rocket Propulsion Elements*, John Wiley & Sons: New York, 2001.

58 Zakirov, V., Sweeting, M., Lawrence, T., and Sellers, J., "Nitrous Oxide as a Rocket Propellant," *Acta Astronautica*, **48** No. 5-12 (2001), pp. 353-62.

59 Hales, T.C., "Historical Overview of the Kepler Conjecture," *Discrete Comput Geom* **36**:5–20 (2006).

60 Callister, W., *Materials Science and Engineering*, John Wiley and Sons: San Francisco, 2002.

61 Scott, G.D. and Kilgour, D.M., *J. Appl. Phys.*, **2**:863 (1969).

62 Pouliquen, O., Nicolas, M., and Weidman, P.D., *Phys. Rev. Lett.*, **79**:3640 (1997).

63 Jodrey, W.S. and Tory, E.M., *Phys. Rev. A*, **32**:2347 (1985).

64 Tobochnik, J. and Chapin, P.M., *Chem. Phys.*, **88**:5824 (1988).

65 Visscher, W.M. and Bolsterli, M., *Nature* (London) **239** No. 504 (1972).

66 Lozano, P. and Martinez-Sanchez, M., "Ionic Liquid Ion Sources: Characterization of Externally Wetted Emitters," *J. Colloid Interface Sci.*, **282** No. 2 (2005), pp. 415-21.

67 Lozano, P. and Martinez-Sanchez, M., "Efficiency Estimation of EMI-BF_4 Ionic Liquid Electrospray Thrusters," 41st AIAA/ASME/SAE/ASEE Joint Propulsion Conference, Tucson, AZ, 2005.

68 Aktakka, E.E., Kim, H., and Najafi, K., "Wafer-Level Fabrication of High Performance MEMS Using Bonded and Thinned Bulk Piezoelectric Substrates," 15th

International Conference on Solid-State Sensors, Actuators, and Microsystems (Transducers 2009), Denver, CO, June 2009, pp. 849-52.

69 Drenkow, B., Liu, T., Bell, J., Huang, M., Robinson, J., Moore, S., Singh, V., Trabert, R., Gilchrist, B., and Gallimore, A., "Developing a Reduced Gravity Testbed for the Nanoparticle Field Extraction Thruster," AIAA-2009-5194, 45th AIAA/ASME/SAE/ASEE Joint Propulsion Conference, Denver, CO, 3-5 August 2009.

70 Brereton, T. and Dymott, K.R., "Some Factors which Influence Screen Performance", in *Tenth International Mineral Processing Congress*, IMM, London, 1974, pp. 181-94.

71 Apling, A.C., "Blinding of Screens by Sub-Sieve Sized Particles," *Transactions of the Institution of Mining and Metallurgy, Section C, Mineral Processing and Extractive Metallurgy*, **93** (1984).

72 Standish, N., "The Kinetics of Batch Sieving," *Powder Technology*, **41** (1985), pp. 57-67.

73 Melling, A., "Tracer Particles and Seeding for Particle Image Velocimetry," *Meas. Sci. Technol.*, **8** (1997), pp. 1406-16.

74 Liu, T.M., Keidar, M., Musinski, L.D., Gallimore, A.D., and Gilchrist, B.E., "Theoretical Aspects of Nanoparticle Electric Propulsion," AIAA-2006-4335, 42nd AIAA/ASME/SAE/ASEE Joint Propulsion Conference, Sacramento, CA, 10-12 July 2006.

75 Taylor, G., "Disintegration of Water Droplets in an Electric Field," *Proc. Roy. Soc. London. Ser. A*, **280** No. 1382 (1964).

76 Tonks, L., "A Theory of Liquid Surface Rupture by a Uniform Electric Field," *Physical Review*, **48** (1935), pp. 562-8.

77 Liu, T., Deline, C., Ramos, R., Sandoval, S., Smetana, A., Gilchrist, B., Washabaugh, P., and Renno, N., "The Student Space Systems Fabrication Laboratory: An Approach to Space Systems Engineering Education," ASEE-2006-1917, 113th ASEE Conference, Chicago, IL, 18-21 June 2006.

78 Sopensky, E., "Trying Out Zero Gravity," *IEEE Potentials*, Aug./Sept. 1998, pp. 38-41.

79 Morris, S., Drenkow, B., Liu, T., Biehle, T., Munski, J., Han, H., Swieringa, K., Martinchek, P., Knapp, M., Trabert, R., Wind, R., Brierty, B., Gilchrist, B., and Gallimore, A., "Reduced Gravity Testing of the Nanoparticle Field Extraction Thruster Concept," AIAA-2008-4995, 44th AIAA/ASME/SAE/ASEE Joint Propulsion Conference, Hartford, CT, 21-23 July 2008.

80 Bilén, S.G. and Bernal, L.P., “Get Away Special Payload G-093: The VOrtex Ring Transit EXperiment (VORTEX) Flights,” NASA/CP-1999-209476, 1999 Shuttle Small Payloads Symposium, Annapolis, MD, 13-15 September 1999, pp. 129-38.

81 Man, P., Mastrangelo, C., Burns, M., and Burke, D., “Microfabricated Capillarity-Driven Stop Valve and Sample Injector,” in *The Eleventh Annual International Workshop on Micro Electro Mechanical Systems (MEMS 98) Proceedings*, IEEE, Heidelberg, Germany, 2008, pp. 45-50.

82 Moreira, R.G., Castell-Pérez, M.E., and Barrufet, M.A., *Deep Fat Frying: Fundamentals and Applications*, Aspen Publishers: Gaithersburg, MD, 1999.

83 O’Brien, R.D., *Fats and Oils: Formulating and Processing for Applications*, CRC Press: Boca Raton, FL, 2004.

84 Suvorov, V. and Zubarev, N., “Formation of the Taylor Cone on the Surface of Liquid Metal in the Presence of an Electric Field,” *J. Phys. D: Appl. Phys.*, **37** (2004), pp. 289-97.

85 Batchelor, G.K., *An Introduction to Fluid Dynamics*, Cambridge University Press: Cambridge, 1967.

86 Gamero-Castaño, M., "Induction Charge Detector with Multiple Sensing Stages," *Review of Scientific Instruments*, **78** (2007).